

**Analysis of Multiphase Fluid Flows via High Speed and Synthetic Aperture Three Dimensional Imaging**

by

Barry Ethan Scharfman

Bachelor of Science, Mechanical Engineering & Applied Mechanics  
Bachelor of Science, Economics/Operations & Information Management  
University of Pennsylvania, 2010

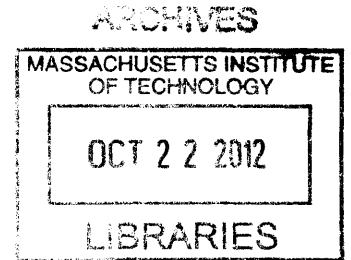
Submitted to the Department of Mechanical Engineering  
in Partial Fulfillment of the Requirements for the Degree of

Master of Science in Mechanical Engineering

at the

MASSACHUSETTS INSTITUTE OF TECHNOLOGY

September 2012



© 2012 Massachusetts Institute of Technology  
All rights reserved.

Signature of Author: .....  
Department of Mechanical Engineering  
August 10, 2012

Certified by: .....  
Alexandra H. Techet  
Associate Professor of Ocean and Mechanical Engineering  
Thesis Supervisor

Accepted by: .....  
David E. Hardt  
Chairman, Department Committee on Graduate Theses



# Analysis of Multiphase Fluid Flows via High Speed and Synthetic Aperture Three Dimensional Imaging

by

Barry Ethan Scharfman

Submitted to the Department of Mechanical Engineering  
on August 10, 2012, in partial fulfillment of the  
requirements for the degree of  
Master of Science in Mechanical Engineering

## Abstract

Spray flows are a difficult problem within the realm of fluid mechanics because of the complicated interfacial physics involved. Complete models of sprays having even the simplest geometries continue to elude researchers and practitioners. From an experimental viewpoint, measurement of dynamic spray characteristics is made difficult by the optically dense nature of many sprays. Flow features like ligaments and droplets break off the bulk liquid volume during the atomization process and often occlude each other in images of sprays.

In this thesis, two important types of sprays are analyzed. The first is a round liquid jet in a cross flow of air, which applies, for instance, to fuel injection in jet engines and the aerial spraying of crops. This flow is studied using traditional high-speed imaging in what is known as the bag breakup regime, in which partial bubbles that look like bags are formed along the downstream side of the liquid jet due to the aerodynamic drag exerted on it by the cross flow. Here, a new instability is discovered experimentally involving the presence of multiple bags at the same streamwise position along the jet. The dynamics of bag expansion and upstream column wavelengths are also investigated experimentally and theoretically, with experimental data having found to generally follow the scaling arguments predicted by the theory. The second flow that is studied is the atomization of an unsteady turbulent sheet of water in air, a situation encountered in the formation and breakup of ship bow waves.

To better understand these complicated flows, the emerging light field imaging (LFI) and synthetic aperture (SA) refocusing techniques are combined to achieve three-dimensional (3D) reconstruction of the unsteady spray flow fields. A multi-camera array is used to capture the light field and raw images are reparameterized to digitally refocus the flow field post-capture into a volumetric image. These methods allow the camera array to effectively “see through” partial occlusions in the scene. It is demonstrated here that flow features, such as individual droplets and ligaments, can be located in 3D by refocusing throughout the volume and extracting features on each plane.

Thesis Supervisor: Alexandra H. Tchet  
Title: Associate Professor of Ocean and Mechanical Engineering



## Acknowledgments

I would not have been able to complete this work without the support of my family, professors, and friends. I would like to thank my parents, my brother, Jason, and the rest of my family and friends both near and far for their continuous support and encouragement. I thank my advisor, Professor Alexandra Techet, for all of the guidance, support, and insights that she has provided during my time at MIT. Many thanks to Professors Douglas Hart and John Bush for their encouragement and offering their expertise. To my MIT labmates both present and past - Leah Mendelson, Abhishek Bajpayee, Juliana Wu, Jesse Belden, Jenna McKown, Amy Gao, Tim Gruber, and Ben Johnson as well as Daniel Kubaczyk and Tom Milnes - thank you for your enthusiasm, support, help, and friendship.



# Contents

<b>1</b>	<b>Introduction</b>	<b>25</b>
1.1	Spray Applications and Physics . . . . .	27
1.1.1	Overview of Sprays . . . . .	27
1.1.2	Spray Applications . . . . .	27
1.1.3	Spray Physics . . . . .	30
1.2	Light Field Imaging . . . . .	35
1.3	Outline of Thesis . . . . .	37
<b>2</b>	<b>Hydrodynamic Instabilities in Round Liquid Jets in Gaseous Cross Flow</b>	<b>43</b>
2.1	Introduction . . . . .	44
2.2	Experiments . . . . .	46
2.3	Observations . . . . .	49
2.4	Theory and Comparison with Experiments . . . . .	56
2.5	Discussion . . . . .	64
<b>3</b>	<b>Application of LFI &amp; SA Refocusing Techniques to a Liquid Jet in Cross Flow</b>	<b>75</b>
3.1	Introduction . . . . .	75
3.2	Synthetic Aperture Imaging . . . . .	77
3.2.1	Principle . . . . .	77
3.2.2	Simulation to Demonstrate the Method . . . . .	79
3.3	Liquid Jet in Cross Flow . . . . .	80

3.4	Conclusions . . . . .	91
<b>4</b>	<b>Application of LFI &amp; SA Refocusing to Turbulent Sheet Breakup</b>	<b>95</b>
4.1	Introduction . . . . .	95
4.2	Physics of Liquid Sheet Atomization in a Quiescent Gas . . . . .	96
4.3	Experiments . . . . .	100
4.4	Results and Discussion . . . . .	104
4.5	Conclusions . . . . .	112
<b>5</b>	<b>Summary and Conclusions</b>	<b>117</b>
<b>A</b>	<b>Additional Turbulent Sheet Breakup SA Refocusing Data</b>	<b>123</b>





# List of Figures

1-1	A high-speed photograph of a sprinkler at night by Edgerton (taken in 1939), recorded using a strobe fired for 10 ms. . . . .	26
1-2	Impacting jets in the combustion chamber of the gas generator of an industrial propulsion engine. . . . .	29
1-3	Classification of atomizers. . . . .	31
1-4	Rayleigh-Plateau instability. . . . .	33
1-5	Rayleigh-Taylor instability. . . . .	34
1-6	Destabilization of a plane liquid sheet of thickness $h$ in air at rest. . .	36
2-1	Liquid jet in cross flow breakup regimes based on $We_G$ . . . . .	46
2-2	A schematic illustration of the experimental apparatus. The water flow rate, $Q_J$ , nozzle diameter, $d_J$ , and air speed, $U_G$ , are all controllable. . . . .	48
2-3	A schematic illustration of a liquid jet in gaseous cross flow. . . . .	52
2-4	Photographs illustrating the single (left), transition (middle), and multiple (right) bag breakup regimes. . . . .	52
2-5	The multiple bag instability is observed when the liquid jet nozzle diameter exceeds the capillary length (side view). . . . .	53
2-6	Top view of the multiple bag instability. Yellow ovals mark discrete, adjacent bags. . . . .	54
2-7	Regime diagram illustrating the observed dependence of the development of bags along a liquid jet in cross flow on the governing dimensionless groups. . . . .	54
2-8	Schematic of the formation of a bag. . . . .	57

2-9	Measured temporal bag diameters for a variety of experimental conditions. . . . .	57
2-10	Schematic of the rupture and subsequent breakup of a bag. . . . .	57
2-11	Ligaments are formed during bag membrane breakup and retraction. . . . .	58
2-12	Sequence showing the elongation of an upstream ligament with a thickened tip due to the downstream expansion of the bag and its rims. . . . .	58
2-13	Measured ligament dimensions at breakup for a variety of experimental conditions. . . . .	59
2-14	Variation of upstream column wavelengths with $We_G$ . Upstream column waves for liquid jets in cross flow scale similarly with $We_G$ theoretically and experimentally for both single and multiple bag regimes. . . . .	61
2-15	Scaled temporal bag expansion diameter. This scaling holds true for both single and multiple bags independent of $We_G$ , $\sqrt{Bo}$ , and $q$ within the bag breakup regime. . . . .	65
2-16	Temporal bag expansion diameter variability. Even for different measurements from the same experiment, bag diameter values diverge at later times due to varying flow conditions that exist over time. . . . .	66
2-17	Overview of the instabilities that occur in the bag breakup regime. RP signifies the Rayleigh-Plateau instability, while RT is the Rayleigh-Taylor instability. . . . .	68
3-1	Simulated camera array in Blender. . . . .	80
3-2	Simulated images from each of the nine simulated cameras of a chessboard calibration grid at particular orientation. . . . .	81
3-3	A three-dimensional plot of the relative locations of the grid points from all of the simulated calibration images, including those shown in the previous figure. . . . .	81
3-4	Simulated raw images from each of the nine simulated cameras of a translucent sphere with a diameter of 5 mm. . . . .	82



3-5	Refocused images of the 5 mm diameter translucent sphere corresponding to the raw images in the previous figure. . . . .	82
3-6	Raw images from nine camera square array. . . . .	85
3-7	Sample calibration grid images for a particular grid orientation from each of the nine cameras in the array. . . . .	86
3-8	Refocused images corresponding to the raw images shown in Figure 3-6. . . . .	86
3-9	Raw images from nine camera square array. . . . .	87
3-10	Refocused images corresponding to the raw images shown in the previous figure. . . . .	88
3-11	Raw images from nine camera square array. . . . .	89
3-12	Refocused images corresponding to the raw images shown in the previous figure. . . . .	90
4-1	Schematic of the evolution of a sheet into a jet and then droplets during atomization. . . . .	96
4-2	Front view (top) and side view (bottom) of the destabilization of a liquid sheet moving in air initially at rest. . . . .	98
4-3	Photograph of the atomization of a turbulent liquid sheet in air. . . . .	99
4-4	Turbulent sheet of water flowing along an inclined plate; imaging was performed in the region where breakup and separation from the plate begins. . . . .	102
4-5	Turbulent sheet experimental setup showing relative locations of the camera array for each experiment. . . . .	102
4-6	Ten camera array of Flea 2 model FL2-08S2M/C from Point Grey Research, Inc. CCD cameras, with 50mm Nikkor lenses, typical of those used for the experiments presented herein. . . . .	103
4-7	Schematic of relative positions of the ten cameras in the array. . . . .	103
4-8	Sample calibration grid images for a particular grid orientation from each of the ten cameras in the array. . . . .	106

4-9	Sample refocused planes corresponding to the raw calibration grid images shown in the previous figure. . . . .	106
4-10	Raw array images at position 1, with the cameras focused on the sheet's center. Here the flow rate is 278 gallons per minute. . . . .	107
4-11	Sample refocused planes corresponding to the raw calibration grid images shown in the previous figure. . . . .	107
4-12	Raw array images at position 21, with the cameras focused on the sheet's center and rotated 30.8° clockwise from the horizontal to be aligned with the sheet. The liquid flow rate was 268 gallons per minute.	109
4-13	Two sample refocused planes with indicated in-focus features corresponding to the raw images in the previous figure. . . . .	109
4-14	Raw array images at position 34, with the cameras focused on the near sheet edge and rotated 30.8° clockwise from the horizontal to be aligned with the sheet. The liquid flow rate was 270 gallons per minute	110
4-15	Two sample refocused planes with indicated in-focus features corresponding to the raw images in the previous figure. . . . .	110
4-16	Raw array images at position 1, with the cameras focused on the near sheet edge and rotated 30.8° clockwise from the horizontal to be aligned with the sheet. The liquid flow rate was 270 gallons per minute . . .	111
4-17	Two sample refocused planes with indicated in-focus features corresponding to the raw images in the previous figure. . . . .	111
5-1	Raw camera array images of ligaments and droplets in the spray resulting from a sneeze. . . . .	118
5-2	Sample refocused image at plane $z = 24$ mm. The in-focus node that is located at this plane is circled. . . . .	119
A-1	Raw array images at position 1, with the cameras focused on the sheet's center and rotated 30.8° clockwise from the horizontal to be aligned with the sheet. The liquid flow rate was 270 gallons per minute. . . .	124

A-2	Sample refocused planes with indicated in-focus features corresponding to the raw images in the previous figure. . . . .	124
A-3	Raw array images at position 2, with the cameras focused on the sheet's center and rotated 30.8° clockwise from the horizontal to be aligned with the sheet. The liquid flow rate was 269 gallons per minute. . . .	125
A-4	Sample refocused planes with indicated in-focus features corresponding to the raw images in the previous figure. . . . .	125
A-5	Raw array images at position 3, with the cameras focused on the sheet's center and rotated 30.8° clockwise from the horizontal to be aligned with the sheet. The liquid flow rate was 268 gallons per minute. . . .	126
A-6	Sample refocused planes with indicated in-focus features corresponding to the raw images in the previous figure. . . . .	126
A-7	Raw array images at position 4, with the cameras focused on the sheet's center and rotated 30.8° clockwise from the horizontal to be aligned with the sheet. The liquid flow rate was 267 gallons per minute. . . .	127
A-8	Sample refocused planes with indicated in-focus features corresponding to the raw images in the previous figure. . . . .	127
A-9	Raw array images at position 5, with the cameras focused on the sheet's center and rotated 30.8° clockwise from the horizontal to be aligned with the sheet. The liquid flow rate was 268 gallons per minute. . . .	128
A-10	Sample refocused planes with indicated in-focus features corresponding to the raw images in the previous figure. . . . .	128
A-11	Raw array images at position 6, with the cameras focused on the sheet's center and rotated 30.8° clockwise from the horizontal to be aligned with the sheet. The liquid flow rate was 267 gallons per minute. . . .	129
A-12	Sample refocused planes with indicated in-focus features corresponding to the raw images in the previous figure. . . . .	129
A-13	Raw array images at position 7, with the cameras focused on the sheet's center and rotated 30.8° clockwise from the horizontal to be aligned with the sheet. The liquid flow rate was 268 gallons per minute. . . .	130

A-14 Sample refocused planes with indicated in-focus features corresponding to the raw images in the previous figure. . . . .	130
A-15 Raw array images at position 8, with the cameras focused on the sheet's center and rotated 30.8° clockwise from the horizontal to be aligned with the sheet. The liquid flow rate was 269 gallons per minute. . . .	131
A-16 Sample refocused planes with indicated in-focus features corresponding to the raw images in the previous figure. . . . .	131
A-17 Raw array images at position 9, with the cameras focused on the sheet's center and rotated 30.8° clockwise from the horizontal to be aligned with the sheet. The liquid flow rate was 268 gallons per minute. . . .	132
A-18 Sample refocused planes with indicated in-focus features corresponding to the raw images in the previous figure. . . . .	132
A-19 Raw array images at position 10, with the cameras focused on the sheet's center and rotated 30.8° clockwise from the horizontal to be aligned with the sheet. The liquid flow rate was 269 gallons per minute.	133
A-20 Sample refocused planes with indicated in-focus features corresponding to the raw images in the previous figure. . . . .	133
A-21 Raw array images at position 11, with the cameras focused on the sheet's center and rotated 30.8° clockwise from the horizontal to be aligned with the sheet. The liquid flow rate was 268 gallons per minute.	134
A-22 Sample refocused planes with indicated in-focus features corresponding to the raw images in the previous figure. . . . .	134
A-23 Raw array images at position 12, with the cameras focused on the sheet's center and rotated 30.8° clockwise from the horizontal to be aligned with the sheet. The liquid flow rate was 268 gallons per minute.	135
A-24 Sample refocused planes with indicated in-focus features corresponding to the raw images in the previous figure. . . . .	135
A-25 Raw array images at position 13, with the cameras focused on the sheet's center and rotated 30.8° clockwise from the horizontal to be aligned with the sheet. The liquid flow rate was 269 gallons per minute.	136

A-26 Sample refocused planes with indicated in-focus features corresponding to the raw images in the previous figure. . . . .	136
A-27 Raw array images at position 14, with the cameras focused on the sheet's center and rotated 30.8° clockwise from the horizontal to be aligned with the sheet. The liquid flow rate was 269 gallons per minute.	137
A-28 Sample refocused planes with indicated in-focus features corresponding to the raw images in the previous figure. . . . .	137
A-29 Raw array images at position 15, with the cameras focused on the sheet's center and rotated 30.8° clockwise from the horizontal to be aligned with the sheet. The liquid flow rate was 269 gallons per minute.	138
A-30 Sample refocused planes with indicated in-focus features corresponding to the raw images in the previous figure. . . . .	138
A-31 Raw array images at position 16, with the cameras focused on the sheet's center and rotated 30.8° clockwise from the horizontal to be aligned with the sheet. The liquid flow rate was 267 gallons per minute.	139
A-32 Sample refocused planes with indicated in-focus features corresponding to the raw images in the previous figure. . . . .	139
A-33 Raw array images at position 17, with the cameras focused on the sheet's center and rotated 30.8° clockwise from the horizontal to be aligned with the sheet. The liquid flow rate was 266 gallons per minute.	140
A-34 Sample refocused planes with indicated in-focus features corresponding to the raw images in the previous figure. . . . .	140
A-35 Raw array images at position 18, with the cameras focused on the sheet's center and rotated 30.8° clockwise from the horizontal to be aligned with the sheet. The liquid flow rate was 266 gallons per minute.	141
A-36 Sample refocused planes with indicated in-focus features corresponding to the raw images in the previous figure. . . . .	141
A-37 Raw array images at position 19, with the cameras focused on the sheet's center and rotated 30.8° clockwise from the horizontal to be aligned with the sheet. The liquid flow rate was 268 gallons per minute.	142

A-38 Sample refocused planes with indicated in-focus features corresponding to the raw images in the previous figure. . . . .	142
A-39 Raw array images at position 20, with the cameras focused on the sheet's center and rotated 30.8° clockwise from the horizontal to be aligned with the sheet. The liquid flow rate was 268 gallons per minute.	143
A-40 Sample refocused planes with indicated in-focus features corresponding to the raw images in the previous figure. . . . .	143
A-41 Raw array images at position 21, with the cameras focused on the sheet's center and rotated 30.8° clockwise from the horizontal to be aligned with the sheet. The liquid flow rate was 268 gallons per minute.	144
A-42 Sample refocused planes with indicated in-focus features corresponding to the raw images in the previous figure. . . . .	144
A-43 Raw array images at position 22, with the cameras focused on the sheet's center and rotated 30.8° clockwise from the horizontal to be aligned with the sheet. The liquid flow rate was 268 gallons per minute.	145
A-44 Sample refocused planes with indicated in-focus features corresponding to the raw images in the previous figure. . . . .	145
A-45 Raw array images at position 23, with the cameras focused on the sheet's center and rotated 30.8° clockwise from the horizontal to be aligned with the sheet. The liquid flow rate was 269 gallons per minute.	146
A-46 Sample refocused planes with indicated in-focus features corresponding to the raw images in the previous figure. . . . .	146
A-47 Raw array images at position 24, with the cameras focused on the sheet's center and rotated 30.8° clockwise from the horizontal to be aligned with the sheet. The liquid flow rate was 268 gallons per minute.	147
A-48 Sample refocused planes with indicated in-focus features corresponding to the raw images in the previous figure. . . . .	147
A-49 Raw array images at position 25, with the cameras focused on the sheet's center and rotated 30.8° clockwise from the horizontal to be aligned with the sheet. The liquid flow rate was 268 gallons per minute.	148

A-50 Sample refocused planes with indicated in-focus features corresponding to the raw images in the previous figure. . . . .	148
A-51 Raw array images at position 26, with the cameras focused on the sheet's center and rotated 30.8° clockwise from the horizontal to be aligned with the sheet. The liquid flow rate was 268 gallons per minute.	149
A-52 Sample refocused planes with indicated in-focus features corresponding to the raw images in the previous figure. . . . .	149
A-53 Raw array images at position 27, with the cameras focused on the sheet's center and rotated 30.8° clockwise from the horizontal to be aligned with the sheet. The liquid flow rate was 269 gallons per minute.	150
A-54 Sample refocused planes with indicated in-focus features corresponding to the raw images in the previous figure. . . . .	150
A-55 Raw array images at position 28, with the cameras focused on the sheet's center and rotated 30.8° clockwise from the horizontal to be aligned with the sheet. The liquid flow rate was 269 gallons per minute.	151
A-56 Sample refocused planes with indicated in-focus features corresponding to the raw images in the previous figure. . . . .	151
A-57 Raw array images at position 29, with the cameras focused on the sheet's center and rotated 30.8° clockwise from the horizontal to be aligned with the sheet. The liquid flow rate was 266 gallons per minute.	152
A-58 Sample refocused planes with indicated in-focus features corresponding to the raw images in the previous figure. . . . .	152
A-59 Raw array images at position 30, with the cameras focused on the sheet's center and rotated 30.8° clockwise from the horizontal to be aligned with the sheet. The liquid flow rate was 266 gallons per minute.	153
A-60 Sample refocused planes with indicated in-focus features corresponding to the raw images in the previous figure. . . . .	153
A-61 Raw array images at position 31, with the cameras focused on the sheet's center and rotated 30.8° clockwise from the horizontal to be aligned with the sheet. The liquid flow rate was 269 gallons per minute.	154

A-62 Sample refocused planes with indicated in-focus features corresponding to the raw images in the previous figure. . . . . 154

A-63 Raw array images at position 32, with the cameras focused on the sheet's center and rotated 30.8° clockwise from the horizontal to be aligned with the sheet. The liquid flow rate was 270 gallons per minute.155

A-64 Sample refocused planes with indicated in-focus features corresponding to the raw images in the previous figure. . . . . 155

A-65 Raw array images at position 33, with the cameras focused on the sheet's center and rotated 30.8° clockwise from the horizontal to be aligned with the sheet. The liquid flow rate was 269 gallons per minute.156

A-66 Sample refocused planes with indicated in-focus features corresponding to the raw images in the previous figure. . . . . 156

A-67 Raw array images at position 34, with the cameras focused on the sheet's center and rotated 30.8° clockwise from the horizontal to be aligned with the sheet. The liquid flow rate was 270 gallons per minute.157

A-68 Sample refocused planes with indicated in-focus features corresponding to the raw images in the previous figure. . . . . 157

A-69 Raw array images at position 35, with the cameras focused on the sheet's center and rotated 30.8° clockwise from the horizontal to be aligned with the sheet. The liquid flow rate was 270 gallons per minute.158

A-70 Sample refocused planes with indicated in-focus features corresponding to the raw images in the previous figure. . . . . 158

A-71 Raw array images at position 36, with the cameras focused on the sheet's center and rotated 30.8° clockwise from the horizontal to be aligned with the sheet. The liquid flow rate was 266 gallons per minute.159

A-72 Sample refocused planes with indicated in-focus features corresponding to the raw images in the previous figure. . . . . 159

A-73 Raw array images at position 37, with the cameras focused on the sheet's center and rotated 30.8° clockwise from the horizontal to be aligned with the sheet. The liquid flow rate was 267 gallons per minute.160



A-74 Sample refocused planes with indicated in-focus features corresponding to the raw images in the previous figure. . . . . 160

A-75 Raw array images at position 38, with the cameras focused on the sheet's center and rotated 30.8° clockwise from the horizontal to be aligned with the sheet. The liquid flow rate was 266 gallons per minute.161

A-76 Sample refocused planes with indicated in-focus features corresponding to the raw images in the previous figure. . . . . 161



# List of Tables

2.1	The parameter regime explored in this experimental study of a liquid jet in gaseous cross flow. . . . .	48
-----	---	----



# Chapter 1

## Introduction

Sprays are a class of multiphase flows that result from the atomization of a volume of liquid in the presence of a gas. Due to their prevalence and importance in both nature and engineering applications, many experimental, computational and theoretical investigations of sprays have been performed [2]. However, complete descriptions and models of spray flows with even the simplest geometries continue to elude researchers because of the complexity inherent in the study of sprays. They present a difficult class of problems in fluid mechanics because of the complex interfacial physics that come into play. All sprays include liquid and gas phases, and some may feature solid particles as well. These flows are usually turbulent, making them difficult to model. Thermal effects and evaporation also affect the evolution of sprays, further convoluting the problem.

From an experimental viewpoint, it is difficult to quantitatively measure dynamic spray characteristics. Imaging techniques are generally employed because pressure probes and other invasive means would disrupt and modify the flow, especially in the near-field region close to the jet or sheet nozzle exit, which is particularly difficult to analyze. Throughout most sprays, the flow is optically dense, with ligaments and droplets often occluding each other. This leads to considerable difficulty in effective image capture and analysis of sprays. Most prior imaging methods that have been



**Figure 1-1: A high-speed photograph of a sprinkler at night by Edgerton (taken in 1939), recorded using a strobe fired for 10 ms [8].**

employed suffer from a combination of issues ranging from complexity of the setup, to limited utility at the jet core, to only providing two-dimensional images, to overly constraining the experimental setup in terms of optical access. These issues have been overcome in the present study by employing a combination of the emerging quantitative three-dimensional imaging techniques of light field imaging (LFI) and synthetic aperture (SA) refocusing. By utilizing these methods, it is possible to obtain a three-dimensional (3D) reconstruction of the spray flow and to “see through” occlusions. Quantitative measurements of spray structures, such as droplets and ligaments, may be extracted from these refocused volumes. (Traditional high-speed imaging was also used to obtain time-resolved two-dimensional (2D) data.) This information can be used to better understand sprays and to improve the design of devices that involve them, such as liquid jet atomizers, among many other examples.

## 1.1 Spray Applications and Physics

### 1.1.1 Overview of Sprays

A sheet is formed when a fluid is injected into another relatively less dense fluid through a narrow slit with a thickness significantly less than its width. If the slit is circular, then a jet forms rather than a sheet. Sheet atomization actually occurs much quicker than jet breakup [2]. The scale of the volume of liquid to be atomized can range from light years in astronomical settings [3] to nanometers in a biological context [4]. A thorough knowledge of the physics of atomization is important for understanding the role of breakup behavior in many natural and engineering applications [6]. A book providing a review of the physics and applications related to sprays and jets, including a summary of relevant experimental, computational, and theoretical developments, has been published one year prior to this writing [2].

### 1.1.2 Spray Applications

Sprays play a pivotal role in many natural and engineering applications. Breaking ocean waves are an example of liquid sheet atomization in air. Waterfall mists and rain are other forms of natural atomization [6]. Coughing and sneezing involve sprays of droplets that can lead to airborne disease transmission [7]. Liquid atomizers are found in diesel injectors, furnace burners, spray guns, spray driers, and sprinkle chambers [2]. Figure 1-1 presents a high-speed photo by Harold Edgerton of water jet atomization in a sprinkler [8]. The jets break up due to disturbances that are amplified by both capillary and inertial forces. Primary and secondary atomization mechanisms that cause the breakup of the jets determine the resulting droplet size, position, and velocity distributions. These are important for understanding how to design the sprinkler in order to achieve the desired lawn water coverage with maxi-

mum efficiency.

Large industries, such as automotive, aerospace, and power-generation, that rely on spray and droplet technologies involve annual production in the tens of billions of dollars and possibly more [9]. Understanding the impact of design decisions on the resulting spray droplet distributions and characteristics can lead to important technological improvements and lower costs. The design parameters that can generally be controlled are injector size and shape, air speed, and liquid properties, such as surface tension and viscosity [10]. It turns out that viscosity plays the most important role of any liquid property in atomization [2]. Water and oil are the most common liquids found in atomization processes, but non-Newtonian (“complex”) fluids, such as emulsions and slurries, as well as solid particles may be found in sprays as well, depending on the application [2].

Sometimes it is advantageous to stall atomization, while other applications demand rapid breakup. Increasing the jet nozzle exit velocity and having the jet collide with a solid object can hasten atomization [2]. Another technique that is used to speed up atomization is the collision of jets, which atomize more quickly than do single jets [2]. Figure 1-2 presents an example of a Rayleigh-Plateau instability (see Section 1.1.3) found in the combustion chamber of the gas generator of an industrial propulsion engine (this figure was taken from [11]). The sheets shown in this image were formed by the collision of two liquid jets at an oblique angle. This type of flow was first analyzed by Taylor [12] and Miller [13] in 1960 and has been further investigated theoretically and experimentally by others [14, 15, 16, 17].

There are several types of jet atomizers. Figure 1-3 shows various types of atomizers organized by the type of energy that they employ along with schematics showing general modes of operation (this chart was taken from [2]). The liquid itself provides the kinetic energy to atomize it in pressure atomizers, including the jet, swirl, and the combination jet-swirl types. These are the most simple type of atomizers and



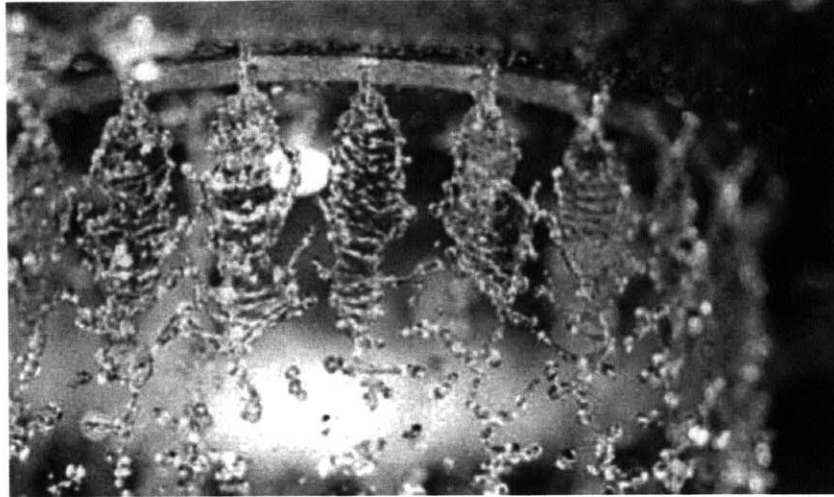


**Figure 1-2: Impacting jets in the combustion chamber of the gas generator of an industrial propulsion engine, taken from [11].**

are the most economical and widely used. Specifically, swirl atomizers are the most popular. They involve the rotation of the liquid before it is emitted into the gaseous environment.

Pneumatic atomizers feature the flow of the gaseous phase to help atomize the liquid. The gas may flow parallel, perpendicular, or swirled around the liquid, which enhances atomization by increasing the kinetic energy of the liquid and amplifying instabilities that develop in the liquid volume (see Section 1.1.3). Flows of the kind encountered in cross flow pneumatic atomizers will be analyzed in depth in Chapters 2 and 3. Rotary atomizers involve the transfer of kinetic energy from the rotating device to the liquid, which breaks up due to centrifugal forces. A main disadvantage of this type of atomizer is that high rotation speeds are necessary, which requires a large power input. Other methods are also used, such as vibrating the apparatus to hasten the atomization process. Often, a combination of atomizer types is employed. In traditional atomizers, the efficiency of atomization, defined as the ratio of the surface energy to the sum of surface energy, kinetic energy, and energy loss due to friction, is generally less than 0.1%. By this metric, pressure atomizers are the most

efficient. However, the other more power-demanding methods are often required and can be more effective [2].

### 1.1.3 Spray Physics

#### Common Spray Instabilities

Thin jets or sheets of liquid are used in atomizers because these volumes have large surface area and hence high surface energy, which leads to greater instabilities. In most atomization processes, waves appear throughout the volume of liquid whose amplitudes quickly increase, leading to instabilities followed by breakup [2]. The state of the gas of a spray plays an important role in the atomization process. For instance, critical and supercritical temperature and pressure are found in diesel engines [9]. Other critical parameters are the velocity of the gas, along with its density and viscosity. These properties dictate the types of instabilities and, therefore, the physical mechanisms governing the atomization process.

#### Rayleigh-Plateau Instability

Liquid jet atomization in an ambient gas has been examined quantitatively since the 19th century [2, 18]. Plateau found that a liquid jet in still air breaks into spherical droplets to minimize surface tension. This is the phenomenon that is responsible, for instance, for the breakup of a liquid column from a faucet into droplets (Figure 1-4). Plateau stated that a jet breaks up into segments of equal length, each of which has a length of  $2\pi$  times the jet radius [19]. Droplets then form from these sections of the jet due to surface tension. It could be considered ironic that the cohesive force of surface tension actually ends up causing the atomization of jets into ligaments and droplets [20]. However, this is the case because under the appropriate conditions

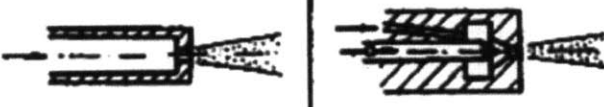


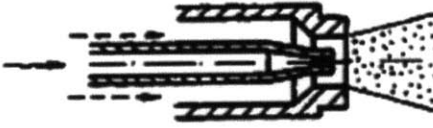

Liquid energy	<p><b>Jet atomizers</b></p> <p>continuous      intermittent</p> 
	<p><b>Swirl atomizers</b></p> 
	<p><b>Jet-swirl atomizers</b></p> 
Gas energy	<p><b>Pneumatic atomizers</b></p> 
Mechanical energy	<p><b>Rotary atomizers</b></p> 
Vibration energy, electric energy, etc.	<p><b>Various atomizers:</b> acoustic, ultrasonic, electrostatic, etc.</p>

Figure 1-3: Classification of atomizers, taken from [2].

it is more energetically favorable for the liquid column to take the form of discrete droplets as opposed to remaining as a continuous jet. It turns out that the surface area of the resulting droplets is less than that of the original liquid jet when the final droplet radius exceeds 1.5 times the jet radius [21].

Rayleigh showed that hydrodynamic instability is the cause of jet breakup in this case [22, 23]. A linear stability analysis involving perturbing the radius, surface velocities, and pressure distribution on a column of liquid in the equilibrium state shows that the disturbance wavelength along the jet for the fastest growth rate of instability is about 9.02 times the undisturbed jet radius, or 143.7% of its circumference. These results were found by neglecting the ambient fluid, viscosity of the liquid jet, and gravity. Rayleigh also showed that for a viscous jet in an inviscid gas (neglecting the mass of the gas), the most unstable wavelength is infinitely long [24]. For an inviscid gas jet in an inviscid liquid, the most unstable wavelength was found to be 206.5% of the undisturbed jet circumference [25].

Tomotika found that there is a ratio of the viscosities of the jet and ambient gas that maximizes the growth rate of jet instability [26]. Unlike Rayleigh, Chandrasekhar included the liquid viscosity and density in his model of jet breakup and demonstrated theoretically that viscosity slows down atomization and increases the resulting drop diameter [22]. The experimental investigations of Donnelly and Glaberson [28] as well as Goedde and Yuen [29] agree with the theory developed by Rayleigh and Chandrasekhar.

## **Rayleigh-Taylor Instability**

The Rayleigh-Taylor instability occurs when a fluid of less density, such as air, is accelerated towards one of greater density, e.g. water [22]. This type of instability can occur when a heavier fluid is located above a lighter fluid. In the context of sprays, it

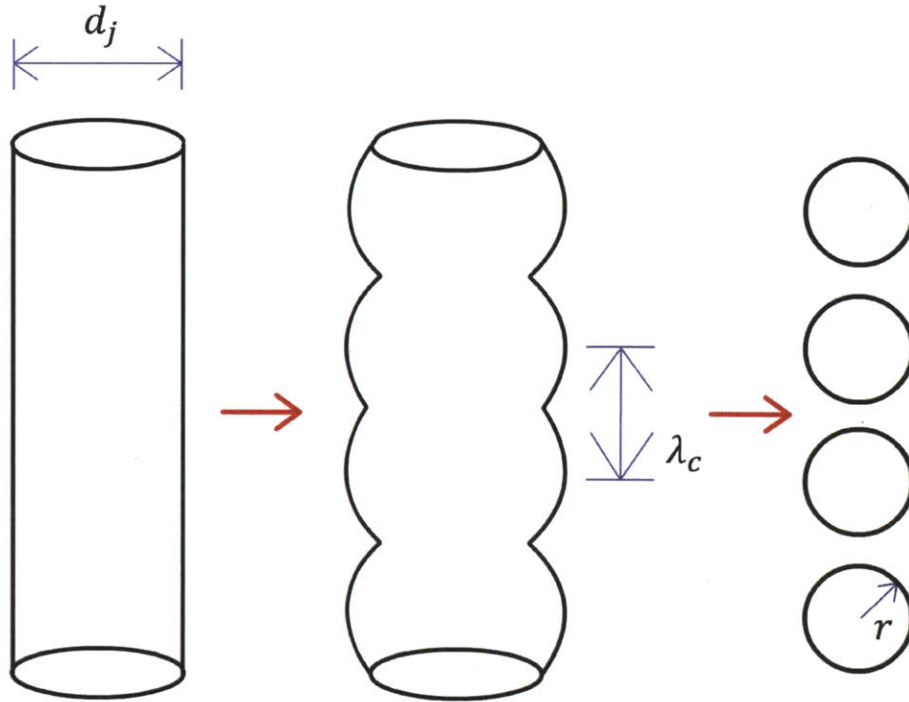


**Figure 1-4: Rayleigh-Plateau instability.**

is relevant in pneumatic atomizers involving a liquid jet in a cross flow of air. The air moves toward the relatively heavier fluid and bends the liquid jet in the downstream direction due to the aerodynamic drag force. As the air flows along the curved jet, it accelerates, creating waves along the jet surface. Figure 1-5 presents a schematic of the development of the Rayleigh-Taylor instability in a liquid jet in cross flow.  $U_G$  is the gas velocity,  $V_j$  is the liquid nozzle exit velocity,  $d_j$  is the nozzle exit diameter,  $dl$  is the length of the segment of the jet, and  $R$  is the radius of curvature of the deformed jet.  $\lambda_c$  is the most unstable wavelength for the Rayleigh-Taylor instability, which is  $2\sqrt{3}\pi(\sigma/(\rho a_c))^{1/2}$  (neglecting viscosity), where  $\sigma$  is the surface tension,  $\rho$  is the liquid density, and  $a_c$  is the acceleration [22].

### **Kelvin-Helmholtz Instability**

In most atomization processes, the liquid volume often becomes a sheet, at least

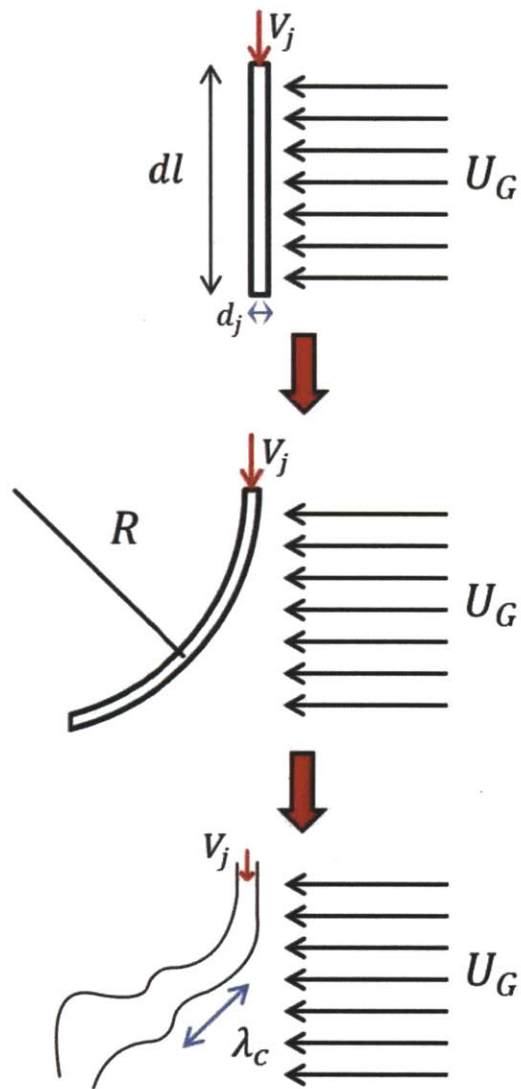


Figure 1-5: Rayleigh-Taylor instability.

in intermediate breakup stages [9]. The next stage of atomization is primary breakup, during which ligaments are formed. These structures then shatter into droplets and determine the final droplet size distribution in the spray [31]. The level of corrugation of ligaments and other structures at the time of breakup is also important in setting droplet size distribution [32]. A liquid sheet in the presence of an ambient gas will develop waves naturally when moving fast enough relative to the gas due to a shear, Kelvin-Helmholtz type instability [33, 34] that exacerbates any disturbances in the sheet [6, 12, 9]. This type of instability is caused by the relative (parallel) motion between two adjacent fluids of different densities (or of different layers of a single density stratified fluid).

Figure 1-6 shows a schematic of the destabilization of a plane liquid sheet of thickness  $h$  in air at rest [6, 12, 9]. The sheet is moving to the right with a velocity  $u$  and is perturbed by a disturbance with amplitude  $\zeta$  and phase  $\phi$ .  $\rho$ ,  $\rho_a$ , and  $r$  are the liquid density, gas density, and distance along the sheet, respectively. For two fluids arranged horizontally moving parallel to each other with different densities (neglecting surface tension), the maximum unstable wavelength due to the Kelvin-Helmholtz instability is  $\frac{2\pi\alpha_1\alpha_2(U_1-U_2)^2}{g(\alpha_1-\alpha_2)}$ , where  $\alpha_1$  and  $\alpha_2$  are the ratios of the density of each fluid to the sum of the densities,  $g$  is the acceleration due to gravity, and  $U_1$  and  $U_2$  are the constant velocities of each of the fluids, respectively [22]. This instability will be discussed in greater depth as it applies to the breakup of a turbulent water sheet in air in Chapter 4.

## 1.2 Light Field Imaging

A fundamental challenge in experimental fluid mechanics is the accurate spatial and temporal resolution of three-dimensional, multiphase fluid flows, such as sprays. Whether for determining new fluid phenomena, evaluating new designs, or bench-

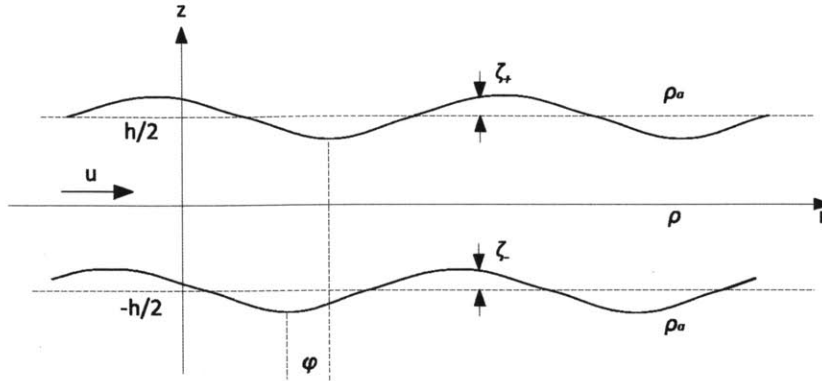


**Figure 1-6: Destabilization of a plane liquid sheet of thickness  $h$  in air at rest, taken from [9].**

marking computational codes, fully spatially- and time-resolved experimental data is paramount. Given recent advances in camera and imaging technologies, and the growing prevalence of commercially available light field imaging systems, the opportunities for obtaining such data are achievable at a lower cost and with greater resolution and computational savings. Stemming from the computer vision communities, light field imaging (LFI) and synthetic aperture (SA) refocusing techniques have been combined in an emerging method to resolve three-dimensional flow fields over time [1]. This technique is aptly suited for sprays, particle laden and multiphase flows, as well as complex unsteady and turbulent flows.

At the core of light field imaging, a large number of light rays from a scene are collected and subsequently reparameterized based on calibration to determine a 3D image [2]. In practice, one method used by researchers in the imaging community for sampling a large number of rays is to use a camera array [37, 38] or more recently, a single imaging sensor and a small array of lenslets (lenslet array) in a plenoptic camera (e.g. [5]). The combined LFI and SA approach is applied herein to the reparameterization methods to 3D spray fields and fluid flows.

In short, light field imaging involves the reparameterization of images captured using an array of cameras, or from a single sensor and lenslet array (i.e. a plenoptic



camera), to digitally refocus a flow field post-capture. All cameras record a volumetric scene in-focus, and by recombining images in a specific manner, individual focal planes can be isolated in software to form refocused images. Flow features, such as individual droplets, can be located in 3D by refocusing throughout the volume and extracting features on each plane. An implication of the refocusing is the ability to “see through” partial occlusions in the scene. This method extends measurement capabilities in complicated flows where knowledge is incomplete. Utilization of this technique allows for finer measurements of flow quantities and structures that would have been impossible with prior methods.

In particular, this imaging system is designed to measure and locate features, such as bubbles, droplets and particles in three spatial dimensions over time in multiphase flows. Other measurement systems often only allow practitioners to measure average quantities or envelopes of flow regions that do not require such high resolution. This new technique has already demonstrated the capability to resolve very fine flow features, which is especially important in multiphase and turbulent flow fields that contain very minute flow structures and length scales. An instrument of this kind is of great aid in a variety of engineering applications in areas such as air-sea interaction, naval hydrodynamics, aerospace, turbulence and beyond.

### **1.3 Outline of Thesis**

Chapter 2 presents a theoretical and experimental investigation of a liquid jet in gaseous cross flow in the bag breakup regime. Bags are partial bubbles that form along the jet due to the aerodynamic drag force of the air on the liquid jet. Water jets emanating vertically downward into a horizontal wind tunnel were recorded using traditional 2D high-speed video to analyze the instabilities that develop in the jet as well as primary and secondary jet breakup. It was discovered that there is a

transition regime from single to multiple side-by-side bags for liquid jet diameters that are approximately equal to the liquid's capillary length (which is approximately 2.7 mm for water). Once this diameter size is exceeded, multiple bags are consistently present throughout the length of the liquid jet in a gaseous cross flow in the bag breakup regime.

Chapter 3 discusses further development and validation of the light field imaging and synthetic aperture refocusing techniques. These methods are then applied to the liquid jet in cross flow experiments described in Chapter 2. These 3D imaging techniques were used to reconstruct an image volume from the images taken by each of the individual cameras in the arrays used to image the flows.

In Chapter 4, an experimental investigation of the atomization of a turbulent sheet of water launched into the air at an angle is presented. As in Chapter 3, light field imaging and synthetic aperture refocusing techniques are utilized to analyze this flow. The focus here is the primary sheet breakup into ligaments and relatively large droplets on the underside of the sheet. These flow features were successfully resolved in three dimensions.

Finally, Chapter 5 presents conclusions for the entire thesis. A summary of the physical insights gained into the various sprays that were analyzed is provided. In addition, the synthetic aperture imaging results are summarized. Applications of the combined LFI and SA methods to other flows, such as sneezing and airborne disease transmission, are discussed. Future steps to be taken are outlined.

# Bibliography

- [1] N. Ashgriz. Handbook of Atomization and Sprays: Theory and Applications. New York, NY: Springer. 2011.
- [2] L. Bayvel and Z. Orzechowski. Liquid Atomization. Washington, DC: Taylor & Francis. 1993.
- [3] P. A. Hughes. Beams and Jets in Astrophysics. Cambridge University Press. 1991.
- [4] S. Benita. Microencapsulation. Marcel Dekker. 1996.
- [5] S. P. Lin. Breakup of Liquid Sheets and Jets. Cambridge University Press. 2003.
- [6] A. H. Lefebvre. Atomization and Sprays. New York: Hemisphere. 1989.
- [7] J. K. Gupta, C.-H. Lin, and Q. Chen. Flow dynamics and characterization of a cough. *Indoor Air*, 19(6):517-525. 2009.
- [8] H. E. Edgerton, E. Jussim, and G. Kayafas. Stopping time: the photographs of Harold Edgerton. New York: H. N. Abrams. 1987.
- [9] W. A. Sirignano. Fluid Dynamics and Transport of Droplets and Sprays. Cambridge, UK: Cambridge University Press. 1999.
- [10] E. Villermaux. Fragmentation. *Annual Review of Fluid Mechanics*, 39(1): 419-446. 2007.
- [11] N. Bremond and E. Villermaux. Atomization by jet impact. *J. Fluid Mech.*, 549: 273-306. 2006.

- [12] G. I. Taylor. Formation of thin flat sheets of water. *Proc. R. Soc. Lond. A*, 259: 1–17. 1960.
- [13] K. D. Miller. Distribution of spray from impinging liquid jets. *J. Phys* 31: 1132–1133. 1960.
- [14] M. F. Heidmann, R. J. Priem, and J. C. Humphrey. A study of sprays formed by two impacting jets. NACA IN 3835. 1957.
- [15] N. Dombrowski and P. C. Hooper. A study of the sprays formed by impinging jets in laminar and turbulent flow. *J. Fluid Mech.* 18: 392–400. 1963.
- [16] E. A. Ibrahim and A. Przekwas. Impinging jets atomization. *Phys. Fluids A* 3: 2981–2987. 1991.
- [17] J. W. M. Bush and A. E. Hasha. On the collision of laminar jets: fluid chains and fishbones. *J. Fluid Mech.* 511: 285–310. 2004.
- [18] S. P. Lin and R. D. Reitz. Drop and Spray Formation from a Liquid Jet. *Annual Review of Fluid Mechanics*, 30: 85-105. 1998.
- [19] J. Plateau. *Statique Experimentale et Theorique des Liquids Soumis aux Seules Forces Moleculaire*. Paris: Cauthier Villars. 1, 2: 450-495. 1873.
- [20] J. Eggers and E. Villermaux. Physics of liquid jets. *Rep. Prog. Phys.* 71: 036601. 2008.
- [21] P.-G. de Gennes, F. Brochard-Wyart, and D. Quéré. *Capillarity and Wetting Phenomena: Drops, Bubbles, Pears, Waves*. New York, NY: Springer. 2004.
- [22] Lord Rayleigh. On the capillary phenomenon of jets. *Proc. R. Soc. London.* 29: 71-97. 1879a.
- [23] Lord Rayleigh. On the instability of jets. *Proc. Lond. Math. Soc.* 10: 4-13. 1879b.
- [24] Lord Rayleigh. On the instability of a cylinder of viscous liquid under capillary force. *Phil. Mag.* 34:145–54. 1892a.

- [25] Lord Rayleigh. On the instability of cylindrical fluid surfaces. *Phil. Mag.* 34:177-180. 1892b.
- [26] S. Tomotika. On the instability of a cylindrical thread of a viscous liquid surrounded by another viscous fluid. *Proc. R. Soc. London Ser. A.* 150:322–37. 1935.
- [27] S. Chandrasekhar. *Hydrodynamic and Hydromagnetic Stability*. Oxford: Oxford Univ. Press. 1961.
- [28] R. J. Donnelly and W. Glaberson. Experiments on the capillary instability of a liquid jet. *Proc. R. Soc. London Ser. A.* 290:547–56. 1996.
- [29] E. F. Goedde and M. C. Yuen. Experiments on liquid jet instability. *J. Fluid Mech.* 40:495– 512. 1970.
- [30] N. Bremond, C. Clanet, and E. Villermaux. Atomization of undulating liquid sheets. *J. Fluid Mech.* 585: 421–456. 2007.
- [31] F. Savart. Mémoire sur la constitution des veines liquides lancées par des orifices circulaires en mince paroi. *Ann. de chim.* 53: 337–398. 1833a.
- [32] E. Villermaux, P. Marmottant, J. Duplat. Ligament-mediated spray formation. *Phys. Rev. Let.* 92: 074501. 2004.
- [33] H. von Helmholtz. On discontinuous movements of fluids. *Phil. Mag.* 36: 337–346. 1868.
- [34] Lord Kelvin. Hydrokinetic solutions and observations. *Philo. Mag.* 42: 362–377. 1871.
- [35] J. Belden, T. T. Truscott, M. Axiak, and A. H. Techet. Three-dimensional synthetic aperture particle image velocimetry. *Meas Sci Technol* 21:1-21. 2010.
- [36] A. Isaksen, L. McMillan, and S. J. Gortler. Dynamically reparameterized light field SIGGRAPH '00: *Proc. 27th Ann. Conf. on Computer Graphics and Interactive Techniques* (New York: ACM Press/Addison-Wesley). 297–306. 2000.

- [37] V. Vaish, B. Wilburn, N. Joshi, and M. Levoy. Using plane + parallax for calibrating dense camera arrays Proc. 2004 IEEE Computer Society Conf. on Computer Vision and Pattern Recognition (CVPR04') (June–July 2004) v. 1, Los Alamitos, CA: IEEE Computer Society Press. 2–9. 2004.
  
- [38] V. Vaish, G. Garg, E. Talvala, E. Antunez, B. Wilburn, M. Horowitz, and M. Levoy. Synthetic aperture focusing using a shear-warp factorization of the viewing transform. Proc. IEEE Computer Society Conf on Computer Vision and Pattern Recognition (CVPR05')—June Workshops. Los Alamitos, CA: IEEE Computer Society Press 3:129. 2005.
  
- [39] K. Lynch. Development of a 3-D Fluid Velocimetry Technique based on Light Field Imaging. MS Thesis, Auburn University, Auburn, Alabama. 2011.

## Chapter 2

# Hydrodynamic Instabilities in Round Liquid Jets in Gaseous Cross Flow

Water jets in the presence of uniform perpendicular air cross flow were investigated theoretically and experimentally using high-speed imaging for gaseous Weber number  $We_G = \rho_G U_G^2 d_J / \sigma$  (where  $\rho_G$  is the density of the gas,  $U_G$  is the velocity of the gas,  $d_J$  is the liquid jet nozzle exit diameter, and  $\sigma$  is the surface tension) below 30, small liquid jet Ohnesorge number  $Oh = \mu_J / \sqrt{\rho_J \sigma d_J}$  (where  $\rho_J$  is the density of the liquid and  $\mu_J$  is the liquid's viscosity), and large Reynolds numbers for the liquid  $Re_J = \rho_J V_J d_J / \mu_J$  (where  $V_J$  is the liquid jet nozzle exit speed) and gas  $Re_G = \rho_G U_G d_J / \mu_G$  (where  $\mu_G$  is the gaseous phase's viscosity). Previously, a bag instability has been reported for  $4 \leq We_G \leq 30$ . Jets first deform into curved sheets due to aerodynamic drag, followed by the formation of partial bubbles (bags) along the jet streamwise direction that expand and ultimately burst. Single bags were present at each streamwise position along the liquid jets in prior experiments featuring liquid jet nozzle diameters less than the capillary length of water. It has been found that at larger nozzle diameters it is possible to observe multiple bags at the same streamwise

jet position because single bags of such large sizes would be unstable. Measurements of bag expansion diameters over time for a wide range of experimental conditions were found to follow the trend predicted by a theoretical analysis. A theoretical derivation for the upstream jet column wavelength was found to match experimental data in both the single and multiple bag regimes. Other flow features, such as upstream ligament extension properties, were measured and analyzed as well.

## 2.1 Introduction

The formation and subsequent breakup of bag-like bubble structures emanating from round nonturbulent liquid jets in uniform gaseous cross flow within the bag breakup regime were studied experimentally and theoretically. Atomization of liquid jets and sheets has numerous significant applications, including film coating, nuclear safety curtain formation, agricultural sprays, ink jet printing, fiber and sheet drawing, powder metallurgy, toxic material removal, encapsulation of biomedical materials, and spray combustion. While some applications require more rapid jet breakup rates, in other cases it is desirable to reduce the speed of atomization, making knowledge of the mechanism of jet atomization critical [1]. Spray flows with very rapid cross flow air speeds are applicable to combustion in air-breathing propulsion systems, such as gas turbine augmentor systems [2]. [3] examined the role of surface tension in jet instability. [4] analyzed jet stability with acoustic excitation of the jet. The Rayleigh-Plateau instability is responsible for the capillary breakup of a liquid jet, such as a column of liquid from a faucet. [1], [5], and [6] review many other investigations related to liquid jets flowing under a wide variety of conditions.

Some prior studies of round nonturbulent liquid jets in uniform gaseous cross flow investigated depth of penetration of the liquid jet and jet trajectories for various experimental conditions [7, 8, 9, 10]. Liquid bag breakup has also been observed



in liquid jets accompanied by a coaxial flow of gas [11] and in drop deformation and breakup in a flow of air. The most relevant studies to the present investigation are [8, 12, 13, 15]. [12] developed a regime map for liquid jets in cross flow based on  $We_G$  and the momentum flux ratio  $q = \rho_J V_J^2 / (\rho_G U_G^2)$ .  $We_G$  is a dimensionless parameter that indicates the relative importance of the inertia of the gas and surface tension, while  $q$  is the ratio of the liquid's inertia to that of the gas. Mazallon et al. found that for  $Oh < 0.1$ , the regimes are only governed by  $We_G$ . They also created a new regime map with  $Oh$  and  $We_G$  as the coordinates, which [8] modified later. When viscous effects are small ( $Oh \ll 0.1$ ), [13] found that breakup regime transitions of the liquid jet are determined by  $We_G$  number as follows: column breakup ( $We_G < 4$ ), bag breakup ( $4 < We_G < 30$ ) (modified by [8]), multimode breakup ( $30 < We_G < 110$ ), and shear breakup ( $We_G > 110$ ). Figure 2-1 presents a regime diagram with photographic examples of each known instability category (adapted from [8]). The bag breakup regime is highlighted because it is the focus of the present study. [15] recently published an article about the bag breakup regime of liquid jets in cross flow. It discusses many statistics about the formation of nodes on bags and breakup of bags into tiny droplets due to the breakup of the bag membrane, larger droplets caused by the atomization of the two strings of the ring bounding the base of the bag, and still larger droplets associated with bag nodes. The size of bag droplets is independent of  $We_G$ , but node- and ring-droplet sizes decrease with increasing  $We_G$ . Column waves are also described mathematically in light of the Rayleigh-Taylor instability, which occurs when a fluid is accelerated towards another relatively heavier fluid [4].

The present study explores the destabilization and primary breakup mechanisms of a liquid jet in cross flow. §2.2 describes the experimental methods employed in this study and §2.3 presents the results of the experimental investigation. A new instability has been discovered involving the appearance of multiple side-by-side bags

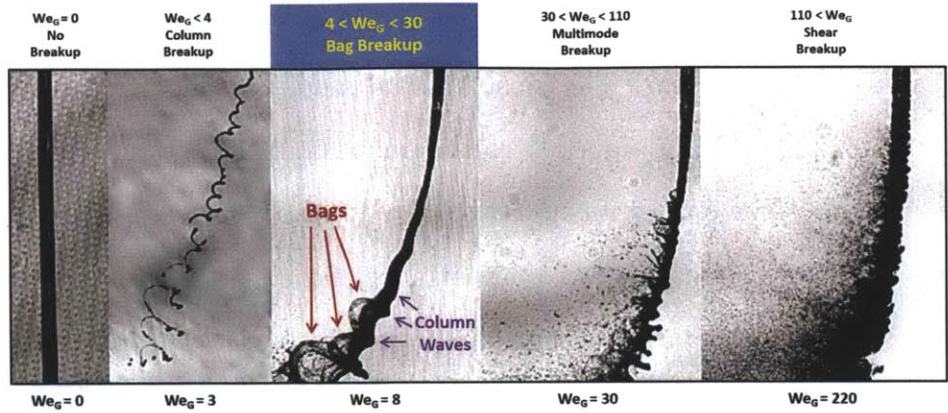


Figure 2-1: Liquid jet in cross flow breakup regimes based on  $We_G$  (adapted from [8]).

at the same streamwise jet position when the jet nozzle diameter exceeds the capillary length. It was also found that a regime exists when the jet nozzle diameter equals the capillary length that marks a transition between the single and multiple bag regimes. Various flow measurements are made in the single bag, multiple bag, and transition regimes. In §2.4 equations are developed to describe the upstream column wavelength and bag expansion diameter over time. Experimental data are found to match the trends predicted by these formulas. Finally, the instabilities responsible for the primary breakup mechanisms of a liquid jet in cross flow are detailed in §2.5.

## 2.2 Experiments

This experimental study is composed of three parts. The first is an exploratory investigation of the flow structures generated in the case of a liquid jet in gaseous cross flow. Secondly, a careful quantitative study of the upstream column waves is performed and the instability responsible for them investigated. Finally, the formation and destruction of fluid bags are studied experimentally in order to test the validity of theoretical developments describing the bag diameters over time and the associated

jet ligament dynamics.

A schematic illustration of the apparatus used in this experimental study is presented in Figure 2-2. Water was injected downward into a horizontal wind tunnel to generate the multiphase flows under consideration. The wind tunnel test section width, height, and length were 1, 1, and 2.5 ft, respectively. The water was pumped from the reservoir through polystyrene tubing into metal water jet nozzles of diameters in the range of 1-9 mm. Water volume flow rates were controlled using a variable-flow pump (Cole Parmer, Model EW-75211-60) and were measured with a digital flowmeter (AW Company Model JFC-01) that gave an accuracy of 0.1% over the range considered. The speed of the water exiting the nozzle was measured by collecting a measured volume of water over a specified amount of time. Streamwise velocity measurements were made via image analysis using MATLAB code in a manner similar to that described in [15]. As has been previously noted and confirmed in the present study, the instantaneous speed at any streamwise point along the jet is essentially the same as the nozzle exit velocity [15]. An anemometer was used to measure the air cross flow speed (La Crosse Technology, Model EA-3010U) with an accuracy of 0.1 m/s. Characteristic flow rates and other experimental parameters are listed in Table 2.1. Images were acquired using an IDT X-Stream XS3 high-speed camera with a Nikon Nikkor 28 mm lens. Most of the images were recorded from a side view, but angled top views were recorded as well to better understand the flow structures. All images were recorded at 1630 frames per second. Two IDT 19-LED pulsed light banks were synchronized with the camera to back light the flow being recorded.

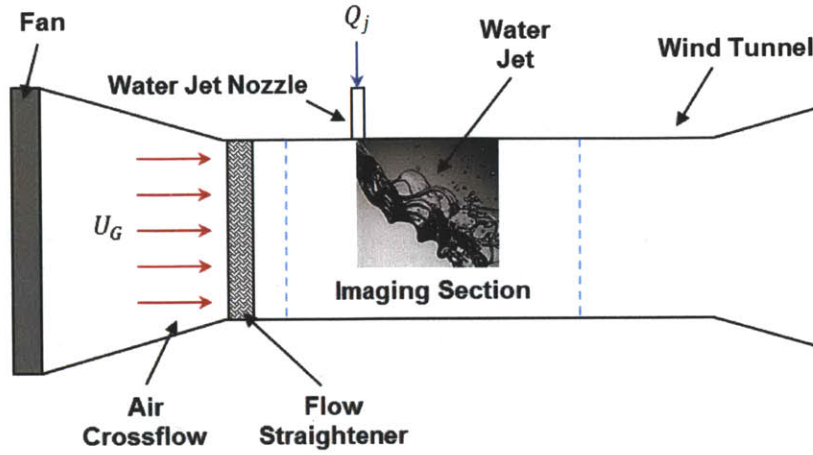


Figure 2-2: A schematic illustration of the experimental apparatus. The water flow rate,  $Q_J$ , nozzle diameter,  $d_J$ , and air speed,  $U_G$ , are all controllable.

Parameter	Symbol	Range
Nozzle diameter	$d_J$	1-9 mm
Air density	$\rho_G$	1.0-1.2 kg/m <sup>3</sup>
Water density	$\rho_J$	1000 kg/m <sup>3</sup>
Air speed	$U_G$	6-13.5 m/s
Water flow rate	$Q_J$	7.6-130 cm <sup>3</sup> /s
Surface tension	$\sigma$	0.073 N/m
Air dynamic viscosity	$\mu_G$	1.8E-5 Pa s
Water dynamic viscosity	$\mu_J$	1E-3 Pa s

Dimensionless group	Definition	Range
$We_G$	$\rho_G d_J U_G^2 / \sigma$	3-27
$q$	$\rho_J V_J^2 / \rho_G U_G^2$	13-419
$\sqrt{Bo}$	$\sqrt{\rho_J g d_J^2 / \sigma}$	0.37-3.30
$Oh$	$\mu_J / \sqrt{\rho_J \sigma d_J}$	0.0012-0.0037
$Re_G$	$\rho_G U_G d_J / \mu_G$	818-7364
$Re_J$	$\rho_J V_J d_J / \mu_J$	9570-22805

Table 2.1: The parameter regime explored in this experimental study of a liquid jet in gaseous cross flow.

## 2.3 Observations

Consider a liquid jet of diameter  $d_J$ , density  $\rho_J$ , dynamic viscosity  $\mu_J$ , and surface tension  $\sigma$ , with a flow rate of  $Q_J$  and speed of  $V_J$  moving downward into a uniform gaseous cross flow with density  $\rho_G$ , dynamic viscosity  $\mu_G$ , and speed  $U_G$  (Figure 2-3). The gravitational acceleration is signified by  $g$ . (By reversing the direction of the liquid jet flow, it was verified that gravity did not affect the general structure of the resulting flow.) Nine physical parameters, which are defined in terms of length, mass, and time, govern this system. Therefore, by dimensional analysis, six dimensionless parameters govern the physics of this flow. They are summarized in Table 2.1. Three of the most important parameters are the gaseous Weber number  $We_G$ , the momentum flux ratio  $q$ , and the square root of the Bond number  $\sqrt{Bo} = \sqrt{\rho_J g d_J^2 / \sigma}$ , which is the ratio of the gravitational to surface tension forces acting on the liquid jet. The square root of the Bond number is used rather than the Bond number itself because the former is the same as the important ratio of the liquid jet diameter  $d_J$  to the capillary length  $\kappa^{-1} = \sqrt{\sigma / (g \rho_J)}$ , with the latter having a value of approximately 2.7 mm for water. The Ohnesorge number  $Oh$  indicates the relative importance of the liquid viscosity and the product of the liquid inertia and surface tension. In the present study it assumes values three orders of magnitude below unity which, combined with the relatively high values of the liquid jet Reynolds number (ratio of liquid inertia to viscosity)  $Re_J$  range, indicates that the liquid viscosity is of relatively low importance compared to the other forces at play. The impact of  $Oh$  on the types of instabilities experienced by liquid jets in cross flow is described by [8]. In the range of  $Oh$  found in the present study, the instabilities that affect the flow are independent of this dimensionless parameter. The gaseous Reynolds number  $Re_G$  is the ratio of gaseous inertial to viscous forces. It is also relatively large in this study, making the flow turbulent and unsteady. In what follows, however, turbulence will not be explicitly considered and mean flow properties will be examined.

Figure 2-4 presents three different photographs of a liquid jet in cross flow experiencing bag (partial bubble) instabilities for  $4 \leq We_G \leq 30$ . The image at the left is an example of the previously known (single) bag instability. For the experiment corresponding to this image,  $d_J = 1$  mm, which is less than the capillary length of water,  $We_G = 3$ , and  $q = 351$ . It is clear that there is only a single, discrete bag present at each streamwise position along the jet. This situation has previously been reported in the literature [13, 8, 15].

When the nozzle jet diameter is increased beyond the value of the capillary length, a new type of bag instability can be seen. In this regime, multiple bags can be observed side-by-side at the same jet streamwise position along the flattened jet. This is the case in the image on the right in Figure 2-4. Near the top-left of this photograph, a smaller bag is located in front of another much larger bag whose membrane is beginning to break up. Here  $d_J = 8$  mm (three times the capillary length),  $We_G = 24$ , and  $q = 14$ . Figure 2-5 is the full sequence of images from which the right image in Figure 2-4 was taken. The time between any two sequential photographs in this series is  $613 \mu s$ . It is clear that the rear bag expands and ruptures before the bag in front of it. This does not always occur. It is also possible for multiple side-by-side bags to expand and burst simultaneously. Also, it is possible to have more than two adjacent bags at a particular streamwise location. An example of this can be seen in Figure 2-6, which shows a top view of another instance of multiple bags. Here  $d_J = 5$  mm,  $We_G = 15$ , and  $q = 70$ . The yellow ovals indicate the locations of four discrete, side-by-side bags. Although the appearance of multiple side-by-side bags in a liquid jet in cross flow is new, the existence of two bags from a single drop in a gaseous flow has been recorded, and this phenomenon has been attributed to a Rayleigh-Taylor-like instability similar to that found in the breakup of liquid sheets [13, 16]. In this case, however, the instability is amplified by motion of the liquid/gas interface of the bag because of unbalanced surface tension forces.

The atomization of the relatively large, multiple bags produces sizable droplets and ligaments. These droplets and ligaments often collide with other bags in the multiple bag regime. Such collisions can result in the premature rupture of subsequent bags that form along the jet. This phenomenon increases the efficiency of the atomization process by hastening the breakup of the larger bag structures. However, the droplets in the resulting spray also often collide and merge into even larger droplets and ligaments, which is counterproductive to ultimate atomization of the liquid jet. These structures eventually atomize in secondary breakup stages due to the aerodynamic drag exerted on them by the gaseous cross flow.

For jet nozzle diameters approximately equal to the capillary length (as  $\sqrt{Bo}$  approaches unity), a transition regime between single and multiple bags has been discovered. The center image in Figure 2-4 is an example of this regime, in which the liquid jet actually takes the form of a single, continuous liquid sheet lined with bag-like protrusions. Here  $d_J = 3$  mm,  $We_G = 9$ , and  $q = 33$ . In the transition regime the bags are not discrete as they are in the images on the left and right, but rather all bags merge into a seamless sheet that eventually bursts farther down along the jet. Figure 2-7 is a regime diagram indicating the dependence of the nature of the bag instability on the governing dimensionless parameters  $We_G$  and  $\sqrt{Bo}$  with example photographs highlighting the types of instabilities present for each dimensionless parameter combination. In all regimes, the width of the flattened liquid jet increases with streamwise position along the jet.

The processes of the birth and death of fluid bags are intricate. The following discussion of the birth and death of bags applies equally to both single and multiple side-by-side bags. Figure 2-8 shows a schematic of the formation of an individual bag. Consider an undisturbed liquid column of diameter  $d_J$  and height  $\lambda_C$  moving downward with speed  $V_j$  in the presence of a gaseous cross flow of uniform speed. Throughout the bag formation process, the height of the deformed jet remains the

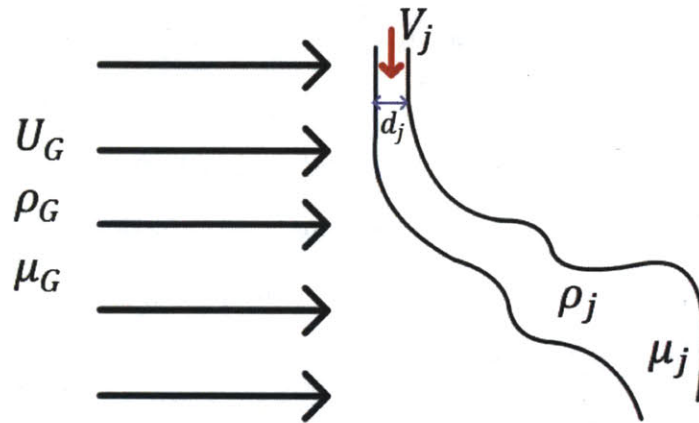


Figure 2-3: A schematic illustration of a liquid jet in gaseous cross flow.

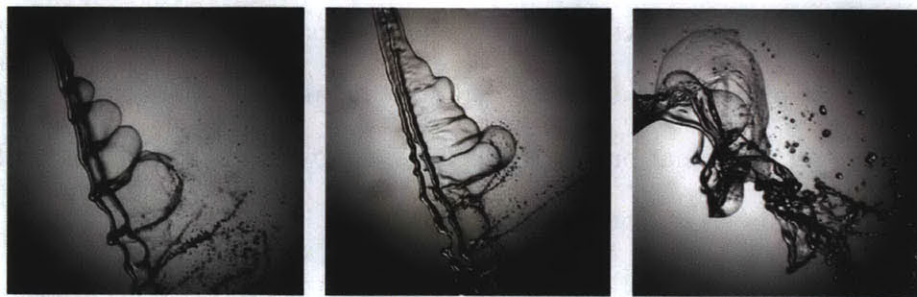


Figure 2-4: Photographs illustrating the single (left), transition (middle), and multiple (right) bag breakup regimes.



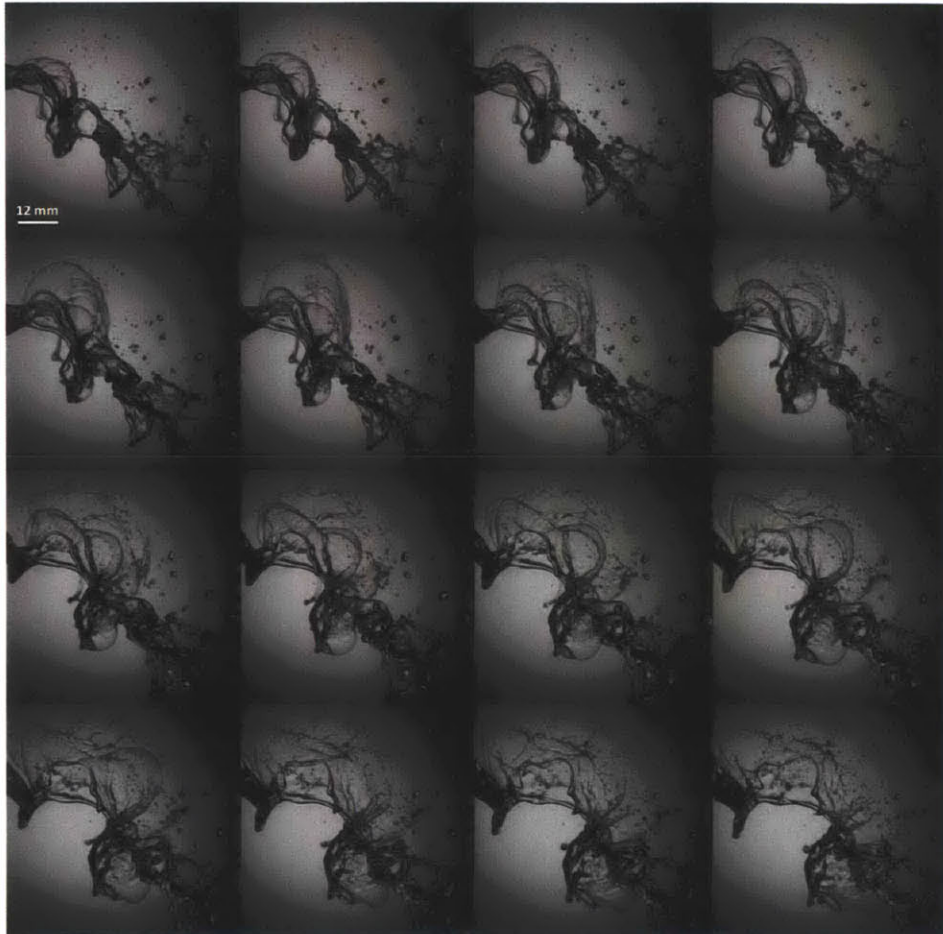


Figure 2-5: The multiple bag instability is observed when the liquid jet nozzle diameter exceeds the capillary length (side view).

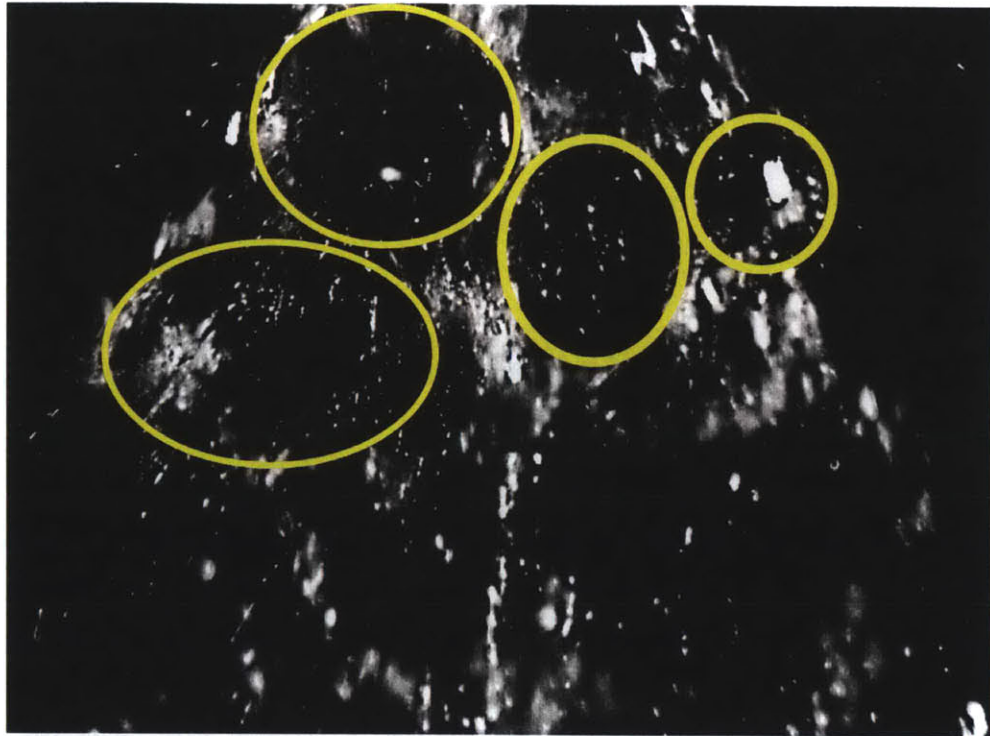


Figure 2-6: Top view of the multiple bag instability. Yellow ovals mark discrete, adjacent bags.

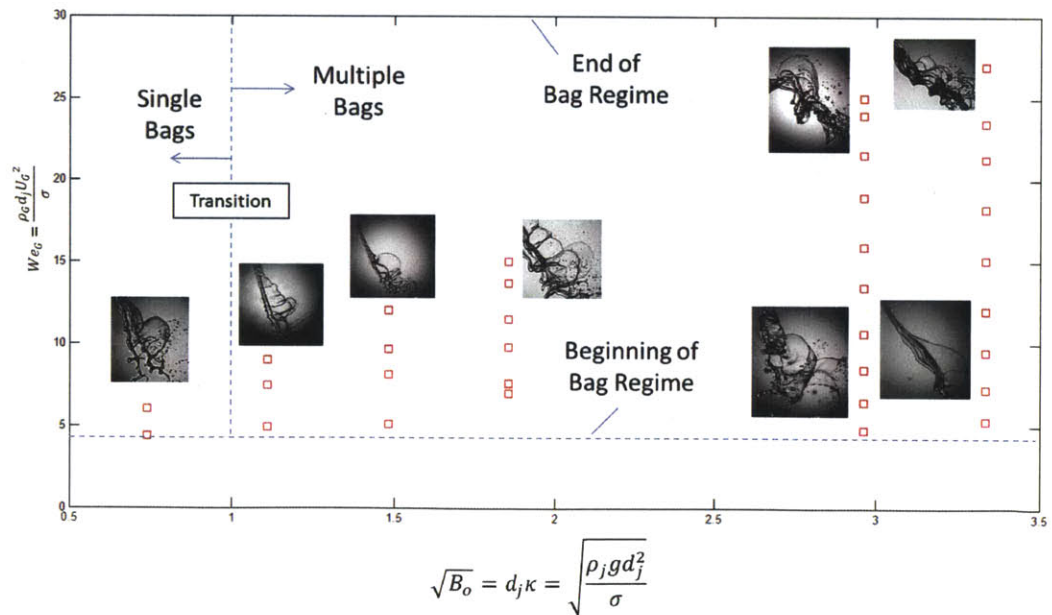


Figure 2-7: Regime diagram illustrating the observed dependence of the development of bags along a liquid jet in cross flow on the governing dimensionless groups.

same as the original height of the column,  $\lambda_C$ . Aerodynamic drag deforms the column into a flattened kidney shape with thickened rims at both edges on the upstream side. Even thicker sphere-like nodes (concentrations of liquid) are present at the top and bottom of each upstream edge of the deformed column. The pressure distribution on the jet causes it to expand in the downstream direction. This is due to both the upstream stagnation pressure on the flattened column as well as the Bernoulli pressure decrease due to the air flowing rapidly around the downstream side of the jet. This expansion results in a partial bubble, or bag, protruding downstream. As the bag membrane expands, the bag rims and nodes continue to move with velocity  $V_j$  in the jet streamwise direction.

The liquid column just described represents a segment of a full liquid jet. The height  $\lambda_C$  is really the wavelength of the upstream jet column waves, which are joined together by the thickened rims and nodes. It is known from prior experimental investigation that for a particular  $We_G$  the value of  $\lambda_C$  is approximately constant both spatially along the length of the jet and over time throughout the experiment in the single bag regime [15]. This has been confirmed in the present study for both the single and multiple bag regimes. Therefore, the invariance of  $\lambda_C$  is independent of  $\sqrt{Bo}$ . Experimental measurements of bag expansion diameters (divided by the initial bag diameter,  $D_0$ ) over time are plotted in Figure 2-9. As shown in this figure, the instantaneous bag diameter at time  $t$ ,  $D(t)$ , is being measured here as the greatest distance from the bag's rim to its membrane. Bag diameters from bags in the single, multiple, and transition regimes are plotted here for a variety of experimental parameters. Time  $t = 0$  and  $D_0$  are measured at the time when the membrane first begins to protrude downstream.

A schematic of the death of a fluid bag is presented in Figure 2-10. As a bag continues to expand, its membrane become thinner and its rims and nodes thicken because of the conservation of mass. Eventually, the bag ruptures in one or more

locations on the bag membrane. A discussion of the rupture locations and the frequency with which bags first tear at each position can be found in [15]. After the bag has ripped, any holes that have appeared begin to expand as the bag diameter itself also continues expanding. The retracting membrane leaves behind a fine mist of droplets and regularly-spaced small ligaments begin to form around each hole with their axes aligned in the direction of membrane retraction. An example of this can be found in Figure 2-12, in which one of the larger ligaments is indicated by the arrow. Throughout the growth of the bag, the bag rims become ever more curved due to the curvature of the bag itself.

When the membrane has fully retracted into the bag rims, the rims themselves break up into a train of uniformly-spaced droplets. During this time, the bag nodes also elongate into ligaments with thickened tips because the bags and their rims have been stretching in the downstream direction (Figure 2-12).  $L(t)$  is the instantaneous ligament length and  $L_b$  is the ligament's length when it begins to break up into a train of droplets that are uniformly spaced. A relevant discussion of the dynamics of ligament expansion can be found in [11]. Experimentally measured breakup properties of these upstream ligaments vs.  $We_G$  for various experimental conditions are plotted in Figure 2-13. In addition to the length of the ligament at breakup,  $L_b$ , the node diameter,  $N_b$ , and average ligament diameter,  $\xi_b$ , at breakup are shown. From the experimental observations, it turns out that all three of these values tend to scale as  $We_G^{-1/3}$  for a variety of experimental conditions (Figure 2-13).

## 2.4 Theory and Comparison with Experiments

The aerodynamic drag of the gaseous cross flow on the liquid jet causes its axis to curve and upstream column waves to form. Let  $R$  and  $\lambda_C$  denote the liquid jet's average radius of curvature and upstream column wavelength, respectively. Here  $\lambda_C$

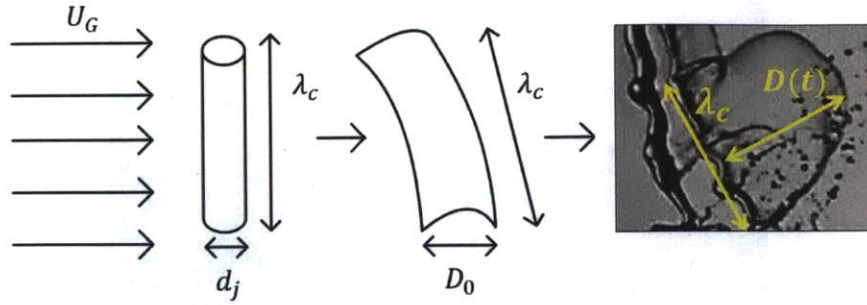


Figure 2-8: Schematic of the formation of a bag.

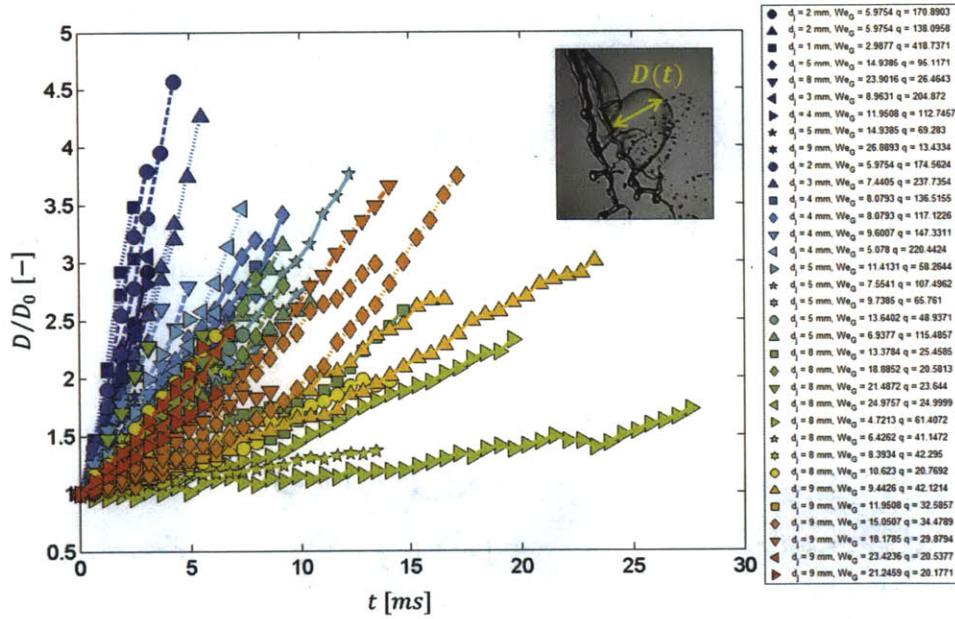


Figure 2-9: Measured temporal bag diameters for a variety of experimental conditions.

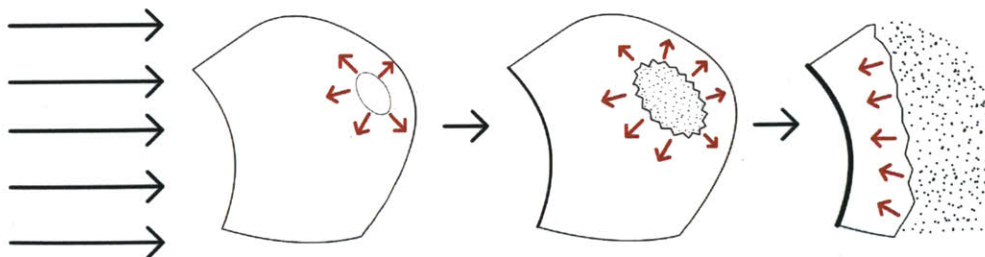


Figure 2-10: Schematic of the rupture and subsequent breakup of a bag.



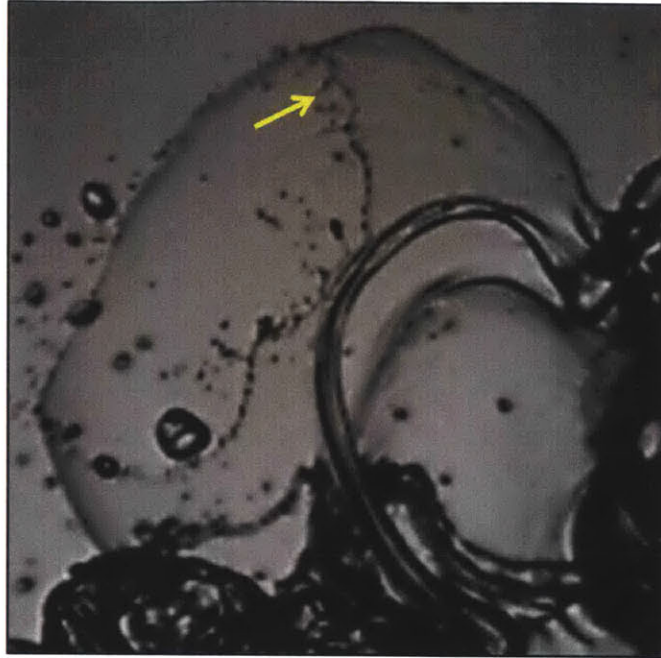


Figure 2-11: Ligaments are formed during bag membrane breakup and retraction (the arrow indicates one of the larger ligaments).

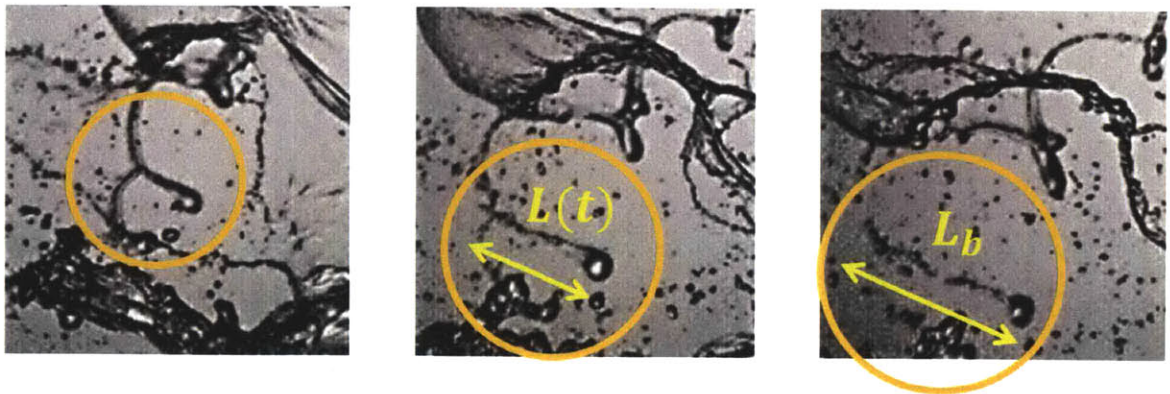


Figure 2-12: Sequence showing the elongation of an upstream ligament (circled) with a thickened tip due to the downstream expansion of the bag and its rims.  $L(t)$  is the instantaneous ligament length and  $L_b$  is the ligament's length when it begins to break up into a train of uniformly-spaced droplets.

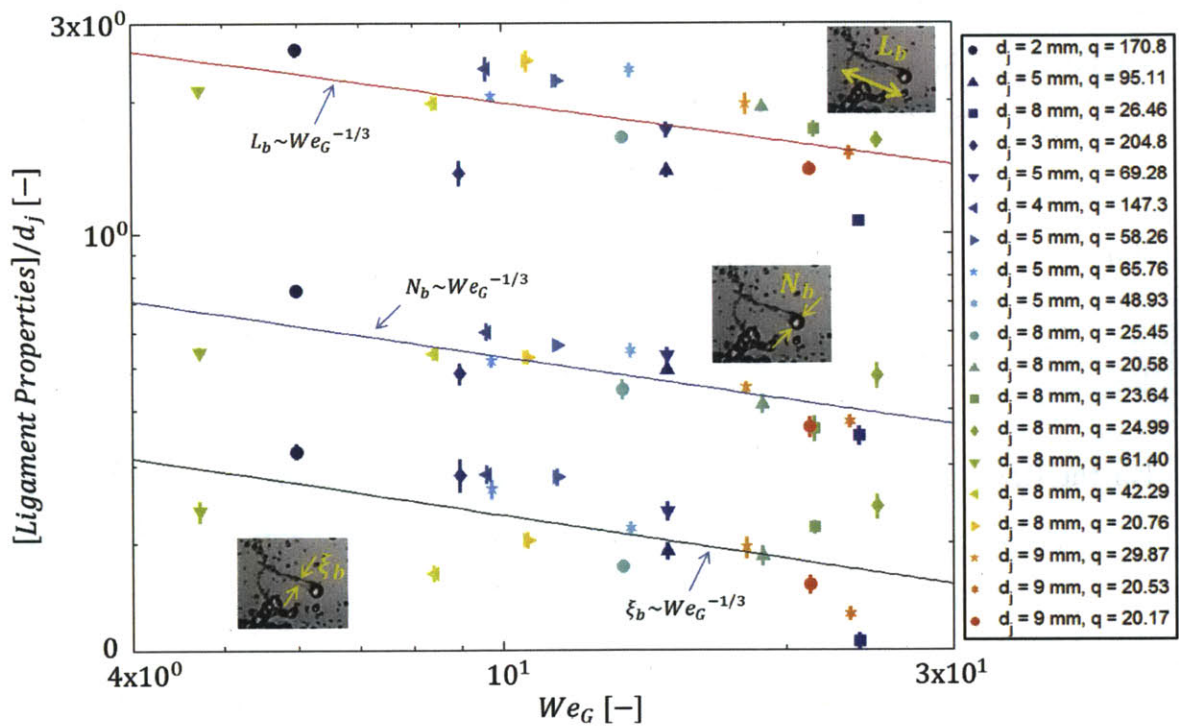


Figure 2-13: Measured ligament dimensions at breakup for a variety of experimental conditions.

is measured diagonally between two consecutive jet nodes (see the inset of Figure 2-14). A Rayleigh-Taylor instability is responsible for the initial destabilization of the jet [17]. Balancing the aerodynamic drag force on a segment of the liquid jet of height  $dl$  and the centripetal acceleration yields the following scaling relationship:

$$C_D \rho_G U_G^2 d_J dl \sim \rho_J d_J^2 a dl, \quad (2.1)$$

where  $C_D$  is the drag coefficient and  $a = V_J^2/R$  is the centripetal acceleration. For a solid cylinder in cross flow for the gaseous Reynolds number range  $1 < Re_G < 2E5$ ,  $C_D \approx 1 + 10Re_G^{-2/3}$  [18]. The liquid jet can be approximated as a solid cylinder for the purposes of the calculation of the drag coefficient [15]. For the range of  $Re_G$  in this investigation, therefore,  $C_D \sim O(1)$ . From Eq. 2.1:

$$\frac{R}{d_J} \sim q. \quad (2.2)$$

For the Rayleigh-Taylor instability, the most unstable wavelength (neglecting viscosity) is proportional to  $\sqrt{(\sigma/((\rho_J - \rho_G)a)} \approx \sqrt{(\sigma/(\rho_J a)}$  since  $\rho_J \gg \rho_G$  [19]. Combining this information with Eq. 2.2 yields the following scaling relationship:

$$\frac{\lambda_C}{d_J} \sim We_G^{-1/2}. \quad (2.3)$$

This scaling law has been experimentally verified for more than two orders of magnitude of  $We_G$ , for various liquids and values of  $V_J$  [17]. Since the regime divisions for liquid jet in cross flow instabilities only depend on  $We_G$  for small  $Oh$ , they are independent of the liquid jet properties. Although Eq. 2.3 was originally derived for the single bag regime, it turns out that it applies to the transition and multiple bag regimes as well. Figure 2-14 presents a plot of experimental values of  $\lambda_C/d_J$  vs.  $We_G$  for various experimental conditions along with the theoretical scaling of Eq. 2.3. The data generally fit the trend of the scaling argument over a wide range of experimental



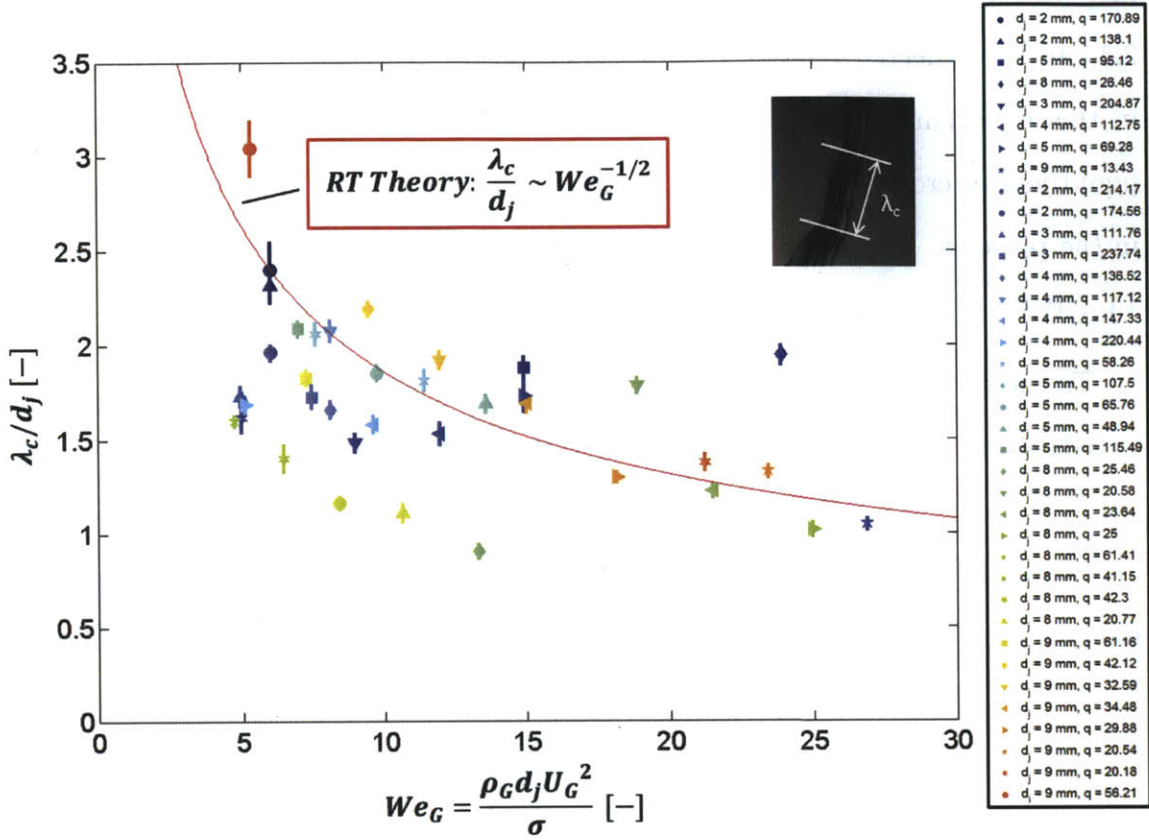


Figure 2-14: Variation of upstream column wavelengths with  $We_G$ . Upstream column waves for liquid jets in cross flow scale similarly with  $We_G$  theoretically and experimentally for both single and multiple bag regimes.

parameters.

Although the beginning of the bag breakup regime for a liquid jet in cross flow has been found in prior investigations experimentally to correspond to  $We_G = 4$ , this bound has not been demonstrated theoretically. In the bag regime, aerodynamic pressure drag on the jet exceeds the Laplace pressure:

$$\frac{1}{2} C_D \rho_G U_G^2 > \sigma \left( \frac{1}{R} + \frac{2}{d_J} \right), \quad (2.4)$$

where  $C_D$  is once again of order unity in this investigation. In the absence of any cross flow,  $We_G = 0$ , and the radius of curvature of the jet is infinity. Even as  $We_G$

increases initially,  $R \gg d_J/2$ . Therefore, the first term on the right-hand side in Eq. 2.4 can be neglected relative to the second term. Rearranging the remaining terms in this equation yields  $We_G > 4$ , in agreement with experimental observations of liquid jets in cross flow. By comparison, experiments have shown that for a droplet in the presence of gaseous flow with  $Oh \ll 1$ , the bag breakup regime  $We_G$  range is  $13 \leq We_G \leq 20$  [20].

To theoretically determine the onset of the multiple bag instability, it is necessary to balance the forces of surface tension and the weight of a fluid bag. For a given  $We_G$ , the weight of the bag equals the surface tension in the transition regime between single and multiple bags. When the weight exceeds the surface tension force, the relatively large volume of liquid makes the formation of single bags unsustainable. The flattened liquid jet is therefore divided into multiple side-by-side bags. The force balance in the transition regime (per unit length) can be expressed as

$$\rho_J g d_J^2 \sim \sigma. \quad (2.5)$$

This force balance can be re-written as

$$\sqrt{Bo} = \frac{d_J}{\kappa^{-1}} \sim O(1), \quad (2.6)$$

which demonstrates that the transition regime occurs for  $d_J \sim \kappa^{-1}$ . The multiple bag instability occurs when  $d_J > \kappa^{-1}$ , and the single bag regime corresponds to  $d_J < \kappa^{-1}$ . These theoretical regime boundaries agree with experimental observations.

For a droplet in a gaseous flow, [16] argue that once a droplet begins to take the form of an expanding bag, surface tension is no longer strong enough to resist the droplet deformation. Therefore, the force balance essentially only involves inertia and the Bernoulli pressure effect. For a segment of a liquid jet in cross flow between two nodes of the upstream column waves, this balance can be expressed as

$$m \frac{d^2 D}{dt^2} \sim \rho_G U_G^2 \lambda_C D, \quad (2.7)$$

where  $m$  is the mass of the columnar jet segment and scales as  $\rho_J d_J^2 \lambda_C$ . Eq. 2.7 can be re-expressed as

$$\frac{d^2 D}{dt^2} \sim CD, \text{ where } C = \frac{\rho_G U_G^2}{\rho_J d_J^2}. \quad (2.8)$$

Eq. 2.8 is a differential equation that has a solution of the form  $D(t) \sim A \exp\{Kt\}$ , where  $A$  and  $K$  are constant determined by initial conditions:

$$D(t = 0) = D_0 \quad (2.9)$$

$$\frac{dD}{dt}(t = 0) \approx 0. \quad (2.10)$$

Eq. 2.9 simply states that at time  $t = 0$  the bag diameter is  $D_0$ , and Eq. 2.10 says that the expansion speed of the bag membrane is essentially zero at time  $t = 0$  (from experimental observations). Combining Eqs. 2.9 and 2.10 with Eq. 2.8 yields the following nondimensionalized scaling relationship for the instantaneous bag diameter:

$$\frac{D(t)}{D_0} \sim \exp \left\{ \sqrt{\frac{\rho_G U_G}{\rho_J d_J}} t \right\}. \quad (2.11)$$

Figure 2-15 presents a plot of the experimentally measured bag diameters over time from Figure 2-9 scaled according to Eq. 2.11, along with a theoretical curve of the relationship in Eq. 2.11 with a proportionality coefficient of unity. The data generally follow the trend indicated by the scaling relationship in Eq. 2.11 for the single, transition, and multiple bag regimes regardless of  $We_G$ ,  $\sqrt{Bo}$ , and  $q$ . An exponential form makes sense because it indicates that the bag membrane accelerates over time due to the higher drag force on the increased bag surface area, which is also

a feature of bag expansion for a droplet in gaseous flow [16].

In order to explain the observed variability in the scaled data in Figure 2-9, it is useful to examine the variability within multiple experimental bag diameter measurements for a single experiment. Figure 2-16 presents ten such measurements for an experiment with  $d_J = 2$  mm,  $We_G = 6$ , and  $q = 175$ . Although the ten different measurements show very good agreement at short times, they begin to diverge at later times. Not only is this due to the fact that the flow is turbulent and unsteady, but the “boundary conditions” of each bag vary, especially at later times. For instance, when a bag bursts, the droplets that it produces may collide with subsequent bags along the jet (the frequency of this happening increases with jet nozzle diameter). The collisions of these droplets with bag membranes could cause premature rupture. Also, due to the variable nature of this turbulent flow, the air velocity conditions around particular bags are often very different. In the transition and multiple bag regimes, the influence of adjacent bags or segments of the jet on a particular bag can also cause its flow conditions to be more variable. The variability observed within this single experiment is on the same order as the maximum difference in the scaled data at later times in Figure 2-15.

## 2.5 Discussion

Figure 2-17 shows an overview of the instabilities that come into play for a liquid jet in cross flow. The single and multiple bag instabilities (birth and death) were discussed in detail in §2.3. The upstream ligament breakup was also mentioned in that section. It turns out that the Rayleigh-Plateau instability is responsible for the breakup of these ligaments. As is generally the case for this instability, the resulting droplets from the atomization of these ligaments are of approximately uniform diameter and spacing (other than the node at the tip, which is an artifact of the jet rim formation

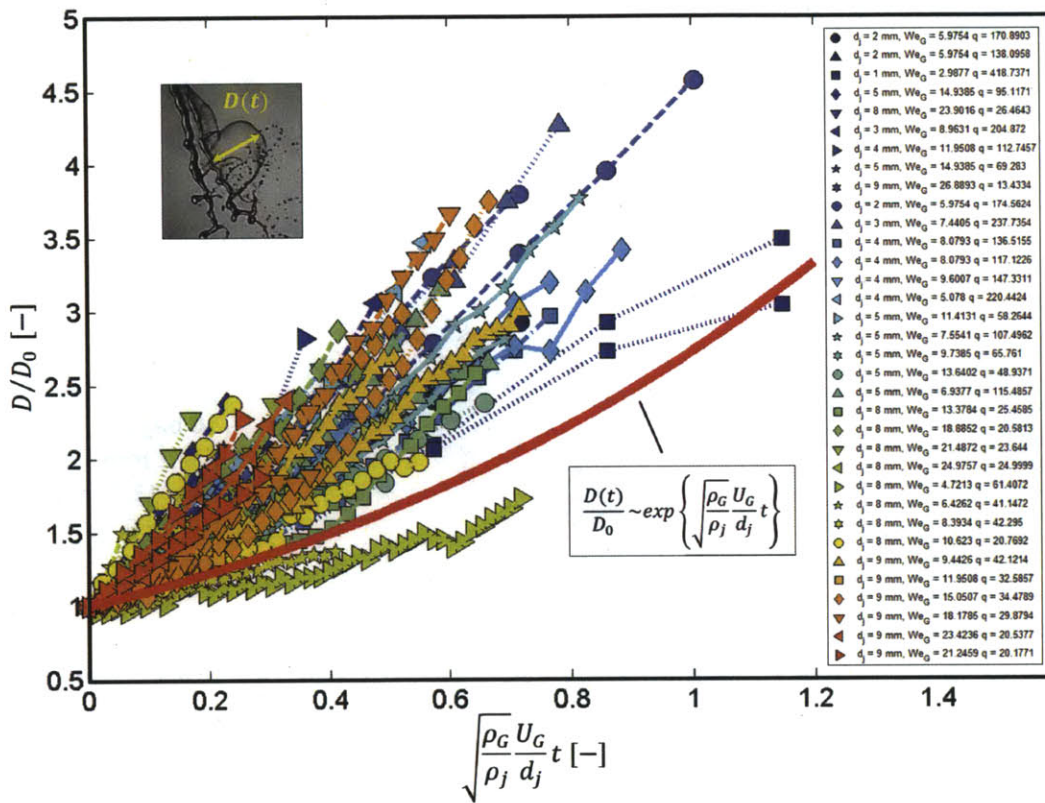


Figure 2-15: Scaled temporal bag expansion diameter. This scaling holds true for both single and multiple bags independent of  $We_G$ ,  $\sqrt{Bo}$ , and  $q$  within the bag breakup regime.

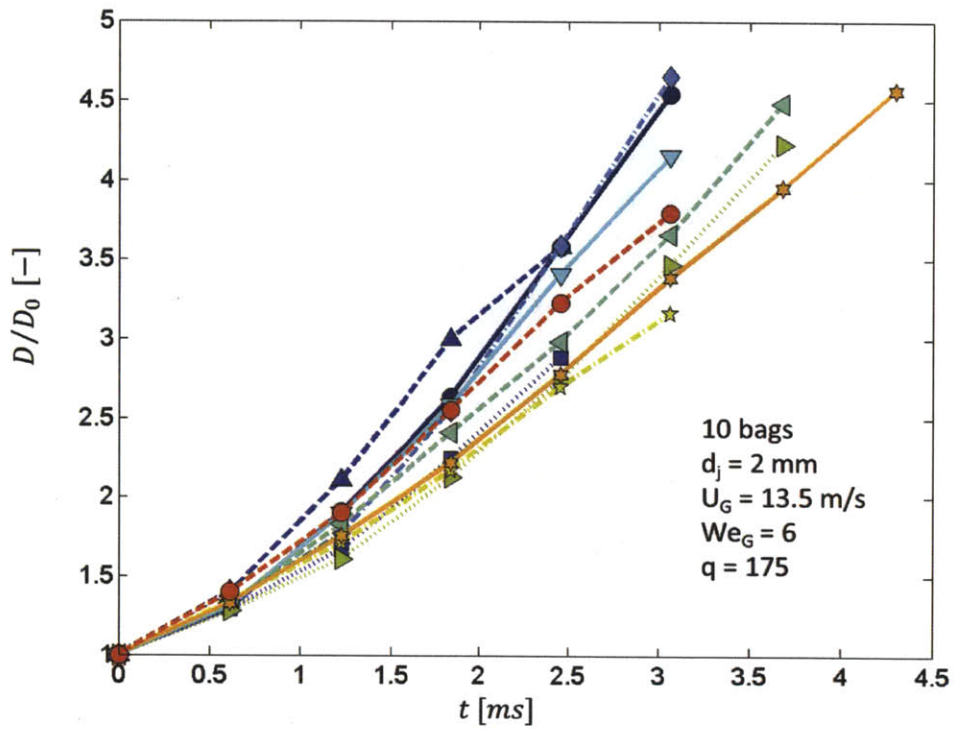


Figure 2-16: Temporal bag expansion diameter variability. Even for different measurements from the same experiment, bag diameter values diverge at later times due to varying flow conditions that exist over time.

during bag expansion). The bag rims also break up due to a similar instability. Once again, approximately uniform droplet diameters and spacing are clearly observed, regardless of the experimental parameters involved in any particular experiment or regime.

The upstream column wavelength instability was described in §2.4. It was identified as a Rayleigh-Taylor instability because it involved the relatively less dense air being accelerated toward the denser water via centripetal acceleration. It also could be conceivable that a Rayleigh-Plateau instability could also be contributing to the destabilization of the jet because this type of instability causes the atomization of liquid jets via capillary forces. However, the Rayleigh-Plateau instability does not take into account  $We_G$ , upon which the upstream column wavelength strongly depends, as shown in Figure 2-14. Even prior to the onset of the bag breakup regime for  $We_G < 4$ , linear stability analysis shows that the aerodynamic drag plays a role in the jet instability, and hence the Rayleigh-Plateau instability cannot explain the physics of the destabilization of the jet in the presence of gaseous cross flow [8].

The bag membrane retraction instability is similar to that which has been observed for bursting bubbles [21]. It is known that the diameter of a hole in a ruptured fluid film expands at the Culick speed:

$$V_C = \sqrt{\frac{2\sigma}{\rho_J h}}, \quad (2.12)$$

where  $h$  is the thickness of the film [22]. In this case,  $V_C$  is the retraction speed of the bag membrane. Combining Eq. 2.12 with the Rayleigh-Taylor most unstable wavelength and the centripetal acceleration  $a_c = V_C^2/(D_b/2)$ , where  $D_b$  is the bag diameter at the time of rupture, yields an expression for the wavelength of the bag membrane retraction instability  $\lambda_{\perp} \sim \sqrt{D_b h}$  [21]. This is the geometric mean of the only two length scales characterizing the bag at the time of rupture.

While this investigation has focused on the primary breakup mechanisms of a

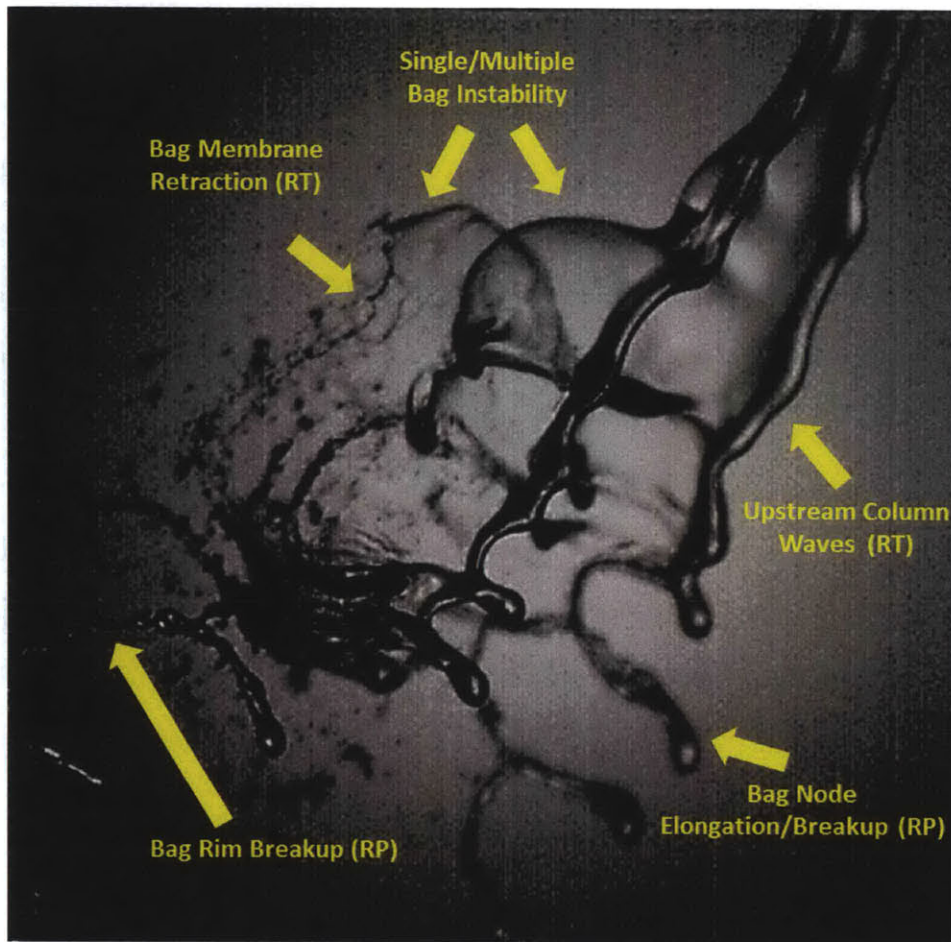


Figure 2-17: Overview of the instabilities that occur in the bag breakup regime. RP signifies the Rayleigh-Plateau instability, while RT is the Rayleigh-Taylor instability.



liquid jet in cross flow, prior studies have measured properties of the spray, such as the distribution of the droplet Sauter mean diameter  $SMD = \sum d^3 / \sum d^2$ , where  $d$  represents droplet diameter [15]. These previous investigations have used two-dimensional imaging techniques to make these measurements. However, spray flows like those produced by liquid jets in cross flow are often very optically dense and many of the droplets and ligaments in the spray may actually be occluded from the camera's view. In order to properly characterize the spray flow characteristics, a three-dimensional imaging technique that can see through such partial occlusions would be preferable. Chapter 3 describes the application of the synthetic aperture imaging technique [1], which is a subset of light field imaging, to the liquid jet in cross flow problem described herein. This use of this technique helps shed greater light on the rich, three-dimensional physics that govern this flow and sprays in general.

## **Acknowledgments**

This work was performed in collaboration with Professors Alexandra H. Techet and John W. M. Bush at MIT.

# Bibliography

- [1] S. P. Lin. Breakup of Liquid Sheets and Jets. Cambridge University Press. 2003.
- [2] C. T. Brown, V. G. McDonell, and B. V. Kiel. Test Bed for Characterization of Liquid Jet Injection Phenomenon at Augmentor Conditions. 42nd AIAA/ASME/SAE/ASEE Joint Propulsion Conference and Exhibit, Sacramento, California. 2006.
- [3] J. Plateau. Statique Experimentale et Theorique des Liquids Soumis aux Seules Forces Moleculaire. Paris: Cauthier Villars. 1, 2: 450-495. 1873.
- [4] Lord Rayleigh. On the Capillary Phenomena of Jets. Proc. R. Soc. London, 29: 71-97. 1879a.
- [5] S. P. Lin and R. D. Reitz. Drop and Spray Formation from a Liquid Jet. Annual Review of Fluid Mechanics, 30: 85-105. 1998.
- [6] N. Ashgriz. Handbook of Atomization and Sprays: Theory and Applications. New York, NY: Springer. 2011.
- [7] E. L. Geary and M. J. Margettes. Penetration of a high velocity gas stream by a water jet. J. Spacecraft 6: 79-81. 1969.
- [8] Y. Kitamura and T. Takahashi. Stability of a liquid jet in air flow normal to the jet axis. J. Chem. Jpn. 9: 282-286. 1976.
- [9] J. A. Schetz and A. Padhye. Penetration and breakup of liquids in subsonic airstreams. AIAA J. 15: 1385-1390. 1977.

- [10] M. Birouk, C. O. Iyogun, and N. Popplewell. Role of viscosity on trajectory of liquid jets in a cross-airflow. *Atomization Spray* 17: 267-287. 2007.
- [11] P. Marmottant and E. Villermaux. On Spray Formation. *J. Fluid Mech.* 498: 73-111. 2004.
- [12] P.-K. Wu et al. Breakup processes of liquid jets in subsonic crossflows. *J. Prop. Power* 13, 64-73. 1997.
- [13] J. Mazallon, Z. Dai, and G. M. Faeth. Primary Breakup of Nonturbulent Round Liquid Jets in Gas Crossflows. *Atomization and Sprays* 9: 291-311. 1999.
- [14] K. Sallam, C. Aalburg, and G. Faeth. Breakup of Round Nonturbulent Liquid Jets in Gaseous Crossflow. *AIAA Journal* 42 (11): 2529-2540. 2004.
- [15] C.-L. Ng et al. Bag breakup of nonturbulent liquid jets in crossflow. *Int. J. of Multiphase Flow* 34: 241-259. 2008.
- [16] É. Reyssat et al. Shape and instability of free-falling liquid globules. *EPL* 80: 34005. 2007.
- [17] J. Eggers and E. Villermaux. Physics of liquid jets. *Rep. Prog. Phys.* 71: 036601. 2008.
- [18] F. M. White. *Viscous Fluid Flow*. Mc-Graw-Hill, Inc. 1991.
- [19] S. Chandrasekhar. *Hydrodynamic and Hydromagnetic Stability*. Oxford: Oxford Univ. Press. 1961.
- [20] L.-P. Hsiang and G. M. Faeth. Near-Limit Drop Deformation and Secondary Breakup. *Int. J. Multiphase Flow* 18: 635-652. 1992.
- [21] H. Lhuissier and E. Villermaux. Bursting Bubbles. *Phys. Fluids* (21). 2009.
- [22] F. E. C. Culick. Comments on a ruptured soap film. *J. Appl. Phys.* 31: 1128-1129. 1960.

- [23] J. Belden, T. T. Truscott, M. Axiak, and A. H. Techet. Three-dimensional synthetic aperture particle image velocimetry. *Meas Sci Technol* 21:1-21. 2010.



# Chapter 3

## Application of LFI & SA

### Refocusing Techniques to a Liquid Jet in Cross Flow

#### 3.1 Introduction

As was demonstrated in the previous chapter, the destabilization and atomization of a liquid jet in cross flow is a highly complex three-dimensional (3D) problem. Liquid jets in cross flow are multiphase flows that involve dense cores and sprays of droplets and ligaments. Traditional imaging techniques have been unable to fully resolve these optically dense segments of the flow and to identify the locations of fine structures. Although two-dimensional (2D) imaging is able to provide some insight into the dynamics of spray formation in this case, 3D resolution is ultimately required in order to better grasp the physics involved and to record data that can be used to improve and validate 3D numerical simulations of sprays. Due to its non-invasive nature and the ability to “see through” partial occlusions, light field imaging (LFI) and synthetic aperture (SA) refocusing techniques (see [1]) have been combined to study this flow field in 3D. This technique is aptly suited for sprays, particle laden

and multiphase flows, as well as complex unsteady and turbulent flows. Synthetic aperture imaging, which is a subset of light field imaging, involves recording as many light rays from a scene as possible [2, 3]. In practice, one method used by researchers in the imaging community for sampling a large number of rays is to use a camera array [3, 4] or more recently, a single imaging sensor and a small array of lenslets (lenslet array) in a plenoptic camera (e.g. [5]). Once the light rays have been captured, they can be reparameterized using a synthetic aperture refocusing algorithm. This involves reprojecting in-focus images from different cameras onto planes throughout the image volume and recombining them in some way to form refocused images [6]. In the refocused images, features that are actually located at a particular depth in the image volume are seen as being in-focus, while other features that are not located there appear blurred [2, 3].

Flow features, such as individual droplets, can be located in 3D by refocusing throughout the volume and extracting features on each plane. An implication of the refocusing is the ability to see through partial occlusions in the scene. This emerging method extends measurement capabilities in complicated flows where knowledge is incomplete. Utilization of this technique allows for finer measurements of flow quantities and structures that would have been impossible with prior methods. In particular, this imaging system is designed to measure and locate features such as bubbles, droplets and particles in three spatial dimensions over time in multiphase flows. Other measurement systems often only allow practitioners to measure average quantities or envelopes of flow regions that do not require such high resolution. This new technique has already demonstrated the capability to resolve very fine flow features, which is especially important in multiphase and turbulent flow fields like sprays that contain very minute flow structures and length scales. Here the synthetic aperture method is reviewed and a simulated example is presented to help demonstrate its capabilities. Then application of this technique to a liquid jet in cross flow



is presented. It is shown that it is possible to resolve both optically sparse and dense flows in 3D.

## 3.2 Synthetic Aperture Imaging

### 3.2.1 Principle

To obtain 3D volumetric data sets for spray fields, a planar array of cameras was implemented to record the scene from different angles. Synthetic aperture refocusing techniques were applied to the raw camera array images, each with large depths of field, to obtain a stack of post-processed images, with narrow depth of field, where each image in the stack is located on a specific focal plane. In general, the post-processing for synthetic aperture refocusing involves projecting all images onto a focal surface (planar or otherwise) in the scene on which the geometry is known, averaging the projected images to generate one image, and repeating for an arbitrary number of focal planes (see [1] for more details).

Image capture is performed using an array of cameras typically arranged in a multi-baseline stereo configuration, which view the scene from different viewpoints. The cameras can be placed at arbitrary locations and angles as long as the desired refocused planes (image volume) are in the field of view of each camera. The depth of field of each camera is set large enough such that the entire volume of interest is in focus. Accurate calibration is also critical in the reparameterization and requires advanced auto-calibration algorithms.

The starting point for volume reconstruction is the implementation of the synthetic aperture algorithm to generate refocused images on planes throughout the volume. Thereafter, the actual particle field must be extracted from the refocused images and organized into a volume with quantifiable locations. First, mapping functions must

be established between the camera image planes and world coordinates

$$\mathbf{u}_j^i = F(\mathbf{X}_j; p^i) \quad (3.1)$$

where  $u_j$  is the 2x1 vector of the  $j^{\text{th}}$  image point coordinates,  $[u_j, v_j]^T$ ,  $X_j$  is the 3x1 vector of the  $j^{\text{th}}$  world point coordinates,  $[X_j, Y_j, Z_j]^T$ ,  $p^i$  is a set of parameters defining the model of the  $i^{\text{th}}$  camera, and  $F$  defines the form of the model. This model allows each image from each of the  $N$  cameras in the array to be projected onto  $k$  focal planes.  $I_{FP_{ki}}$  denotes the image from camera  $i$  aligned on the  $k^{\text{th}}$  focal plane. The resulting, refocused SA image,  $I_{SA_k}$ , may be generated by averaging each of these images over the number of cameras in the array

$$I_{SA_k} = \frac{1}{N} \sum_{i=1}^N I_{FP_{ki}} \quad (3.2)$$

where  $I_{SA_k}$  is the image from camera  $i$  aligned on the  $k^{\text{th}}$  focal plane and  $N$  is the number of cameras [6]. Combining images using this averaging technique is known as additive refocusing. A variant of the additive SA algorithm that can enhance signal-to-noise ratio for well calibrated images is given by the multiplicative refocusing algorithm

$$I_{SA_k} = \prod_{i=1}^N [(I_{FP_{ki}})^n] \quad (3.3)$$

where  $n$  is an exponent between zero and one. This allows for enhancement of the signal-to-noise ratio without letting any camera with an occluded view of an object prevent that object from being refocused, because a small number raised to an exponent between zero and one is non-zero. It has been determined that  $n$  in the range  $\frac{1}{5} \leq n \leq \frac{1}{3}$  works best. It has been found that the most efficient number of cameras is in the range of 10–15 [1]. This was determined by comparing a synthesized image intensity field to a reconstructed one. The value of  $Q$ , defined as follows, is maximized

in the range of 10–15 cameras

$$Q = \frac{\sum_{XYZ} [E_r(X, Y, Z) * E_s(X, Y, Z)]}{\sqrt{\sum_{XYZ} E_r^2(X, Y, Z) * \sum_{XYZ} E_s^2(X, Y, Z)}}, \quad (3.4)$$

where  $E_r$  is the reconstructed intensity field and  $E_s$  is a synthesized intensity volume based on the known particle locations.

### 3.2.2 Simulation to Demonstrate the Method

In order to demonstrate and further verify the codes involved in the auto-calibration and synthetic aperture refocusing method, a simulation was created using Blender, a 3D simulation software package. Nine cameras (Figure 3-1), lighting, a calibration grid, and a translucent sphere were simulated in order to provide a convenient, modifiable testbed for this technique. The following parameters are fully adjustable in the Blender simulation either manually or via a script: 3D location of all objects, Euler rotation angles of all objects, focal length, sensor size, and depth of field of cameras, refractive indices of materials, lighting, and render format, resolution, and quality. Figure 3-2 presents nine simulated images of a chessboard calibration grid (in air) in a particular orientation and at a certain position from each camera in the simulated array. This simulated grid was moved throughout the image volume and recorded at nine different locations and orientations. (The background of the grid images in Figure 3-2 is arbitrary.) Each of the calibration images was processed using an adaptation of the chessboard grid point extraction algorithm described in [7]. Figure 3-3 shows a three-dimensional plot of the grid points relative to each other. After the grid points from each of the calibration image planes were extracted and the individual camera image coordinates were aligned with real world points, the raw data images of a simulated 5 mm diameter translucent sphere shown in Figure 3-4

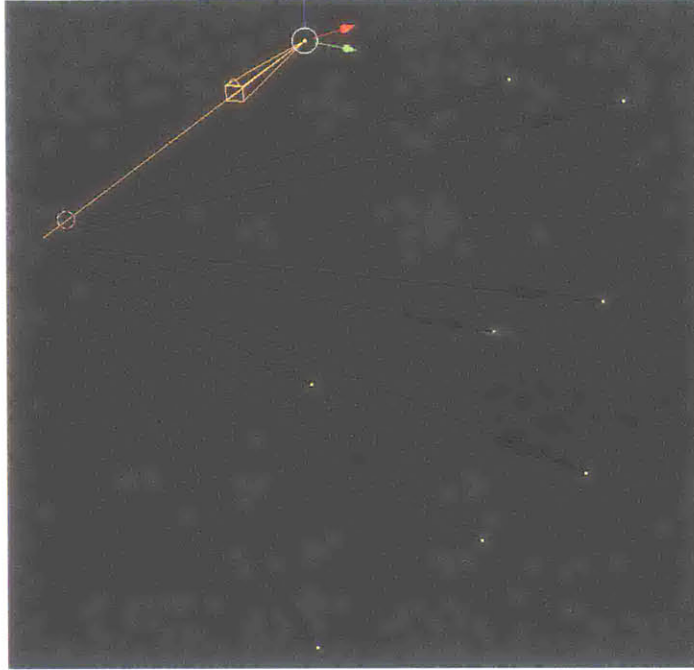


**Figure 3-1: Simulated camera array in Blender.**

were processed. Three sample refocused planes are shown in Figure 3-5. The center image is the focal plane located at the actual center of the sphere. The left and right images are the focal planes 3 mm in front of and behind the center of the sphere, respectively. In the center image, the edge of the sphere is in sharp focus, while in the other two images the sphere is out of focus. This is because the sphere is physically located at the focal plane of the central image, but nothing is present at the other two depths. The reason the left and right images are not blank is due to ghosting from the sphere. This issue is discussed by [6].

### **3.3 Liquid Jet in Cross Flow**

A round water jet was pumped downward through a nozzle into a horizontal wind tunnel to generate a liquid jet in cross flow spray. The apparatus is described in

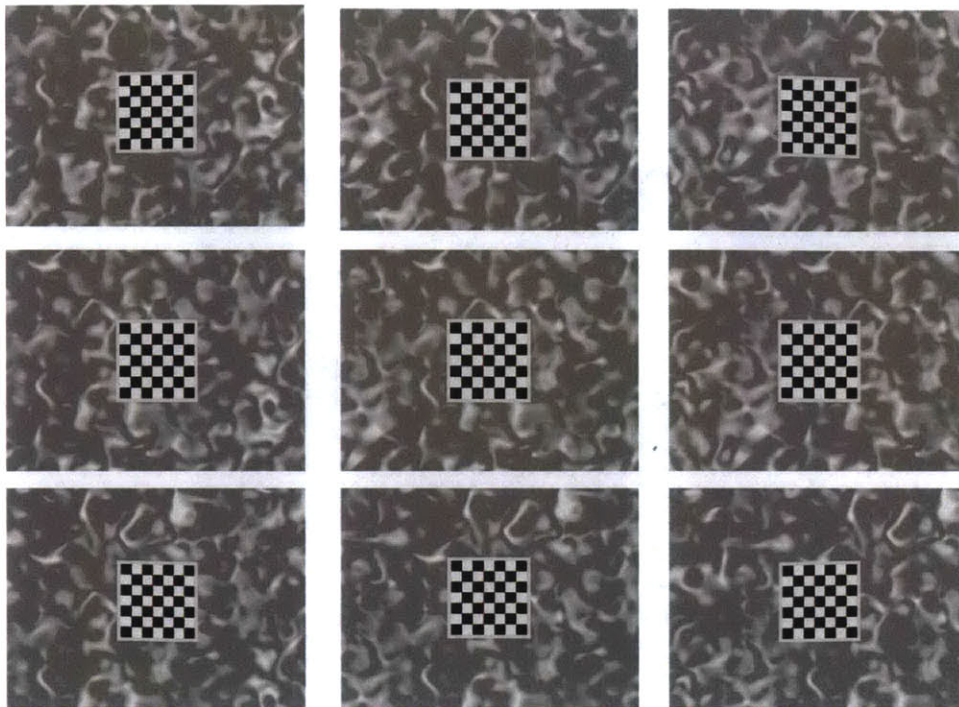


Figure 3-2: Simulated images from each of the nine simulated cameras of a chessboard calibration grid at particular orientation.

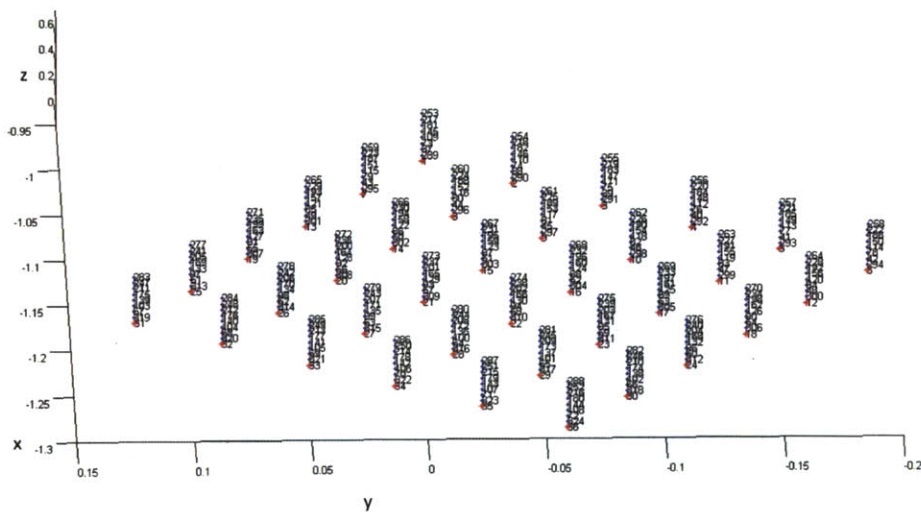


Figure 3-3: A three-dimensional plot of the relative locations of the grid points from all of the simulated calibration images, including those shown in Figure 3-2.

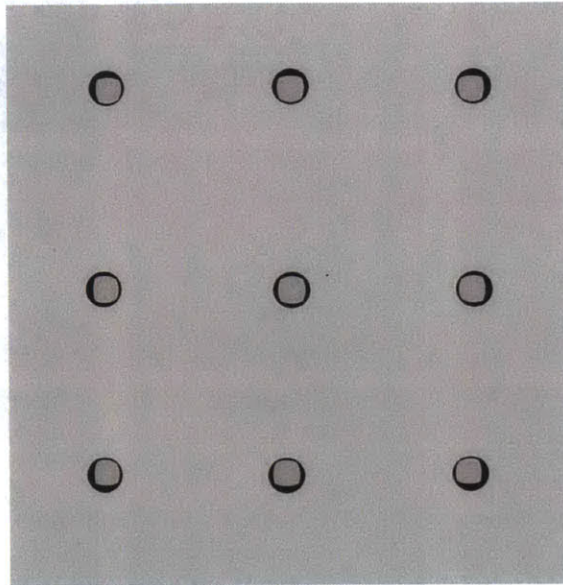


Figure 3-4: Simulated raw images from each of the nine simulated cameras of a translucent sphere with a diameter of 5 mm.

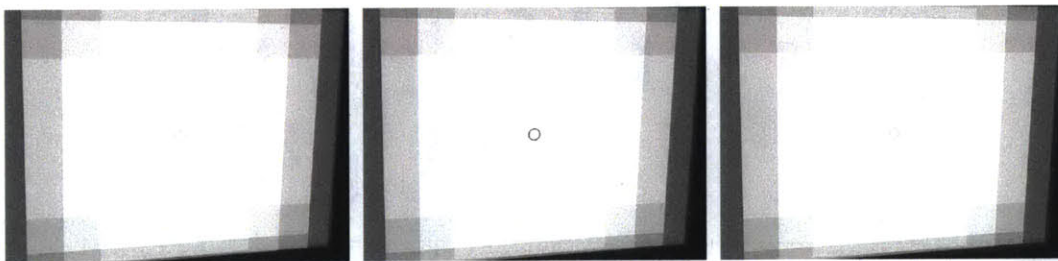


Figure 3-5: Refocused images of the 5 mm diameter translucent sphere corresponding to the raw images in Figure 3-4.

detail in the previous chapter. In the experiments described here, a 5 mm diameter jet nozzle diameter was used and the cross flow air velocity was 13.5 m/s. This is the case corresponding to the raw images shown in Figure 3-6, for which the gaseous Weber number was 15:

$$We_G = \frac{\rho_G U_G^2 d_J}{\sigma}, \quad (3.5)$$

where  $\rho_G$  is the density of the gas,  $U_G$  is the velocity of the gas,  $d_J$  is the liquid jet nozzle exit diameter, and  $\sigma$  is the surface tension. Since  $4 \leq We_G \leq 30$  in this case, the jet suffers from a bag breakup instability instead of a shear breakup with more ballistic spray formation seen at higher  $We_G$  (e.g. see [8]). More precisely, since the nozzle diameter here is greater than the capillary length of water (2.7 mm), a multiple bag breakup instability is present (see the previous chapter for more details).

In this bag breakup regime, fluid bags are formed and then rupture forming a spray of small droplets. The droplets resulting from a bursting bag were imaged using a square nine-camera imaging array. The images were processed using the light field imaging and synthetic aperture refocusing algorithms as described above that were written in MATLAB. The cameras used in all of the experiments presented herein were monochrome Manta GigE cameras from AVT. All of the cameras in the array were synced and simultaneously captured 1024 x 768 pixels, 8 bit, monochromatic images at 30 frames per second maximum. Although this frame rate was not high enough to achieve fine temporal resolution, it was effective for recording images that could be refocused and from which flow structures, such as droplets and ligaments, could be extracted and investigated. High-speed cameras were used by [9] with similar success but significant cost increase. Each camera was equipped with a Sigma 105 mm lens and F-to-C mount adapter. The cameras were arranged in a planar array mounted on tripods with Giottos ball head mounts. All cameras were oriented at angles such they could all record the same image volume simultaneously. The spray was back

illuminated by a pulsed LED light bank, which could be synchronized with the camera frame rate; a common light diffuser, such as that used by professional photographers, was used to create uniform, diffuse lighting. An auto-calibration method relying on a pinhole model was utilized to establish a mapping function between the image planes and world coordinates [6]. For all calibrations, a checkered grid with  $1\text{ mm}^2$  grid squares was randomly moved and recorded in different orientations throughout the focal volume for each set of experiments (Figure 3-7). It was important to make sure that the calibration plate was in focus in every image by each camera in the array to ensure that the auto-calibration and refocusing algorithm would succeed in reconstructing the volume [7].

Using the reconstruction algorithm it is possible to determine the position of in-focus spray droplets at this time instant using the raw images in Figure 3-6. Figure 3-8 shows three planes within the reconstructed volume, highlighting sample individual droplets (yellow ovals) that are in focus on one of three z-planes in the focal stack. The in-focus features at each depth are in sharp focus, while features not physically located at those depths are blurred. Therefore, using this method it is possible to locate features in 3D in the spray flow. A multiplicative exponent of  $1/3$  (see Eq. 3.3) was used to produce the images in this figure.

The cameras that recorded the images in the lower right hand quadrant of Figure 3-8 look up through additional fluid bags that have not yet burst. These bags are not completely refocused in this particular synthetic aperture refocusing experiment because they are not in view in all images. The droplets and ligaments in the spray were the main features of interest here. The bags could be refocused if the cameras are less zoomed in or if different lenses are used to expand the field of view so that the bags are fully in view in every image. Figures 3-9 through 3-12 present additional examples of the synthetic aperture refocusing method applied to the spray resulting from a liquid jet in cross flow. These images focus more on the droplets and ligaments





**Figure 3-6: Raw images from nine camera square array. Lower right hand quadrant of images look up through additional fluid bags that have not yet burst. A fine mist of spray droplets generated from burst fluid bags is observed. The nozzle diameter was 5 mm, the air speed was 13.5 m/s, and the gaseous Weber number was 15.**

of the resulting spray than the bags. Fewer in-focus features can be seen in Figures 3-10 and 3-12 because the cameras in the array were aimed at a position farther downstream from the liquid jet. Therefore, the spray was not as optically dense at this location. Once again, a multiplicative exponent of  $1/3$  was used to refocus the raw images in Figures 3-9 and 3-11. Thresholding and droplet identification algorithms can automate the determination of spray droplet size and location, similar to the work on bubbles presented in [9]. Further investigations are ongoing to develop more robust droplet detection algorithms for light field imaging applications.

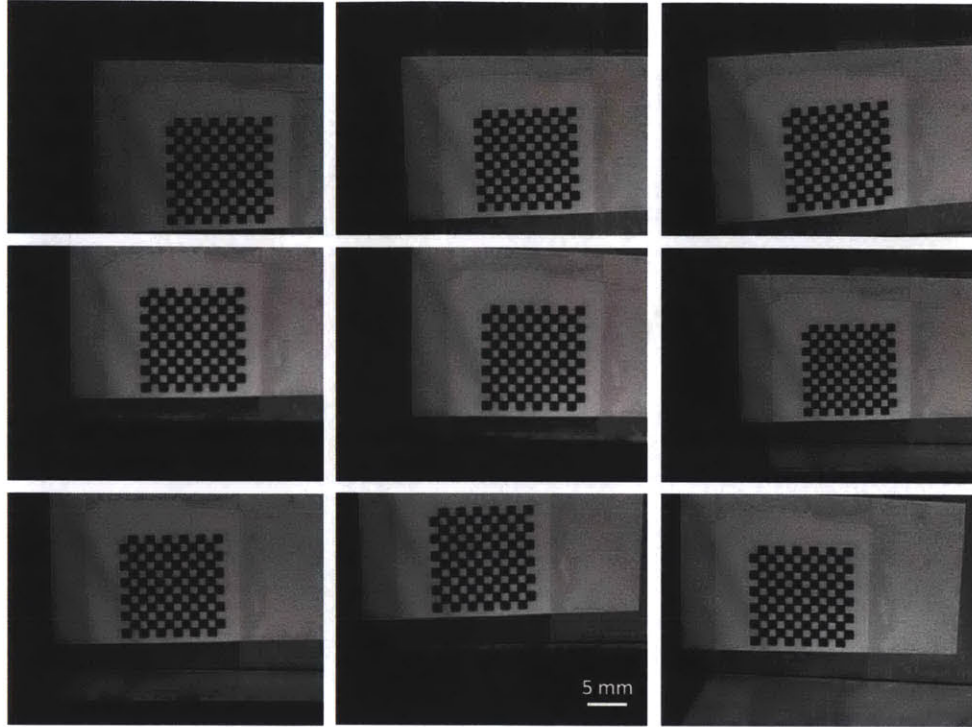


Figure 3-7: Sample calibration grid images for a particular grid orientation from each of the nine cameras in the array.

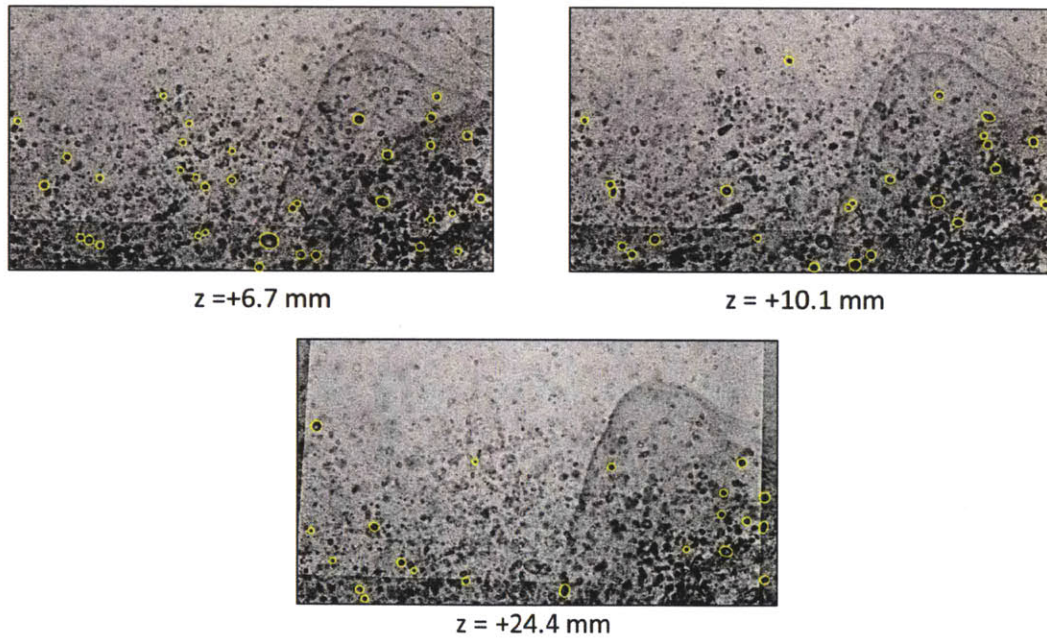


Figure 3-8: Refocused images corresponding to the raw images shown in Figure 3-6 at three z-planes in focal stack:  $z = +6.7 \text{ mm}$  (top-left),  $+10.1 \text{ mm}$  (top-right), and  $+24.4 \text{ mm}$  (bottom);  $z = 0 \text{ mm}$  was chosen arbitrarily. In-focus features on each focal plane are indicated.





Figure 3-9: Raw images from nine camera square array. Lower right hand quadrant of images look up through additional fluid bags that have not yet burst. A fine mist of spray droplets generated from burst fluid bags is observed. The nozzle diameter was 5 mm, the air speed was 13.5 m/s, and the gaseous Weber number was 15.

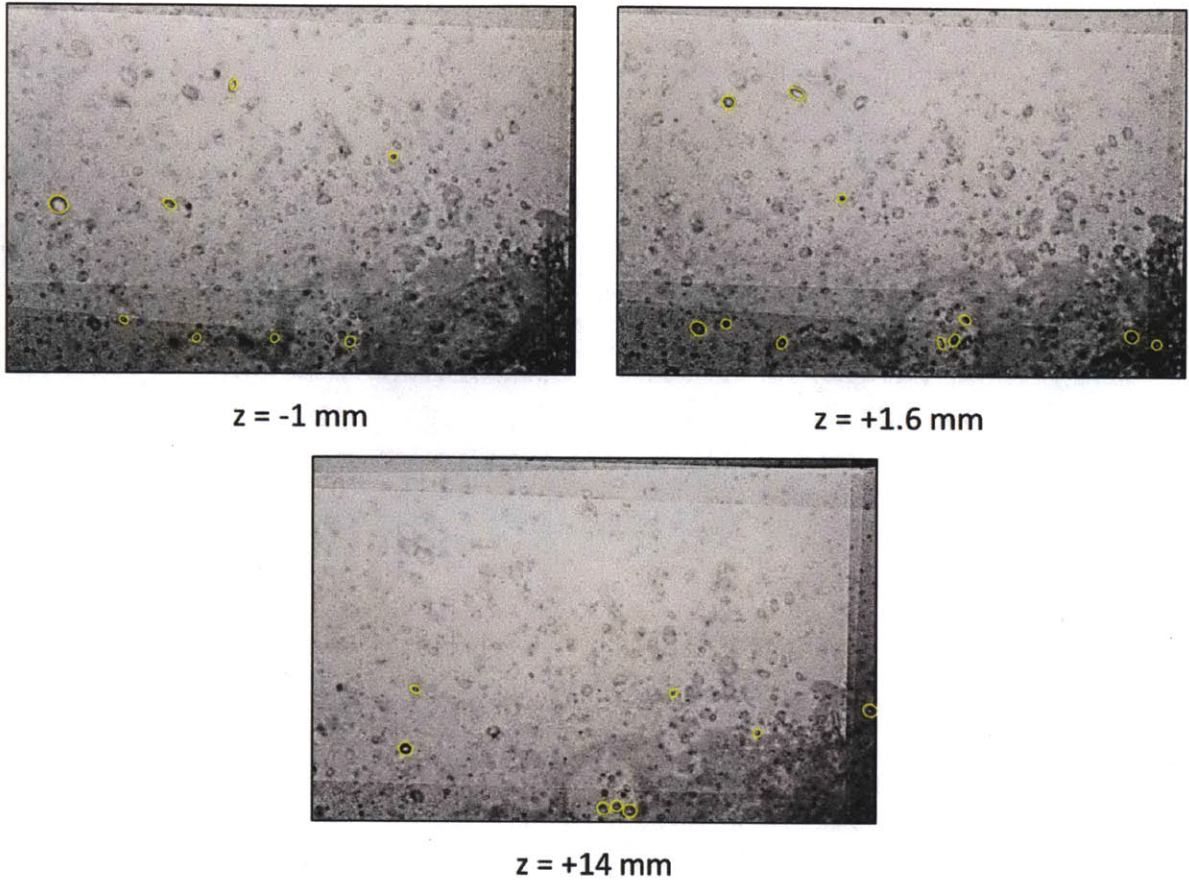


Figure 3-10: Refocused images corresponding to the raw images shown in Figure 3-9 at three  $z$ -planes in focal stack:  $z = -1 \text{ mm}$  (top-left),  $+1.6 \text{ mm}$  (top-right), and  $+14 \text{ mm}$  (bottom);  $z = 0 \text{ mm}$  was chosen arbitrarily. In-focus features on each focal plane are indicated.

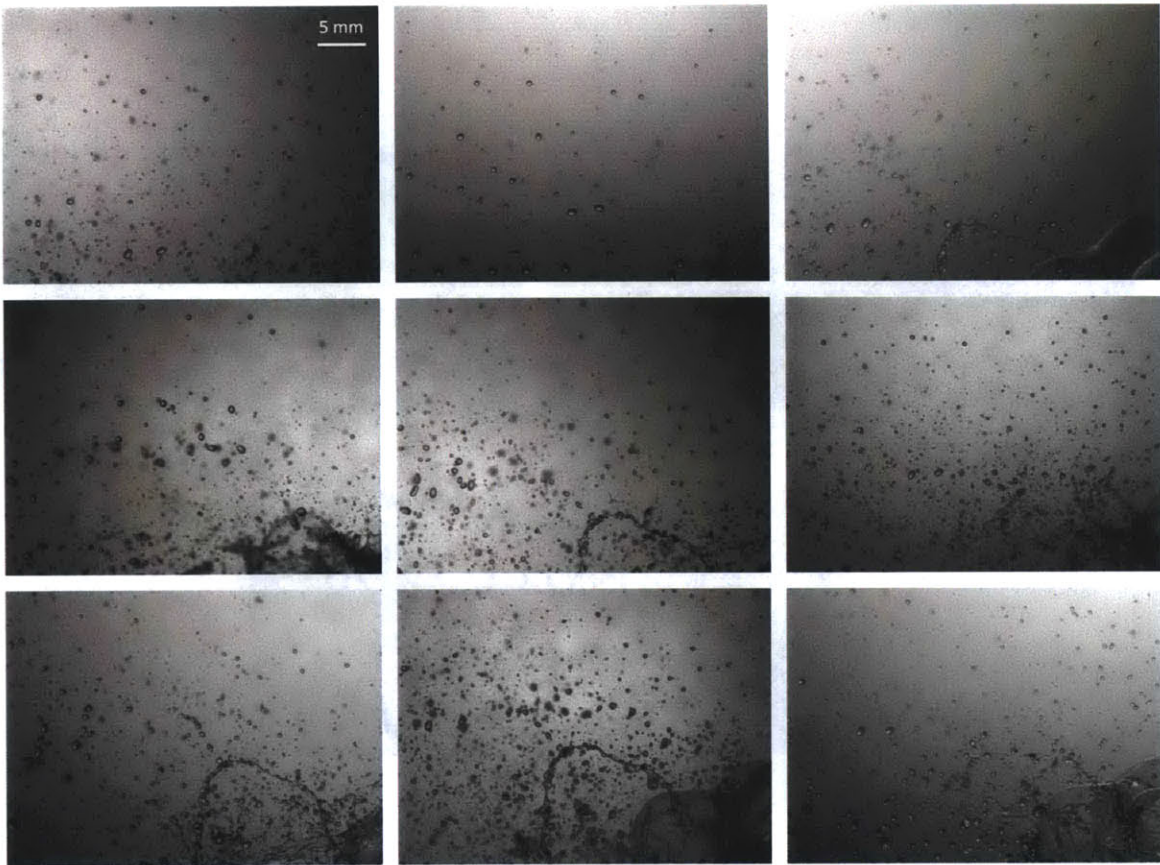
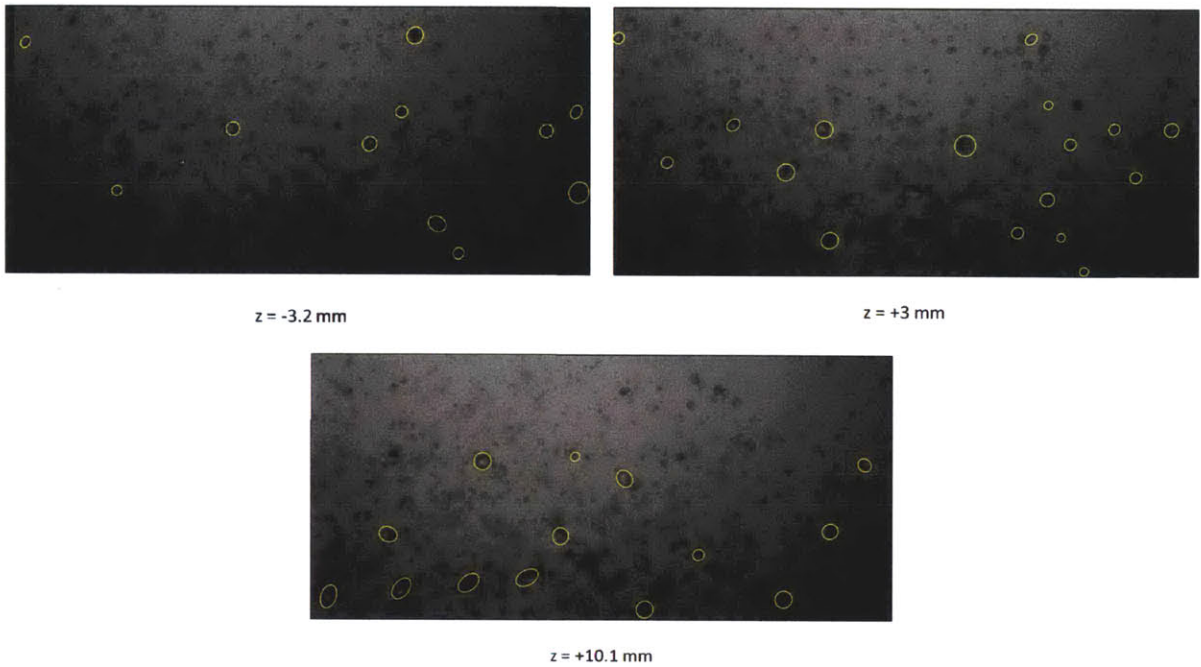


Figure 3-11: Raw images from nine camera square array. Lower right hand quadrant of images look up through additional fluid bags that have not yet burst. A fine mist of spray droplets generated from burst fluid bags is observed. The nozzle diameter was 5 mm, the air speed was 13.5 m/s, and the gaseous Weber number was 15.





**Figure 3-12:** Refocused images corresponding to the raw images shown in Figure 3-11 at three z-planes in focal stack:  $z = -3.2$  mm (top-left),  $+3$  mm (top-right), and  $+10.1$  mm (bottom);  $z = 0$  mm was chosen arbitrarily. In-focus features on each focal plane are indicated.

## 3.4 Conclusions

Spray flows are typically highly unsteady, three-dimensional, and often densely saturated with droplets that impact other droplets, coalesce and break up. Droplets, fluid ligaments, and bags can form from fluid streams and sheets being accelerated in air cross flows. This work shows the potential for imaging such complex features with emerging three-dimensional imaging methods derived from the combination of light field imaging and synthetic aperture refocusing. These techniques were successfully applied to a liquid jet in cross flow in the bag breakup regime. It has been shown that it is possible to resolve and locate flow features accurately in 3D. Ultimately these advances, along with others coming from the vision community, hold great potential for opening doors to previously under-sampled unsteady, turbulent, multiphase fluid flows.

### Acknowledgments

Thanks to Abhishek Bajpayee from MIT for producing the simulated calibration and data images in Blender.





# Bibliography

- [1] J. Belden, T. T. Truscott, M. Axiak, and A. H. Techet. Three-dimensional synthetic aperture particle image velocimetry. *Meas Sci Technol* 21:1-21. 2010.
- [2] A. Isaksen, L. McMillan, and S. J. Gortler. Dynamically reparameterized light field SIGGRAPH '00: Proc. 27th Ann. Conf. on Computer Graphics and Interactive Techniques (New York: ACM Press/Addison-Wesley) 297–306. 2000.
- [3] V. Vaish, G. Garg, E. Talvala, E. Antunez, B. Wilburn, M. Horowitz, and M. Levoy. Synthetic aperture focusing using a shear-warp factorization of the viewing transform. Proc. IEEE Computer Society Conf on Computer Vision and Pattern Recognition (CVPR05')—June Workshops. Los Alamitos, CA: IEEE Computer Society Press 3:129. 2005.
- [4] V. Vaish, B. Wilburn, N. Joshi, and M. Levoy. Using plane + parallax for calibrating dense camera arrays Proc. 2004 IEEE Computer Society Conf. on Computer Vision and Pattern Recognition (CVPR04') (June–July 2004) v. 1, (Los Alamitos, CA: IEEE Computer Society Press, 2–9. 2004.
- [5] K. Lynch. Development of a 3-D Fluid Velocimetry Technique based on Light Field Imaging, MS Thesis, Auburn University, Auburn, Alabama. 2011.
- [6] J. Belden. Synthetic Aperture Imaging for Three Dimensional Resolution of Fluid Flows. Ph.D. Thesis. Massachusetts Institute of Technology. 2011.
- [7] A. Kassir and T. Peynot. “Reliable Automatic Camera-Laser Calibration.” Proceedings of the 2010 Australasian Conference on Robotics & Automation. 2010.

- [8] K. Sallam, C. Aalburg, and G. Faeth. Breakup of Round Nonturbulent Liquid Jets in Gaseous Crossflow. *AIAA Journal* 42 (11): 2529-2540. 2004.
- [9] J. Belden, T. T. Truscott, S. Ravela, and A. H. Techet. Three-Dimensional Bubble Field Resolution Using Synthetic Aperture Imaging: Application to a Plunging Jet, *Exp. Fluids* in press. 2012.

# Chapter 4

## Application of LFI & SA

## Refocusing to Turbulent Sheet

## Breakup

### 4.1 Introduction

When a liquid volume is in the presence of a gas, it often first takes the form of a liquid sheet. A liquid sheet exiting a nozzle may develop disturbances that grow in amplitude. These oscillations eventually cause the sheet to break up first into ligaments and then droplets, which form the spray (see Figure 4-1, reproduced from [1]). The sheet thickness generally sets the order of magnitude of spray droplet sizes. Therefore, even though the sheet nozzle may be wide, a fine droplet spray may be formed as long as the sheet is thin in the other dimension [1]. In order to fully understand the atomization process that leads to spray formation, it is critical to grasp the physics of sheet instabilities. Although two-dimensional (2D) imaging of sheets can provide some information about the spray formation dynamics, they cannot fully resolve the flow features in this highly three-dimensional (3D) problem, which involves spray ligaments, droplets, and segments of the sheet often occluding each other. In this chapter,

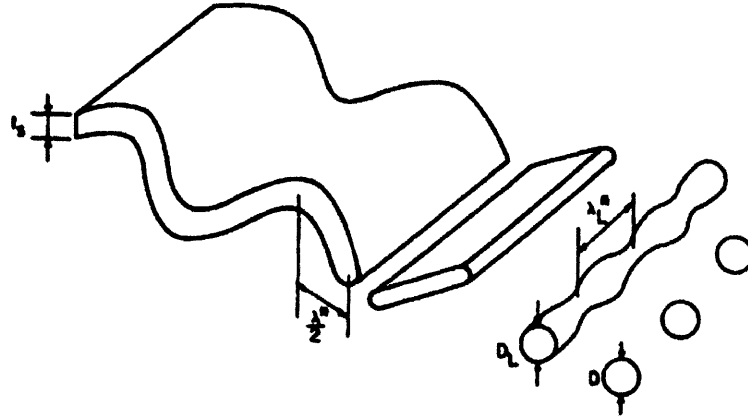


**Figure 4-1: Schematic of the evolution of a sheet into a jet and then droplets during atomization, reproduced from [1].**

3D imaging of the breakup of a turbulent liquid sheet emanating from a nozzle into air is discussed. Light field imaging (LFI) and synthetic aperture (SA) refocusing techniques were applied to resolve the resulting 3D spray fields. The ultimate goal is to characterize the size range, spatial distribution, and velocities of droplets formed by unsteady, turbulent sheet breakup, such as that formed by ship bow waves. This information will help develop models and validate numerical simulations of sprays.

## **4.2 Physics of Liquid Sheet Atomization in a Quiescent Gas**

Aerodynamic interactions between a liquid sheet and the surrounding gas create an instability in the sheet. Although surface tension contributes to the breakup of a cylindrical liquid jet (Rayleigh-Plateau instability), capillary forces actually help stabilize a planar liquid sheet [2]. A linear stability analysis of the shear instability of a high-velocity liquid sheet between two infinite non-moving fluids was performed by [3, 4, 5]. [2] and [6] provide a review of other more recent studies. The instability

that develops has both a varicose and sinuous mode, with the sinuous one having a larger growth rate. For a sheet of constant thickness, [7] achieved good agreement with experiments for the selected wavelength and associated growth rate of the sheet instability. [8] investigated a radially expanding sheet.

Although the initial sheet instability appears to be well understood, the connection between this instability and the primary breakup of the sheet is less clear [9]. There is speculation that the sheet breaks up in a series of lamellae parallel to the free rim and spaced by half the most unstable wavelength of the primary wavy pattern [4]. However, the reason for the lamellae separating from each other is not provided ([10, 11]), and this conjecture does not agree with the observation that the sheet breaks up in longitudinal ligaments, perpendicular to the free edge. A similar effect can be seen in Figure 4-2 (reproduced from [9]), which shows the breakup of a liquid sheet in air formed by the collision of two liquid jets.

[8] have suggested that a Rayleigh-Taylor-like instability [12, 13] that causes fingers perpendicular to the free rim periodically accelerated by the incoming waves is responsible for the initial sheet instability. The surface waves propagate at a velocity different than that of the sheet itself. In the reference frame of the liquid, a liquid particle moves up and down due to the waves that develop along the sheet, which is why this type of instability has been called a “wavy corridor” [9]. It turns out that the thickness of the sheet influences the severity of the instability. If the sheet thickness,  $h$ , is less than the capillary length, which is derived by balancing the liquid’s inertia force and the capillary restoring force and is defined as

$$l \sim \sqrt{\sigma/(\rho a_c)}, \quad (4.1)$$

where  $l$  is the capillary length,  $\sigma$  is the surface tension,  $\rho$  is the liquid density, and  $a_c$  is the centripetal acceleration, then the two gas-liquid sheet interfaces are close together and the Rayleigh-Taylor instability’s effect is reduced. As  $h/l \rightarrow 0$ , the growth rate

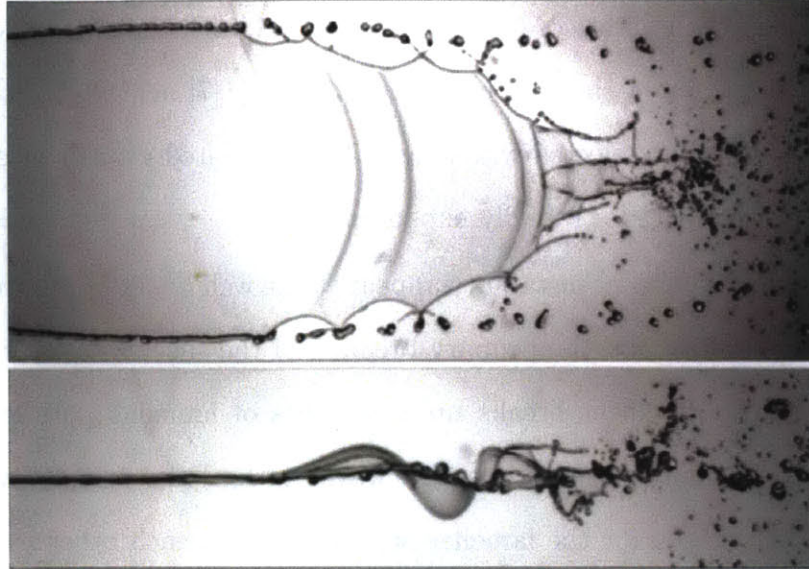


**Figure 4-2: Front view (top) and side view (bottom) of the destabilization of a liquid sheet moving in air initially at rest (reproduced from [9]).**

of the Rayleigh-Taylor instability also approaches zero. This type of instability has been found in other atomization situations that feature acceleration of the liquid/gas interface [14, 15]. It has sometimes even been shown [16] to be the primary cause of the emergence of digitations at the interface. These digitations eventually grow into ligaments, which finally break up into droplets [9]. Figure 4-3 presents an example of the digitations, ligaments, and droplets formed during the atomization of the turbulent liquid sheet at its edge from the present investigation. Ligaments of this type have also been observed in different atomization process in air-blasted sheets [17, 18]. Savart [19] showed this in drawings from sheets expanding radially from a jet. They have also appeared in simulations when a spanwise perturbation is initially added to the flow [20, 21].

Here the breakup of an unsteady, angled turbulent water sheet in (initially) quiescent air that first collides with a solid plate is considered. In addition to the Kelvin-Helmholtz and Rayleigh-Taylor type instabilities discussed above, another Rayleigh-Taylor instability may be involved because the trajectory of the sheet itself is curved.

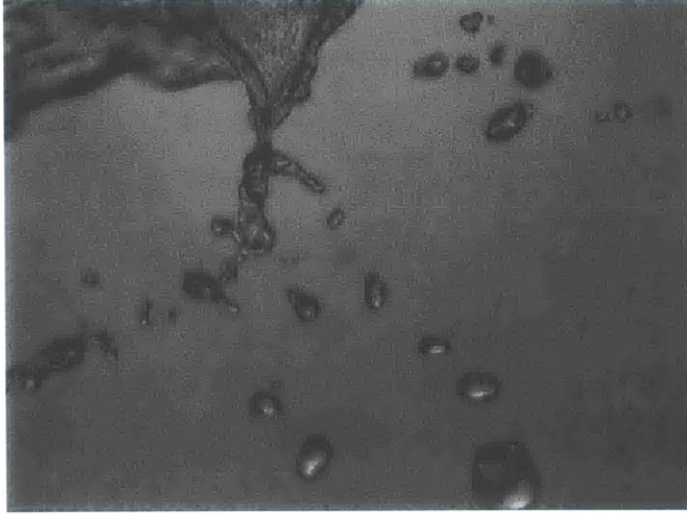


**Figure 4-3: Photograph of the atomization of a turbulent liquid sheet in air.**

(The other Rayleigh-Taylor instability was due to the transverse acceleration of the sheet surfaces due to the waves that develop along the sheet [9]. Since the sheet thickness is of the same order as the capillary length of water, 2.7 mm, this other Rayleigh-Taylor instability should play a role in the sheet atomization.). As in the case of a liquid jet in cross flow, the centripetal acceleration of the liquid-gas interface perpendicular to itself induces this second Rayleigh-Taylor instability. For a Rayleigh-Taylor instability, the most unstable mode has a wavelength of  $2\sqrt{3}\pi(\sigma/(\rho a_c))^{1/2}$  and a timescale of instability of  $(\frac{2}{3}/\sqrt{3})(\sigma/(\rho a_c^3))^{1/4}$  [22]. The centripetal acceleration in this case has a value of  $v^2/r_c$ , where  $v$  is the tangential sheet velocity and  $r_c$  is the curved sheet's radius of curvature.

Turbulence also complicates physics of the atomization of the liquid sheet in this case. This turbulence is due both to the large sheet width and high velocity (causing the Reynolds number to be high) as well as the initial collision of the sheet with the solid plate, which causes upstream vibrations that propagate along the moving sheet. The combination of all of these instabilities causes digitations to form, from which ligaments elongate and break off. More ligaments appear at the edges of the sheet,

where surface tension forces are greater due to the larger surface area of the sheet exposed to the air in these regions.

### 4.3 Experiments

The experimental apparatus consisted of an angled sheet of water issuing from a plenum into air that immediately collided with a Plexiglas sheet upon exiting the nozzle (see Figure 4-4). In order to cause this collision, the Plexiglas sheet was angled at  $30.7^\circ$  relative to the horizontal, while the nozzle was angled at  $30.8^\circ$ . Three water volume flow rates were generally utilized in these experiments: approximately 215, 245, and 265 gallons per minute (these correspond to speeds of approximately 7, 8, and 8.6 m/s respectively). The overall liquid sheet followed a parabolic path under the influence of gravity. 80/20  $\text{\textcircled{R}}$  aluminum rails were utilized to hold up the apparatus. In order to understand the spray ligament and droplet characteristics and distribution throughout the sheet, the camera array that was used to record videos of the flow was positioned at multiple locations (Figure 4-5). The horizontal spacing between any two columns of positions was three inches, and the vertical spacing was usually 1.5 inches, but varied in several of the experiments. Some images were recorded with the cameras in the array rotated  $30.8^\circ$  to be aligned with the liquid sheet, while for other experiments the cameras were level.

Videos were recorded using a planar camera array with ten cameras arranged in three rows. Figure 4-6 shows a photograph of the camera array and Figure 4-7 is a schematic of the relative positions and spacings of the cameras in the array. For positions 1-30, the cameras in the array were focused on the center of the sheet. In the remaining positions, the cameras were focused on the edge of the sheet closest to the array. The images were processed using light field imaging and synthetic aperture refocusing algorithms written in MATLAB.



The cameras used in these experiments are Flea 2 model FL2-08S2M/C from Point Grey Research, Inc. All ten cameras in the array were synced and simultaneously captured 1024 x 768 pixels, 8 bit, monochromatic images at 30 frames per second maximum. Although this frame rate was not high enough to achieve fine temporal resolution, it was effective for recording images that could be refocused and from which flow structures, such as droplets and ligaments, could be extracted and investigated. High-speed cameras were used by [23] with similar success but significant cost increase. Each Flea camera was equipped with a Nikon Nikkor 50 mm lens and F-to-C mount adapter. (In later experiments, monochrome Manta GigE cameras from AVT were utilized with 35 mm lenses to increase the field of view.)

The cameras were arranged in a planar array mounted on 80/20<sup>®</sup> aluminum rails, in various configurations. All cameras were oriented at angles such they could all record the same image volume simultaneously. The spray was back illuminated by a pulsed LED light bank (later two of these light banks were used for additional light), which could be synchronized with the camera frame rate; a common light diffuser, such as that used by professional photographers, was used to create uniform, diffuse lighting.

An auto-calibration method relying on a pinhole model was utilized to establish a mapping function between the image planes and world coordinates [24]. For all calibrations, a checkered grid (with either two or five square millimeter grid spacing) was randomly moved and recorded in different orientations throughout the focal volume for each set of experiments. Figure 4-8 shows a sample image of the calibration grid from all ten cameras in the array for a particular orientation of the grid. It was important to make sure that the calibration plate was in focus in every image by each camera in the array to ensure that the auto calibration and refocusing algorithm would succeed in reconstructing the volume.

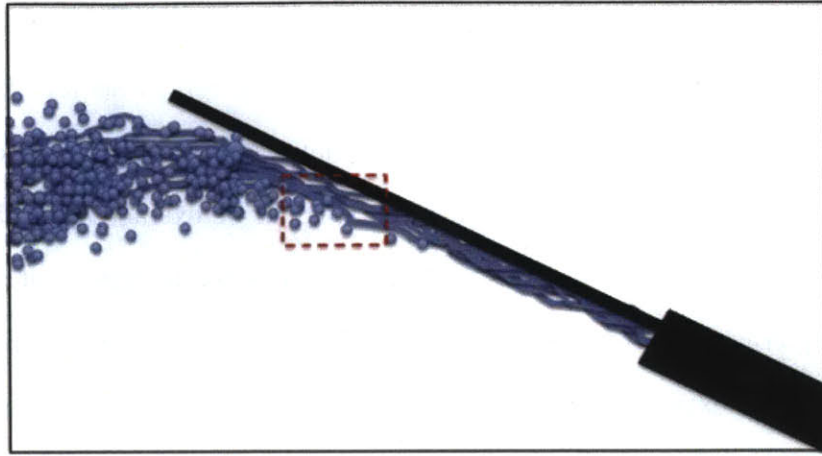


Figure 4-4: Turbulent sheet of water flowing along an inclined plate; imaging was performed in the region where breakup and separation from the plate begins.

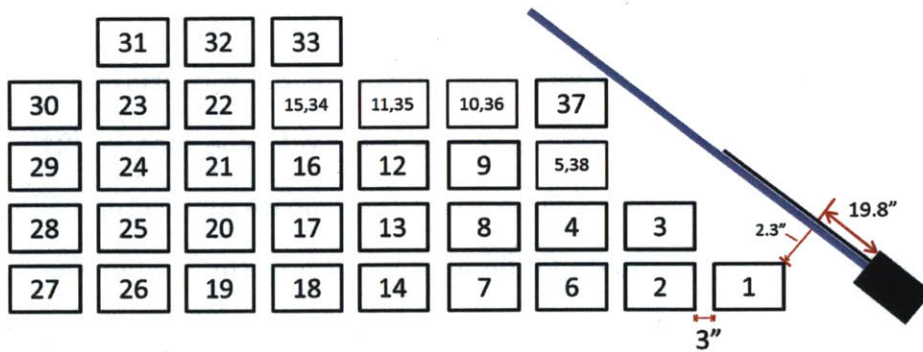


Figure 4-5: Turbulent sheet experimental setup showing relative locations of the camera array for each experiment.

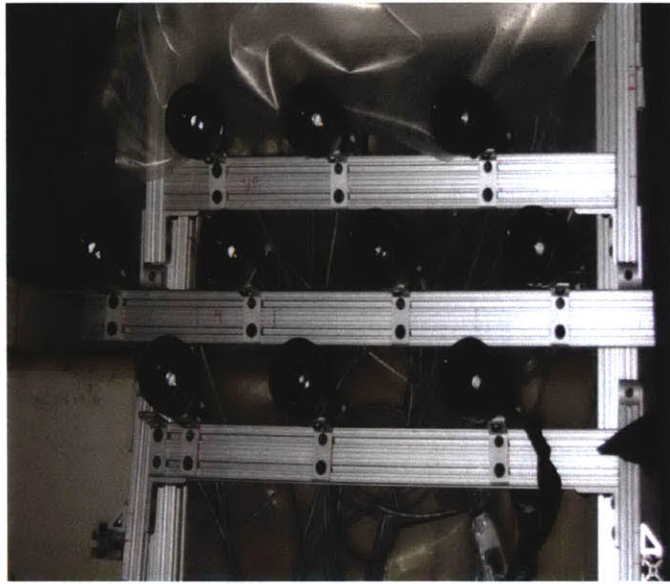


Figure 4-6: Ten camera array of Flea 2 model FL2-08S2M/C from Point Grey Research, Inc. CCD cameras, with 50mm Nikkor lenses, typical of those used for the experiments presented herein.

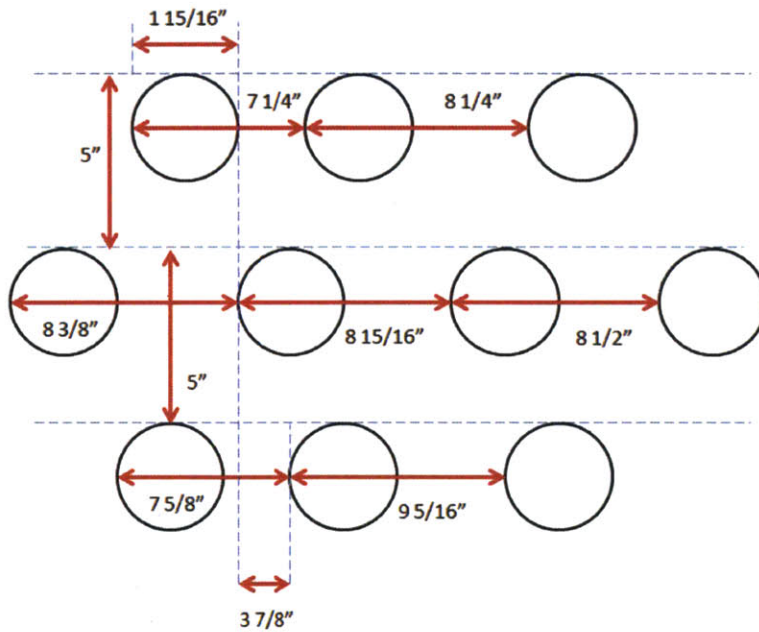


Figure 4-7: Schematic of relative positions of the ten cameras in the array.

## 4.4 Results and Discussion

Synthetic aperture imaging, which is a subset of light field imaging, was utilized to image the unsteady turbulent sheet described above in 3D. An example of this method is presented in Figures 4-8 and 4-9. A mapping is performed between the camera image planes and world coordinates using images of the calibration grid like those shown in Figure 4-8. Figure 4-9 shows the results of the synthetic aperture algorithm being applied to these calibration images. It is clear that the calibration grid is shown in sharp focus at the depth plane  $z = 0$  (shown in the middle in this figure), which is where it is actually located in physical space. Negative  $z$  values indicate image planes that are in front of the reference plane (closer to the camera array) at the center of the volume of interest, while positive values of  $z$  are behind the reference plane. At depths other than  $z = 0$  in this case ( $z = -5$  mm and  $z = 5$  mm, which are shown on the left and right, respectively, in Figure 4-9), the calibration grid is out of focus.

By applying this technique to raw data images of spray at a particular time instant from each of the cameras in the array like those presented in Figure 4-10, it is possible to move through the refocused volume of interest by projecting the individual images onto the desired number of focal planes (Figure 4-11). The notable features in these images are the ligaments and droplets of water emanating from the liquid sheet, which was located above the field of view of the cameras in these images (position 1). It is interesting to investigate the nature of the shape and size distribution of these structures, which are formed during the primary breakup phase of the sheet atomization. These ten individual camera images were processed using the multiplicative refocusing method with a multiplicative exponent of  $1/5$ . This means that each of the projected images from the individual cameras at the focal planes indicated in Figure 4-11 was first raised to a power of  $1/5$  and then multiplied together according to the following formula:

$$I_{SA_k} = \prod_{i=1}^N [(I_{FP_{ki}})^n], \quad (4.2)$$

where  $I_{SA_k}$  is the resulting image showing what is in focus at the focal plane  $k$ ,  $I_{FP_{ki}}$  denotes the image from camera  $i$  aligned on the  $k^{th}$  focal plane,  $n$  is the multiplicative exponent between zero and one, and  $N$  is the number of cameras, which is ten in this case. Multiplicative refocusing enhances the signal-to-noise ratio compared to additive refocusing, which involves averaging the projected images over the number of cameras in the array:

$$I_{SA_k} = \frac{1}{N} \sum_{i=1}^N I_{FP_{ki}}. \quad (4.3)$$

The result of Eq. 2 leads to a higher signal-to-noise ratio than Eq. 3 for well-calibrated images without letting any camera with an occluded view of an object prevent that object from being refocused because a small number raised to an exponent between zero and one is non-zero. It has been determined that  $n$  in the range  $\frac{1}{5} \leq n \leq \frac{1}{3}$  works best. Figure 4-11 presents refocused image planes at various depths throughout the image volume. Appendix A contains sets of raw and refocused images from experiments at each of the 38 positions shown in Figure 4-5.

Those structures that are not depicted in sharp focus, or that appear to be ghosting, are actually located at a different depth in the volume and are not in focus on that  $z$ -plane. The identification of the plane(s) of focus of particular features allows their positions in the volume to be determined. Figure A-41 presents a set of raw images with the array at position 21, focusing on the center of the sheet. Since the features shown in these images are relatively large compared to the field of view, ghosting is more evident in the refocused images shown in Figure A-42. However, the in-focus features are still delineated. Ultimately a larger overall field of view and depth of field, achieved with different lenses, would yield more data for validation of

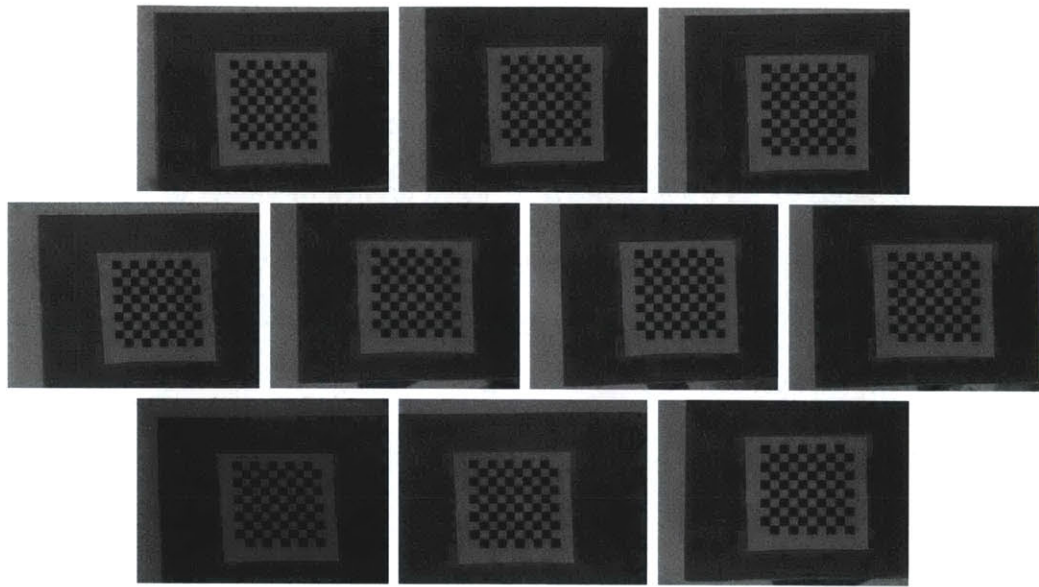


Figure 4-8: Sample calibration grid images for a particular grid orientation from each of the ten cameras in the array.

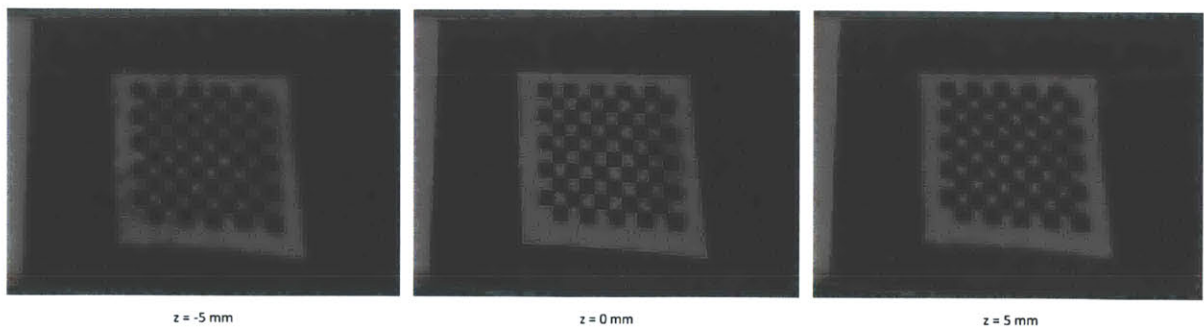


Figure 4-9: Sample refocused planes corresponding to the raw calibration grid images shown in Figure 4-8. The grid is in focus at depth  $z = 0$  (shown at middle), where it is actually located in physical space, but is out of focus at other depths (shown at left and right).

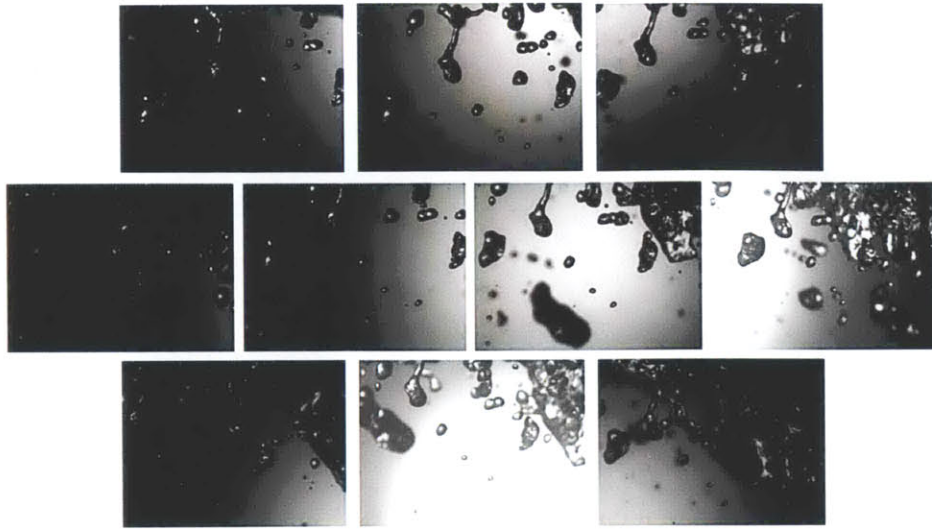


Figure 4-10: Raw array images at position 1, with the cameras focused on the sheet's center. Here the flow rate is 278 gallons per minute.

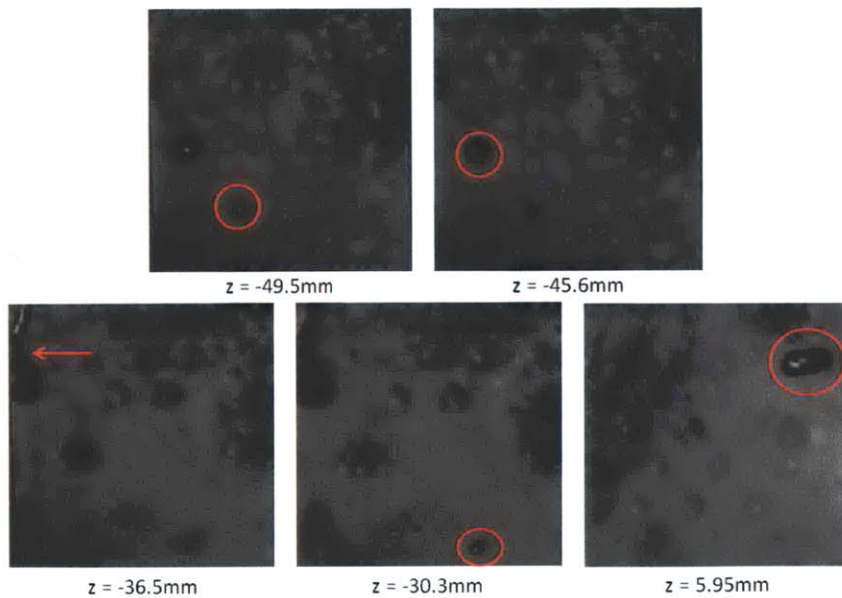


Figure 4-11: Sample refocused planes with indicated in-focus features corresponding to the raw images in Figure 4-10.

CFD studies and development of theoretical predictions. Challenges with the Flea cameras arose mainly due to issues with the firewire interface and individual camera gains, which tended to challenge the reconstruction when one camera had brighter overall images than another. Gains were typically adjusted to provide a similarly light/dark background for all ten cameras.

For this investigation, the overall field of view was smaller than desired due to the magnification factor of the CCD camera (35mm mount camera lenses were used with a Nikon to C-mount adapter, instead of C-mount). However, here it is shown that it is possible to determine the location of the droplets and the incline of the ligaments in three dimensions. In addition it is possible to place the location of the droplets relative to the turbulent sheet with good position calibration a priori. Figures A-67 and A-68 present raw and refocused images, respectively, from the array located at position 34 with the cameras focused on the near edge of the sheet. Due to the relatively larger surface tension forces at the sheet's edge, more in-focus ligaments and droplets can generally be observed in this region since it is easier for the sheet to break up there. Relatively large ligaments like the one shown in these figures are therefore more likely to be observed in this part of the sheet.

Figures A-1 and A-2, which correspond to position 1 with the cameras focused on the center of the sheet, highlight a key advantage of the synthetic aperture refocusing technique. At the plane  $z = 163$  mm (the right image in Figure A-2), it is possible to see a droplet and ligament that would otherwise have been occluded by the bulk of the sheet in most of the images from the cameras in the array. Therefore, it is possible to see through partial occlusions using this imaging method in optically dense flows such as this one. Other imaging techniques would not be able to achieve this.



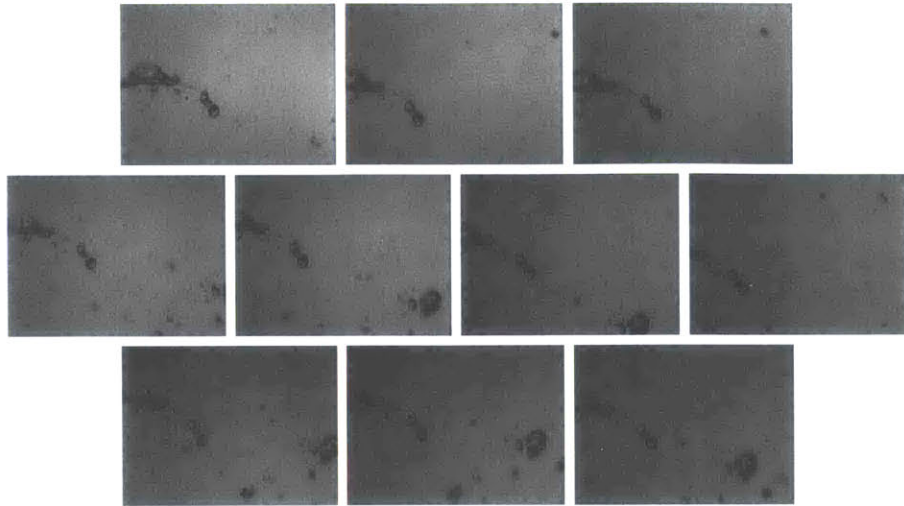


Figure 4-12: Raw array images at position 21, with the cameras focused on the sheet's center and rotated 30.8° clockwise from the horizontal to be aligned with the sheet. The liquid flow rate was 268 gallons per minute.

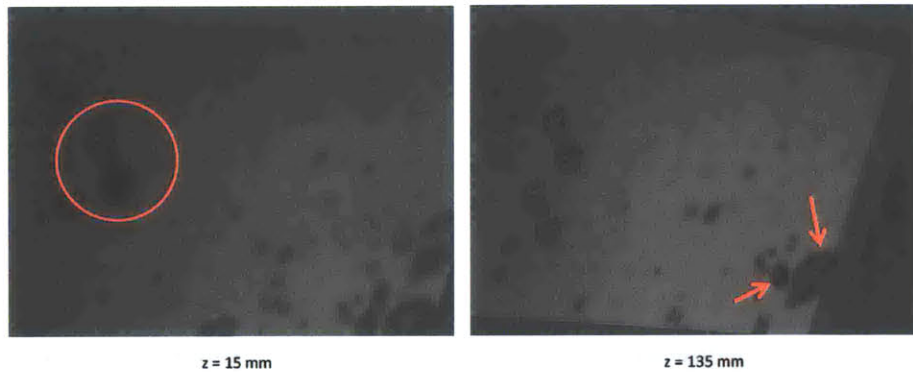


Figure 4-13: Two sample refocused planes with indicated in-focus features corresponding to the raw images in Figure A-41. Multiplicative refocusing was used with an exponent of 1/3.

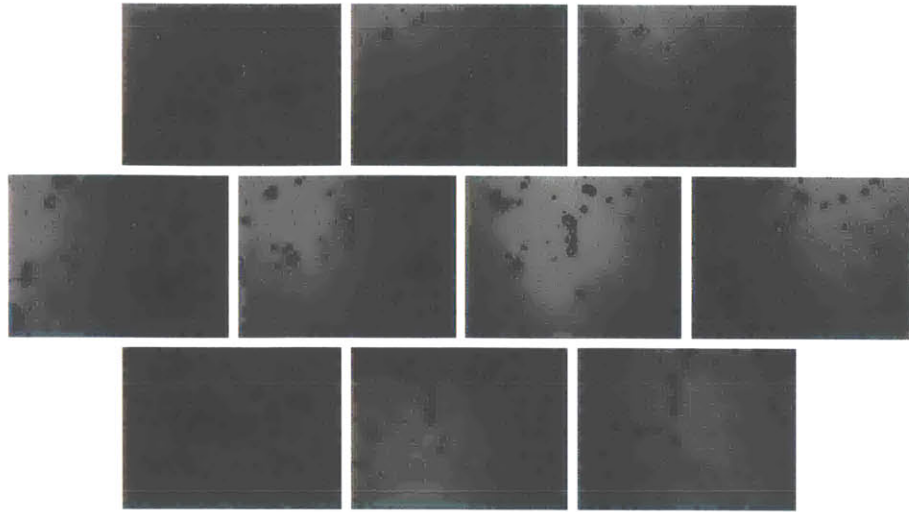


Figure 4-14: Raw array images at position 34, with the cameras focused on the near sheet edge and rotated 30.8° clockwise from the horizontal to be aligned with the sheet. The liquid flow rate was 270 gallons per minute

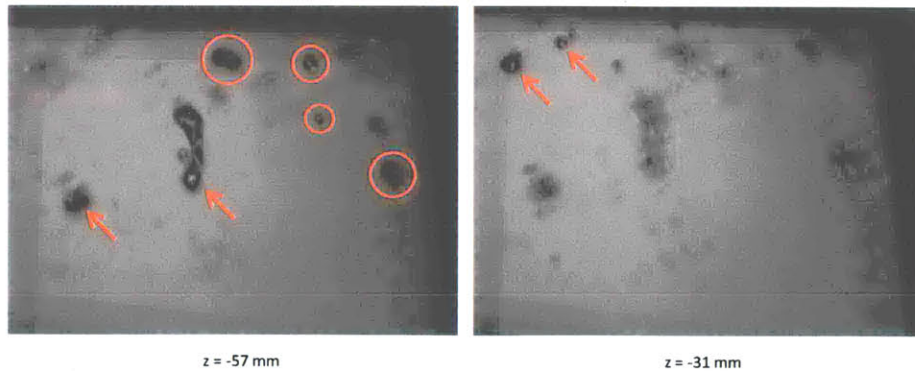


Figure 4-15: Two sample refocused planes with indicated in-focus features corresponding to the raw images in Figure A-67. Multiplicative refocusing was used with an exponent of 1/4.

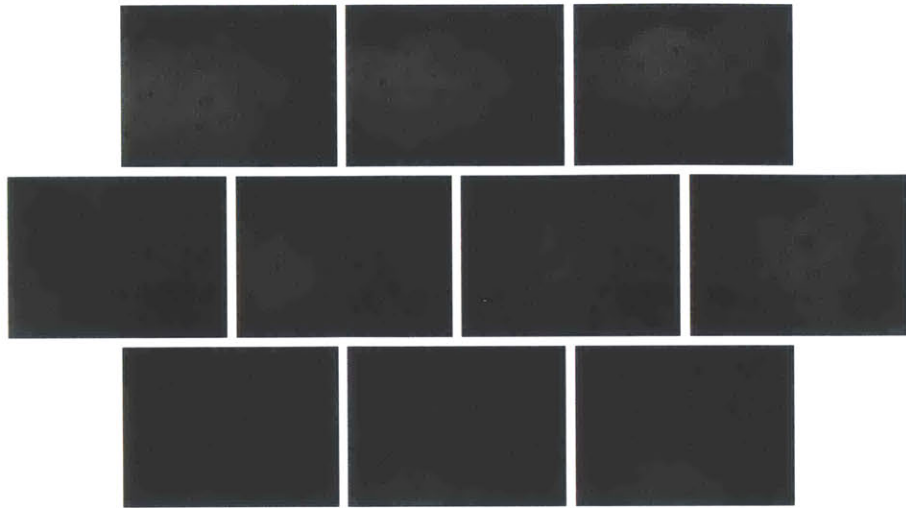


Figure 4-16: Raw array images at position 1, with the cameras focused on the near sheet edge and rotated 30.8° clockwise from the horizontal to be aligned with the sheet. The liquid flow rate was 270 gallons per minute

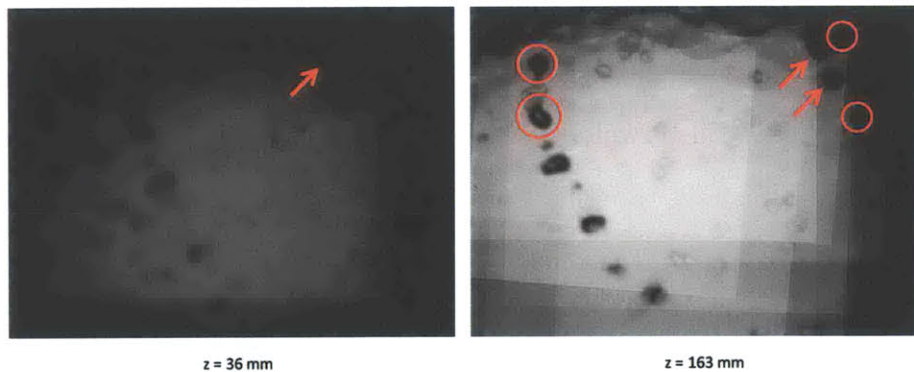


Figure 4-17: Two sample refocused planes with indicated in-focus features corresponding to the raw images in Figure A-1. Multiplicative refocusing was used with an exponent of 1/4.

## 4.5 Conclusions

Turbulent, unsteady liquid sheet atomization in air has been investigated experimentally using the emerging 3D imaging technique of synthetic aperture refocusing, which is a subset of light field imaging. It is shown that it is possible to determine the location of the ligaments and droplets emerging from the sheet during atomization in three dimensions. In addition, it is possible to place the location of the droplets relative to the turbulent sheet with good calibration a priori. Using these data, future work will involve building full models of the flow field by extracting the exact shapes of flow features in 3D.

### Acknowledgments

This work was funded by the Naval Engineering Education Center and the Office of Naval Research (Grant no. N00014-09-1-1167, Dr. Steven Russell). The experiments described in this chapter were performed at the Naval Surface Warfare Center Carderock Division (NSWCCD) in W. Bethesda, MD, USA in collaboration with Drs. Thomas Fu and Erin Hackett. I would also like to thank the following people for helping with the experiments: Leah Mendelson, Juliana Wu, Daniel Kubaczyk, and Thomas Milnes from MIT as well as Ashley Kowalski, Sarah Richer, Barry Abramson, and the rest of the members of the Carderock team. Leah Mendelson, Juliana Wu, and Abhishek Bajpayee (MIT) are also acknowledged for their help in processing the data from the experiments.

# Bibliography

- [1] L. Bayvel and Z. Orzechowski. *Liquid Atomization*. Washington, DC: Taylor & Francis. 1993.
- [2] N. Ashgriz. *Handbook of Atomization and Sprays: Theory and Applications*. New York, NY: Springer. 2011.
- [3] H. B. Squire. Investigation of the stability of a moving liquid film. *Brit. J. Appl. Phys.* 4: 167–169. 1953.
- [4] J. L. York, H. E. Stubbs, and M. R. Tek. The mechanism of disintegration of liquid sheets. *Trans. ASME*, 1279–1286. 1953.
- [5] W. W. Hagerty and J. F. Shea. A study of the stability of plane fluid sheets. *J. Appl. Mech.* 22: 509–514. 1955.
- [6] S. P. Lin. *Breakup of Liquid Sheets and Jets*. Cambridge University Press. 2003.
- [7] H. R. Asare, R. K. Takahashi, and M. A. Hoffman. Liquid sheet jet experiments: comparison with linear theory. *Trans. ASME: J. Fluids Engng* 103: 395–604. 1981.
- [8] E. Villermaux and C. Clanet. Life of a flapping liquid sheet. *J. Fluid Mech.* 462: 341–363. 2002.
- [9] N. Bremond, C. Clanet, and E. Villermaux. Atomization of undulating liquid sheets. *J. Fluid Mech.* 585: 421–456. 2007.

- [10] R. P. Fraser, P. Eisenklam, N. Dombrowski, and D. Hasson. Drop formation from rapidly moving liquid sheet. *AIChE J.* 8: 672–680. 1962.
- [11] N. Dombrowski and W. R. Johns. The aerodynamics instability and disintegration of viscous liquid sheets. *Chem. Engng Sci.* 18: 203–214. 1963.
- [12] Lord Rayleigh. Investigation of the character of the equilibrium of an incompressible heavy fluid of variable density. *Proc. R. Soc. Lond.* 14: 170–177. 1883.
- [13] G. I. Taylor. The instability of liquid surfaces when accelerated in a direction perpendicular to their plane.i. *Proc. R. Soc. Lond. A* 201: 192–196. 1950.
- [14] P. Einsenklam. On ligament formation from spinning disks and cups. *Chem. Engng Sci.* 19: 693–694. 1964.
- [15] A. J. James, B. Vukasinovic, M. K. Smith, and A. Glezer. Vibration-induced drop atomization and bursting. *J. Fluid Mech.* 476: 1–28. 2003.
- [16] P. Marmottant and E. Villermaux. On spray formation. *J. Fluid Mech.* 498: 73–112. 2004b.
- [17] A. Mansour and N. Chigier. Disintegration of liquid sheets. *Phys. Fluids A* 2: 706–719. 1990.
- [18] J. Park, K. Y. Huh, X. Li, and M. Renksizbulut. Experimental investigation on cellular breakup of a planar liquid sheet from an air-blast nozzle. *Phys. Fluids* 16: 625–632. 2004.
- [19] F. Savart. M´emoire sur le choc d’une veine liquide lanc´ee sur un plan circulaire. *Ann. de chim.* 54: 56–87. 1833c.
- [20] A. Lozano, A. Garcia-Olivares, and C. Dopazo. The instability growth leading to a liquid sheet break up. *Phys. Fluids* 10: 2188–2197. 1998.
- [21] I. Kim and W. A. Sirignano. Three-dimensional wave distortion and disintegration of thin planar liquid sheets. *J. Fluid Mech.* 410: 147–183. 2000.

- [22] S. Chandrasekhar. Hydrodynamic and Hydromagnetic Stability. Oxford: Oxford Univ. Press. 1961.
- [23] J. Belden, T. T. Truscott, S. Ravela, and A. H. Techet. Three-Dimensional Bubble Field Resolution Using Synthetic Aperture Imaging: Application to a Plunging Jet, *Exp. Fluids* in press. 2012.
- [24] J. Belden, T. T. Truscott, S. Ravela, and A. H. Techet. Three-dimensional synthetic aperture imaging and resolution of multi-phase flows. *Proc ASME-JSME-KSME Joint Fluids Engineering Conf Hamamatsu, Shizuoka, Japan*. 2011.





# Chapter 5

## Summary and Conclusions

This thesis presented an analysis of various multiphase spray flows using traditional high-speed imaging as well as the emerging technique of synthetic aperture (SA) refocusing, a subset of light field imaging (LFI) [1]. The SA codes were also updated and simulations were produced to further verify and improve upon the method. The flows investigated were a liquid jet in a cross flow of air and the atomization of an unsteady turbulent liquid sheet in air at an incline. For the liquid jet in cross flow, a new type of instability was discovered experimentally involving the presence of multiple bags, or partial bubbles, at the same streamwise position along the jet. The dynamics of bag expansion and upstream column wavelengths was investigated experimentally and theoretically and good agreement was found between the two approaches. Other flow features, such as upstream ligament extension properties, were measured and analyzed as well.

In addition to the high-speed imaging of liquid jets in gaseous cross flow, synthetic aperture imaging was used to study this flow. For this and the other flows mentioned above, it was demonstrated that flow features could successfully be resolved and located in three-dimensional space. Next steps will involve the development of algorithms to further extend the post-processing capabilities of SA data. The goal is to extract more quantitative data from refocused volumes, such as exact spray droplet

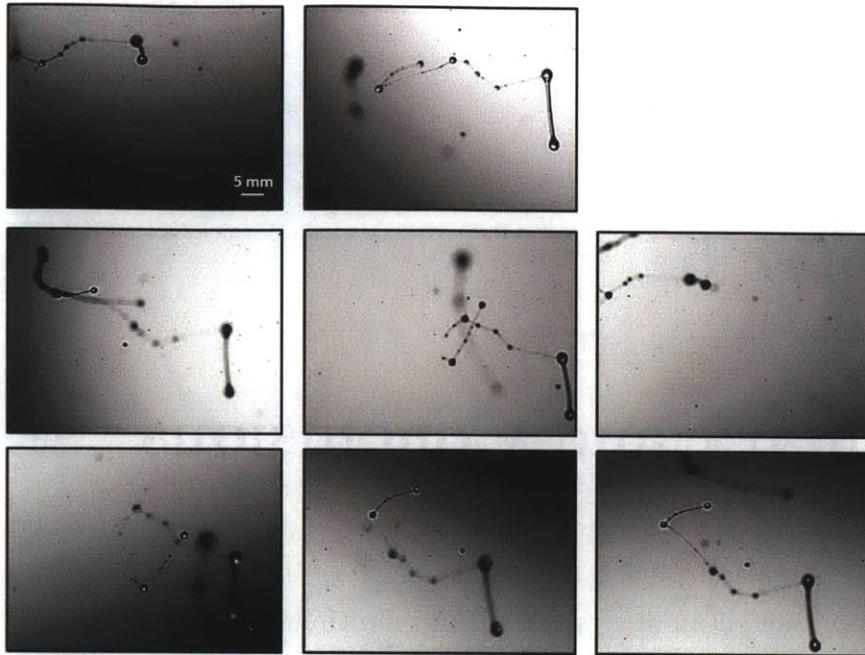


**Figure 5-1: Raw camera array images of ligaments and droplets in the spray resulting from a sneeze.**

and ligament shapes, sizes, velocities, etc. It is also desired to be able to produce complete three-dimensional computer models from the refocused image data. This will facilitate the comparison of experimental and simulation data, especially for complicated multiphase spray flows.

Another important application of the study of sprays is related to coughing and sneezing, which can both lead to airborne disease transmission [2]. Many sprays relating to medical applications such as this can benefit from the implementation of synthetic aperture imaging techniques. In order to further demonstrate the capabilities of the method and to provide an overview of future work, preliminary results from a sneezing experiment are presented. (The liquid in this multiphase spray flow is actually non-Newtonian, which further complicates the analysis because it requires considerations of viscoelasticity.) In this experiment, the researcher sneezes into the field of view and the resulting droplets and ligaments are recorded by the cameras

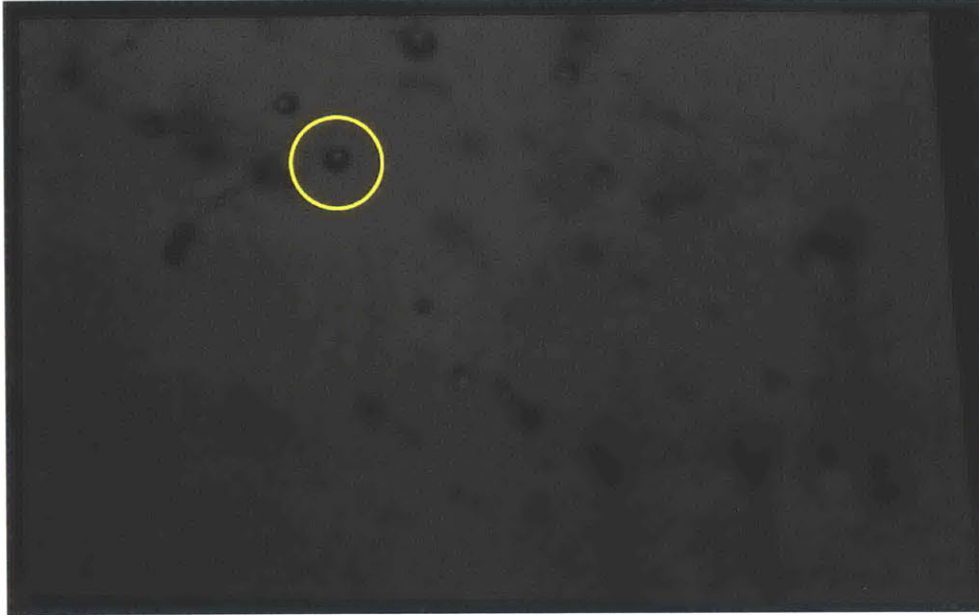


**Figure 5-2: Sample refocused image at plane  $z = 24$  mm. The in-focus node that is located at this plane is circled.**

in the array. Eight cameras were used to record the sample raw images presented in Figure 5-1. A sample refocused image is shown in Figure 5-2. The node of the one of the ligaments (circled) is in sharp focus, while other features are blurred, indicating that the node is actually located at that depth plane ( $z = 24$  mm), while the other features are located at different depths. Utilizing the synthetic aperture technique to study these kinds of flows could lead to exciting new discoveries of the dynamics of disease transmission through the air. Many other fields and applications would also stand to benefit from the application of this method because of the great insight that it can provide into optically dense multiphase flow structures and dynamics.

## **Acknowledgments**

The work on the sneezing project was performed in collaboration with Dr. Lydia Bourouiba and Professors Alexandra H. Techet and John W. M. Bush at MIT.

# Bibliography

- [1] J. Belden, T. T. Truscott, M. Axiak, and A. H. Techet. Three-dimensional synthetic aperture particle image velocimetry. *Meas Sci Technol* 21:1-21. 2010.
- [2] J. K. Gupta, C.-H. Lin, and Q. Chen. Flow dynamics and characterization of a cough. *Indoor Air*, 19(6):517-525. 2009.



# Appendix A

## Additional Turbulent Sheet

### Breakup SA Refocusing Data

This appendix presents sample refocused synthetic aperture (SA) refocusing image volume depth slices from all 38 positions underneath the turbulent sheet shown schematically in Chapter 4, Figure 4.5 along with the raw images that were refocused in each particular experiment. Sheet nozzle exit volume flow rates and multiplicative refocusing exponents (see Eq. 4.2) used to process the data are listed for each experiment.

#### A.1 SA Refocusing Data

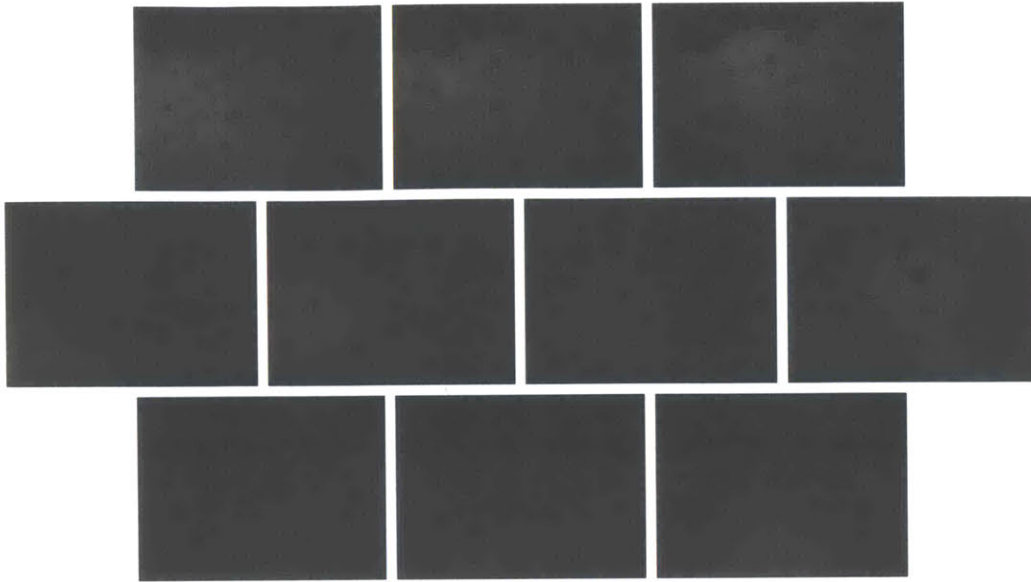


Figure A-1: Raw array images at position 1, with the cameras focused on the sheet's center and rotated  $30.8^\circ$  clockwise from the horizontal to be aligned with the sheet. The liquid flow rate was 270 gallons per minute.

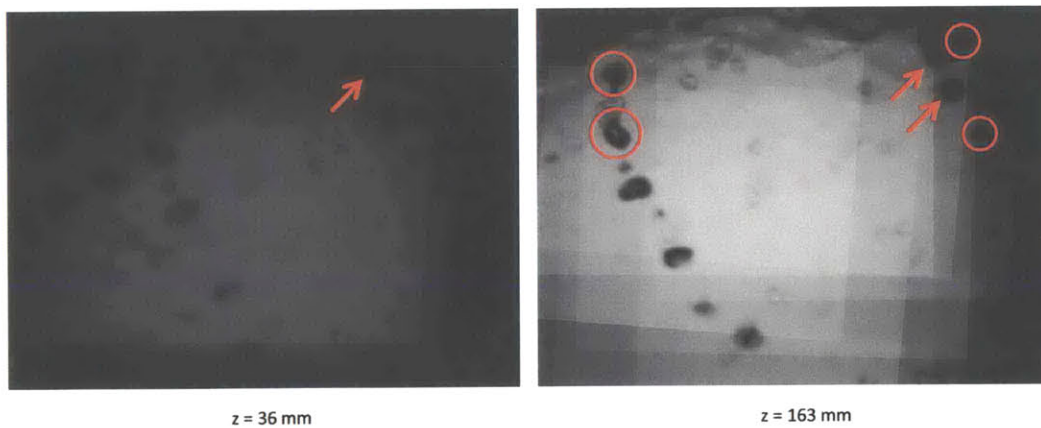


Figure A-2: Sample refocused planes with indicated in-focus features corresponding to the raw images in Figure A-1. Multiplicative refocusing was used with an exponent of  $1/4$ .



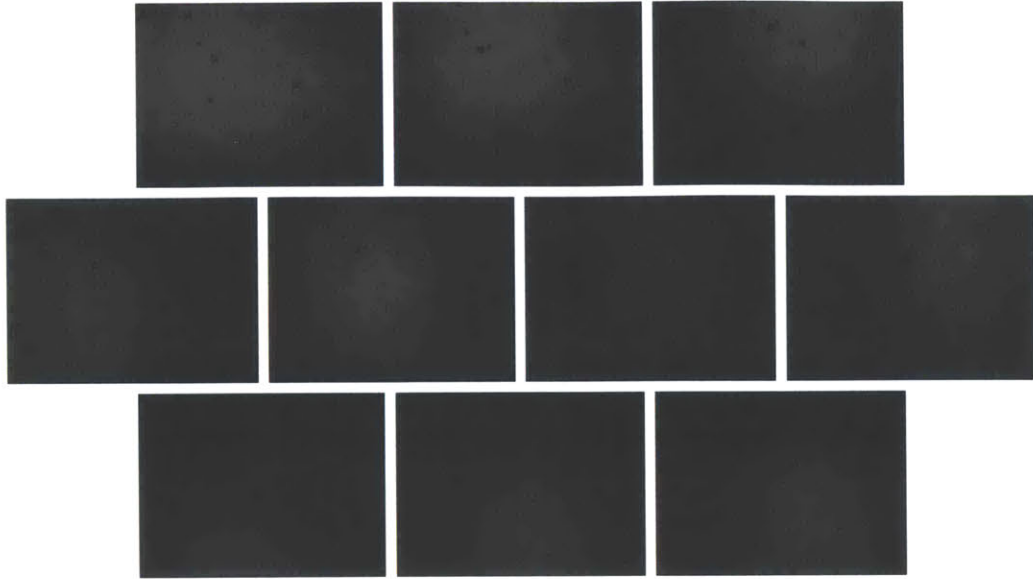


Figure A-3: Raw array images at position 2, with the cameras focused on the sheet's center and rotated 30.8° clockwise from the horizontal to be aligned with the sheet. The liquid flow rate was 269 gallons per minute.

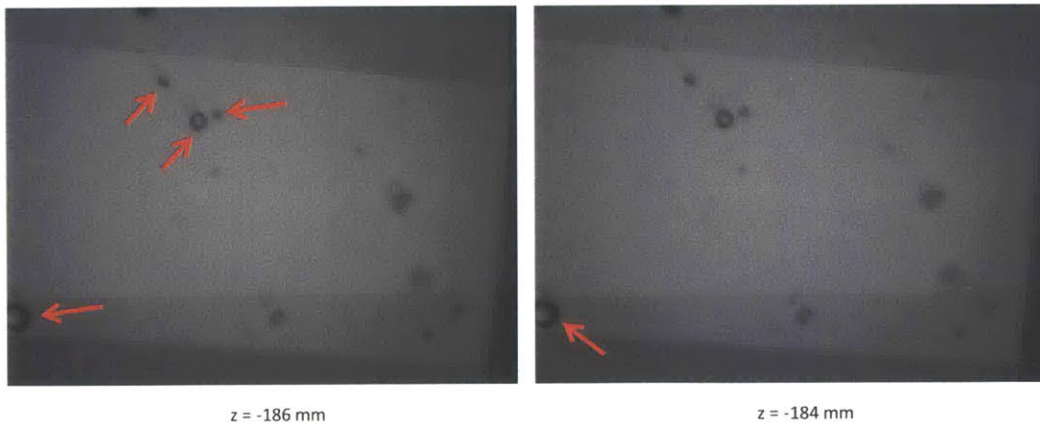


Figure A-4: Sample refocused planes with indicated in-focus features corresponding to the raw images in Figure A-3. Multiplicative refocusing was used with an exponent of 1/4.

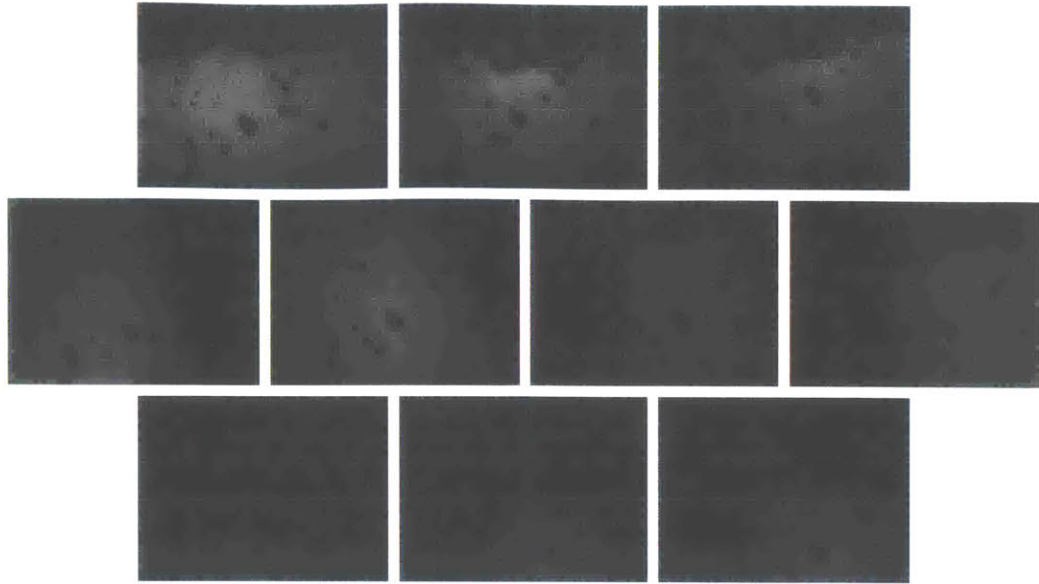


Figure A-5: Raw array images at position 3, with the cameras focused on the sheet's center and rotated 30.8° clockwise from the horizontal to be aligned with the sheet. The liquid flow rate was 268 gallons per minute.

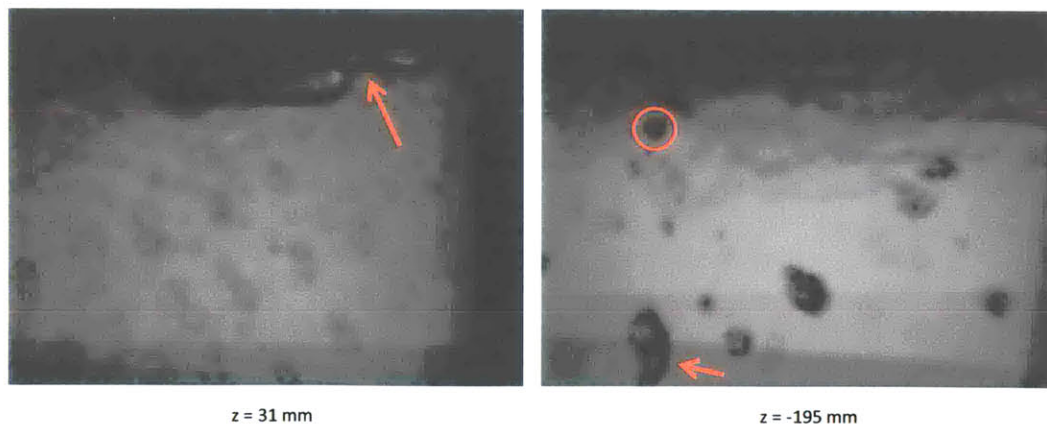


Figure A-6: Sample refocused planes with indicated in-focus features corresponding to the raw images in Figure A-5. Multiplicative refocusing was used with an exponent of 1/4.

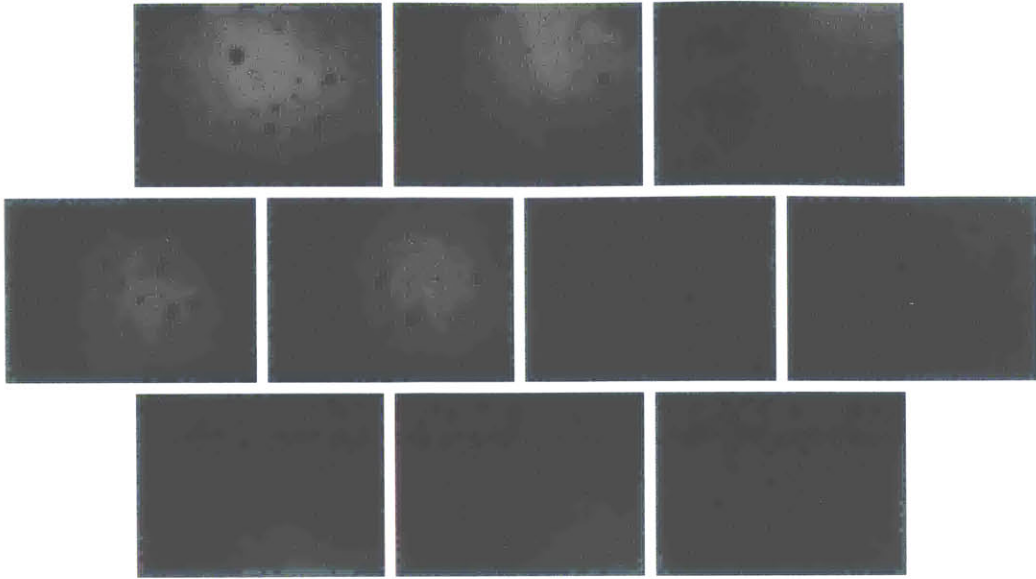


Figure A-7: Raw array images at position 4, with the cameras focused on the sheet's center and rotated  $30.8^\circ$  clockwise from the horizontal to be aligned with the sheet. The liquid flow rate was 267 gallons per minute.

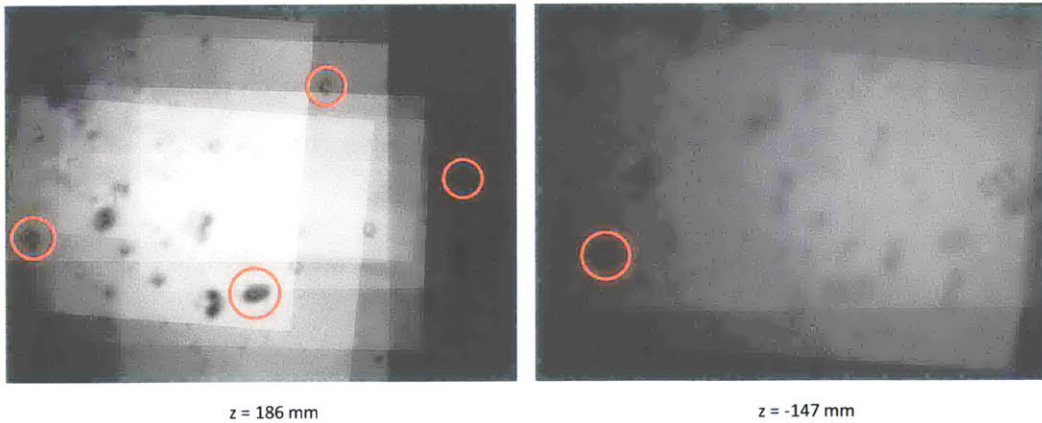


Figure A-8: Sample refocused planes with indicated in-focus features corresponding to the raw images in Figure A-7. Multiplicative refocusing was used with an exponent of  $1/4$ .

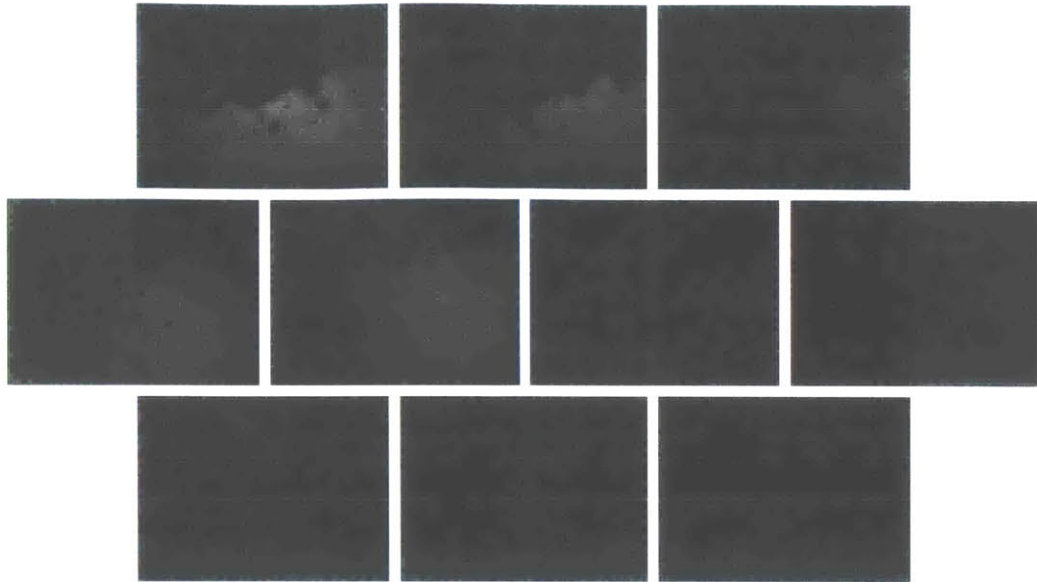


Figure A-9: Raw array images at position 5, with the cameras focused on the sheet's center and rotated  $30.8^\circ$  clockwise from the horizontal to be aligned with the sheet. The liquid flow rate was 268 gallons per minute.

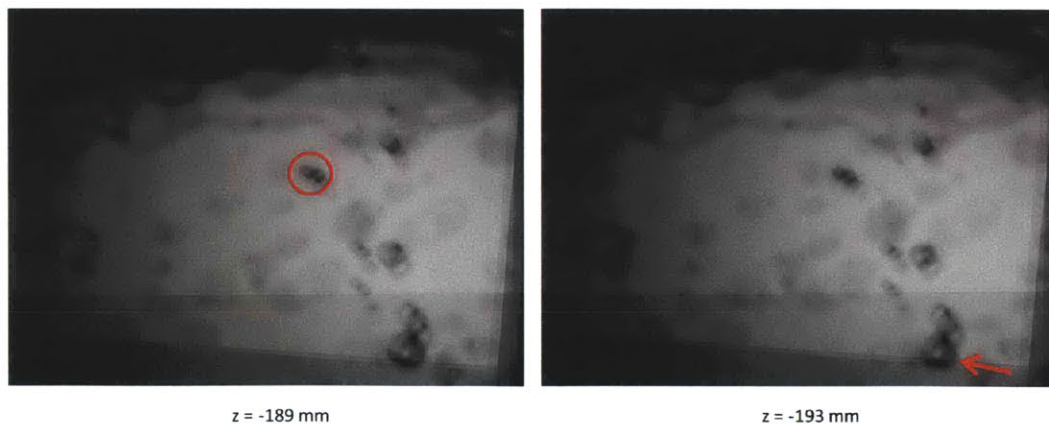


Figure A-10: Sample refocused planes with indicated in-focus features corresponding to the raw images in Figure A-9. Multiplicative refocusing was used with an exponent of  $1/4$ .

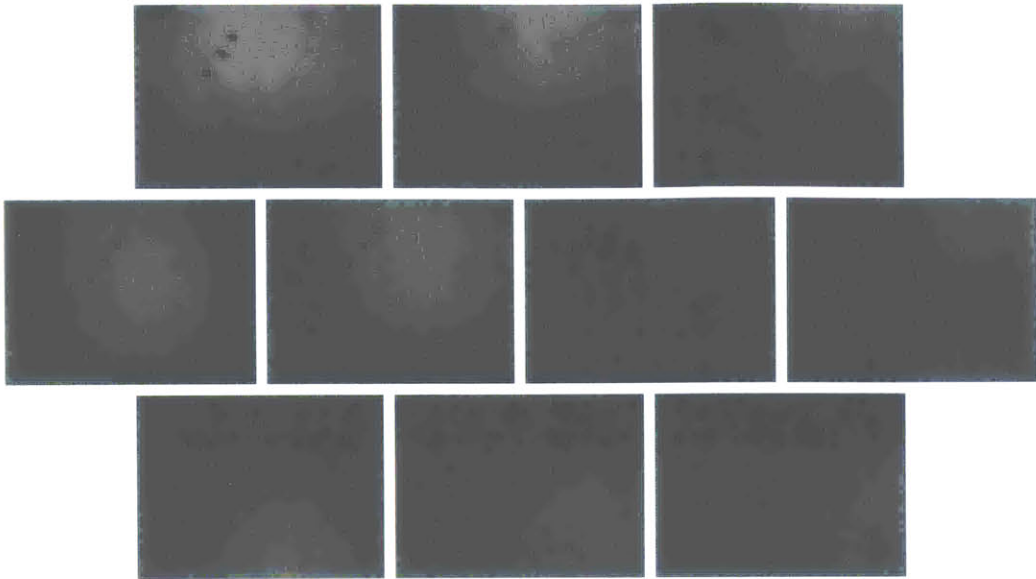


Figure A-11: Raw array images at position 6, with the cameras focused on the sheet's center and rotated 30.8° clockwise from the horizontal to be aligned with the sheet. The liquid flow rate was 267 gallons per minute.

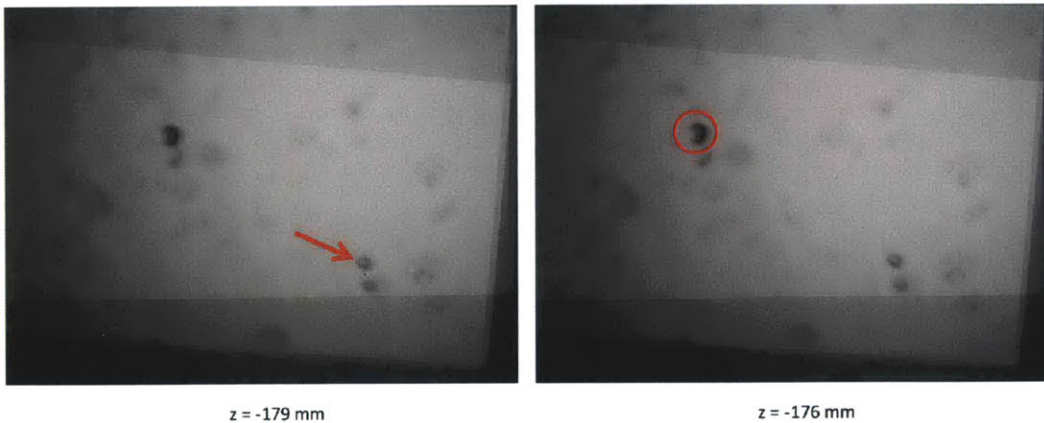


Figure A-12: Sample refocused planes with indicated in-focus features corresponding to the raw images in Figure A-11. Multiplicative refocusing was used with an exponent of 1/4.



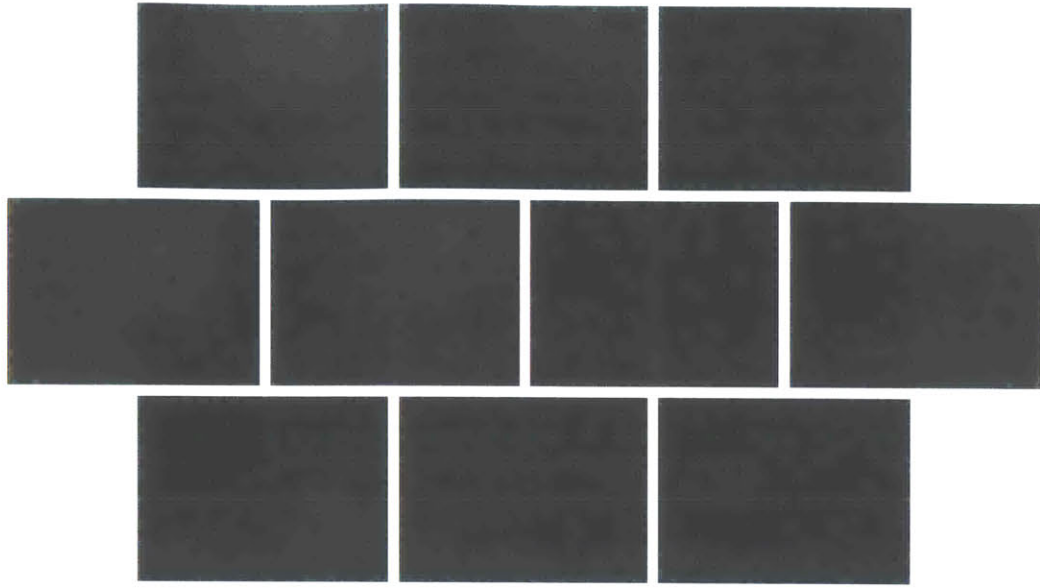


Figure A-13: Raw array images at position 7, with the cameras focused on the sheet's center and rotated 30.8° clockwise from the horizontal to be aligned with the sheet. The liquid flow rate was 268 gallons per minute.

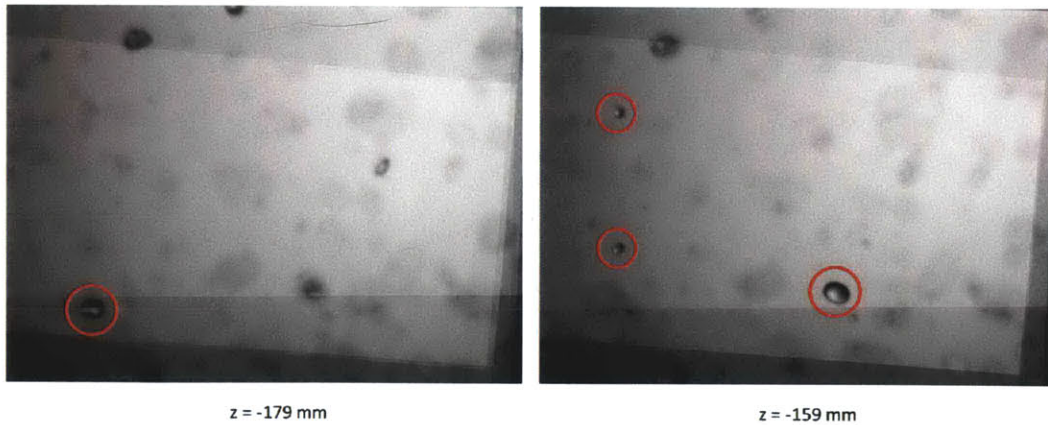


Figure A-14: Sample refocused planes with indicated in-focus features corresponding to the raw images in Figure A-13. Multiplicative refocusing was used with an exponent of 1/4.

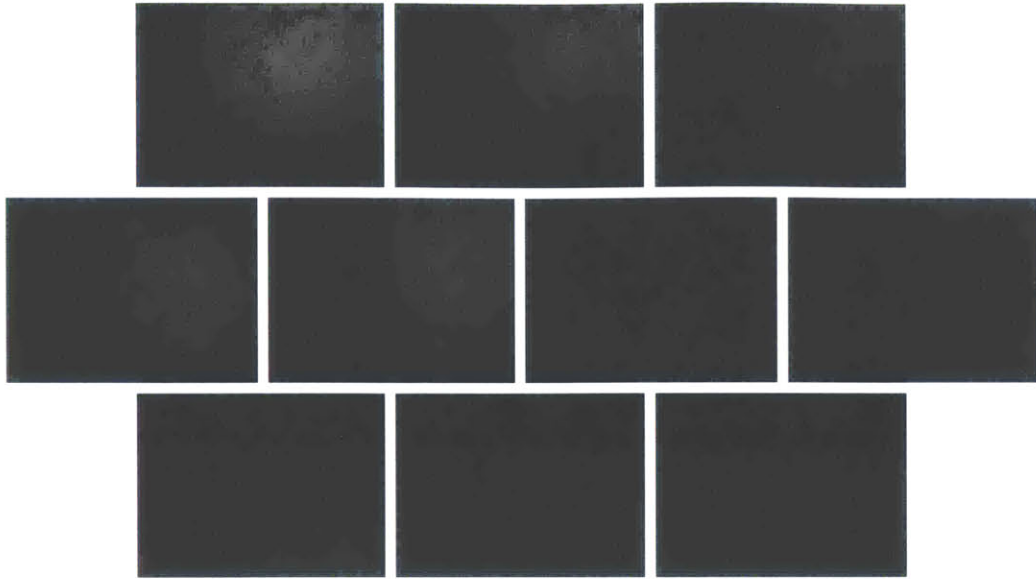


Figure A-15: Raw array images at position 8, with the cameras focused on the sheet's center and rotated 30.8° clockwise from the horizontal to be aligned with the sheet. The liquid flow rate was 269 gallons per minute.

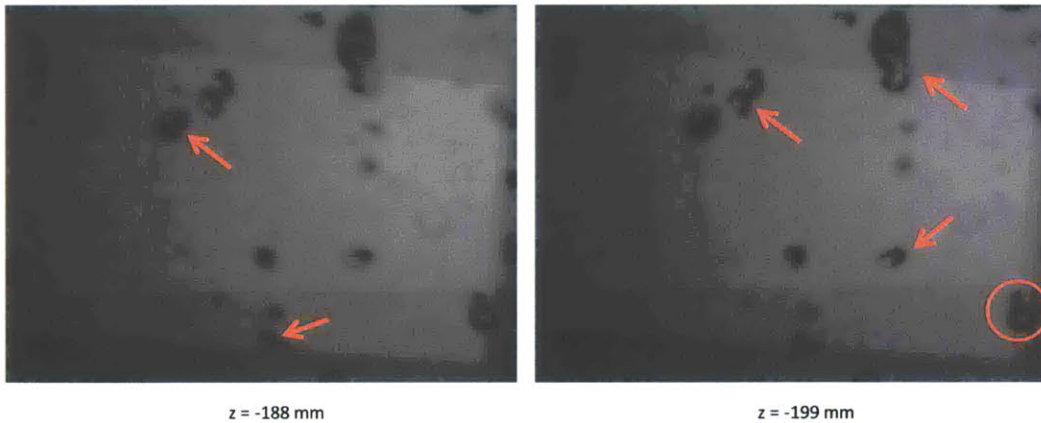


Figure A-16: Sample refocused planes with indicated in-focus features corresponding to the raw images in Figure A-15. Multiplicative refocusing was used with an exponent of 1/4.

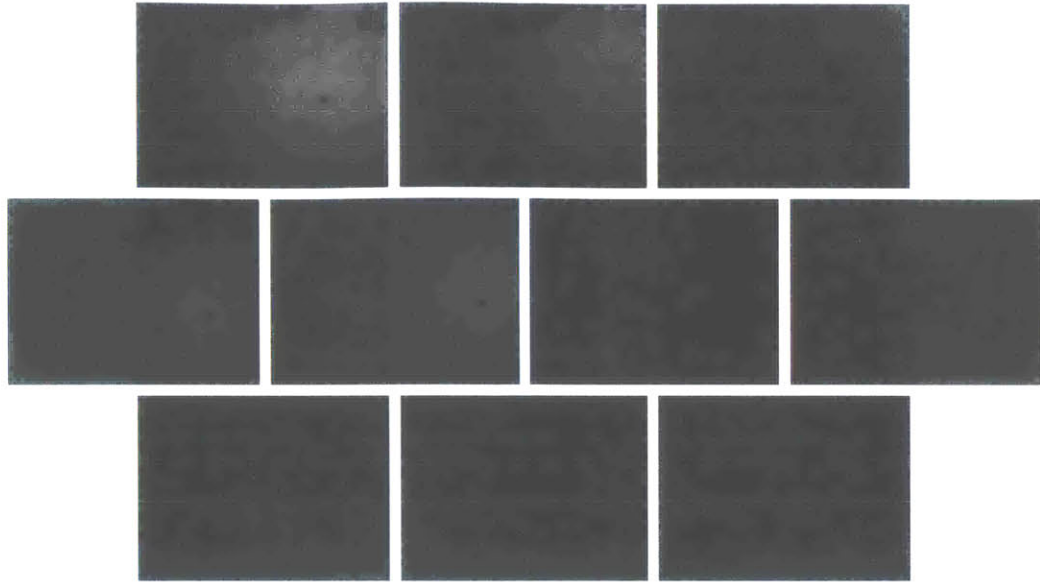


Figure A-17: Raw array images at position 9, with the cameras focused on the sheet's center and rotated  $30.8^\circ$  clockwise from the horizontal to be aligned with the sheet. The liquid flow rate was 268 gallons per minute.

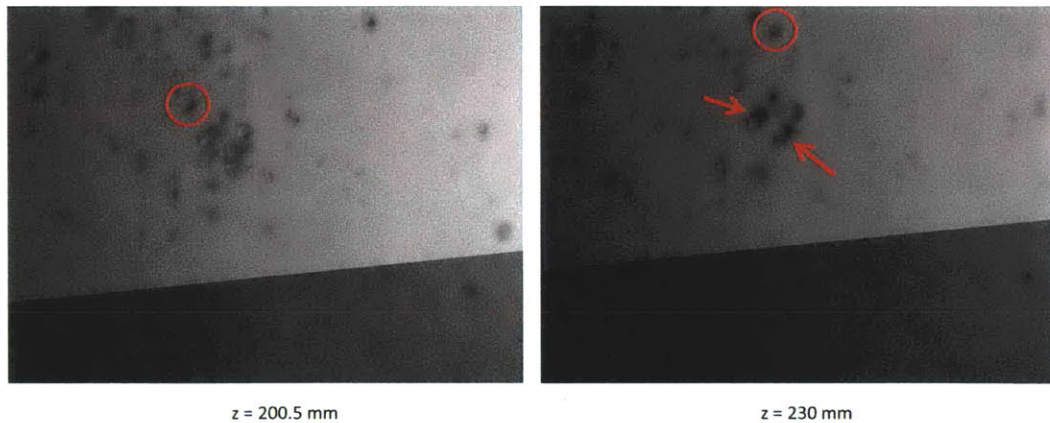


Figure A-18: Sample refocused planes with indicated in-focus features corresponding to the raw images in Figure A-17. Multiplicative refocusing was used with an exponent of  $1/4$ .



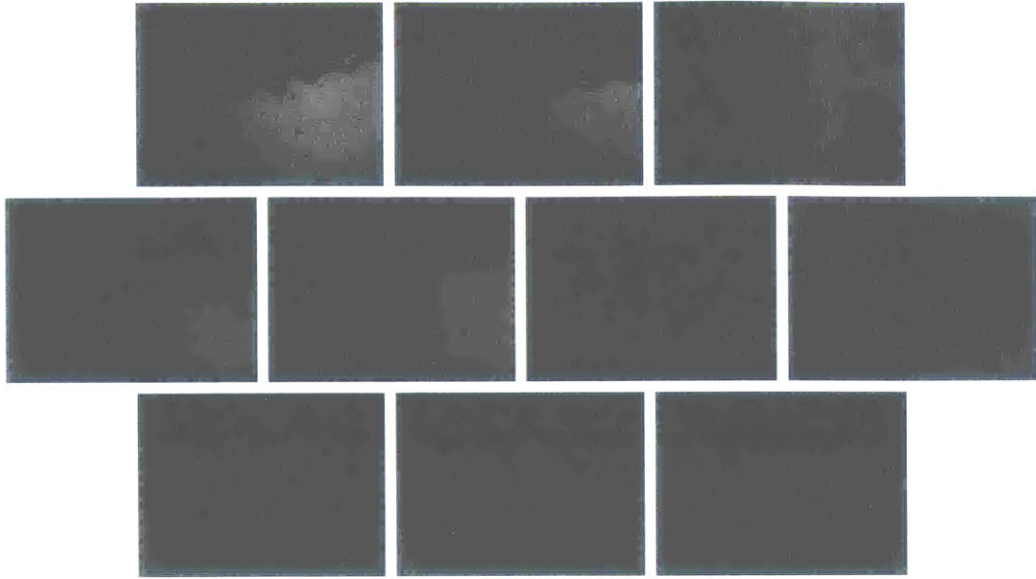


Figure A-19: Raw array images at position 10, with the cameras focused on the sheet's center and rotated 30.8° clockwise from the horizontal to be aligned with the sheet. The liquid flow rate was 269 gallons per minute.

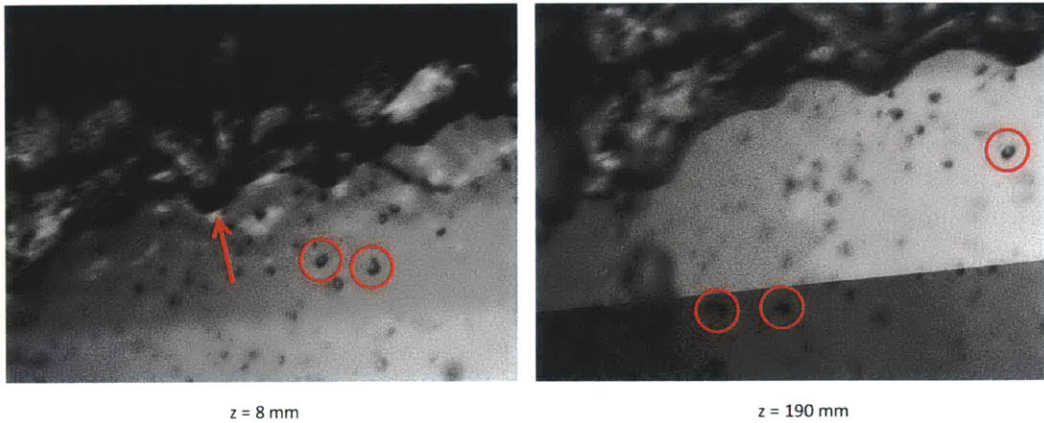


Figure A-20: Sample refocused planes with indicated in-focus features corresponding to the raw images in Figure A-19. Multiplicative refocusing was used with an exponent of 1/4.

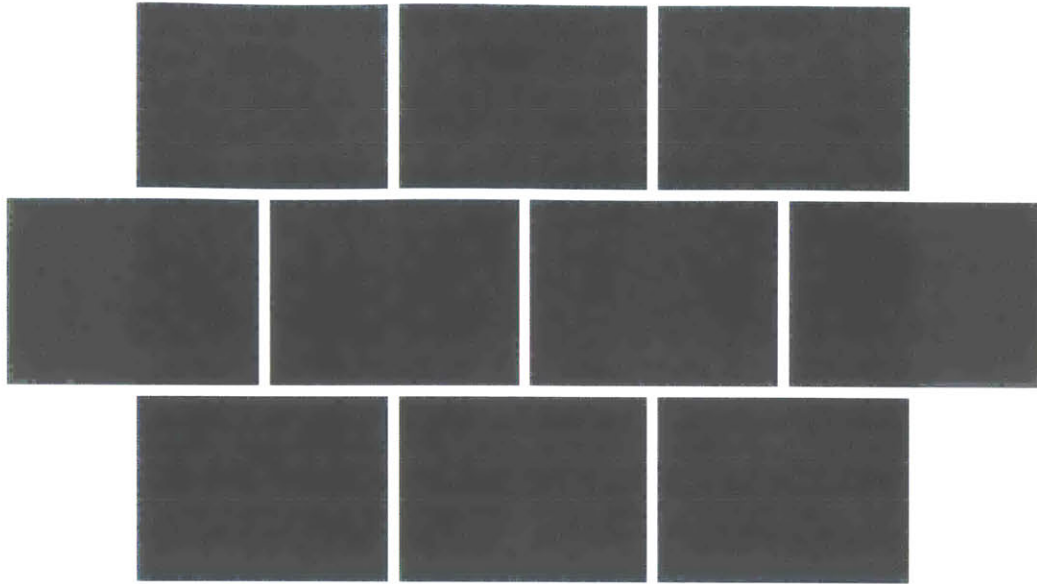


Figure A-21: Raw array images at position 11, with the cameras focused on the sheet's center and rotated  $30.8^\circ$  clockwise from the horizontal to be aligned with the sheet. The liquid flow rate was 268 gallons per minute.

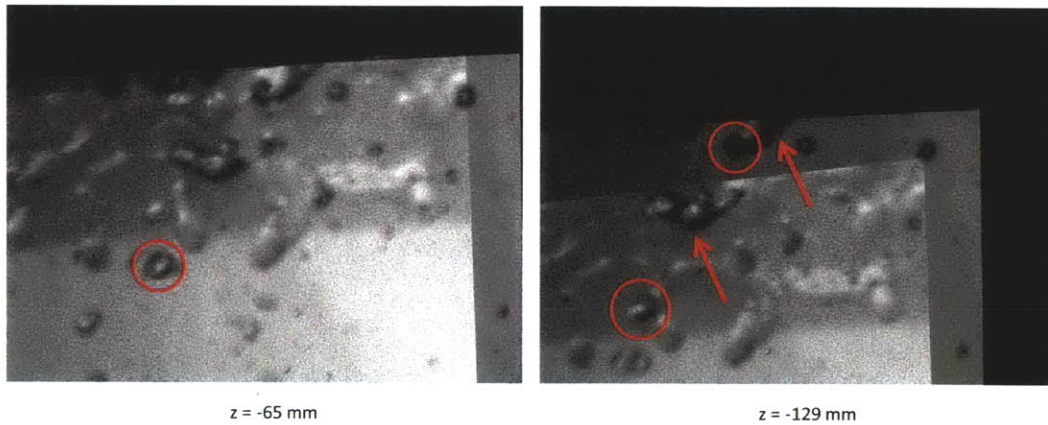


Figure A-22: Sample refocused planes with indicated in-focus features corresponding to the raw images in Figure A-21. Multiplicative refocusing was used with an exponent of  $1/4$ .

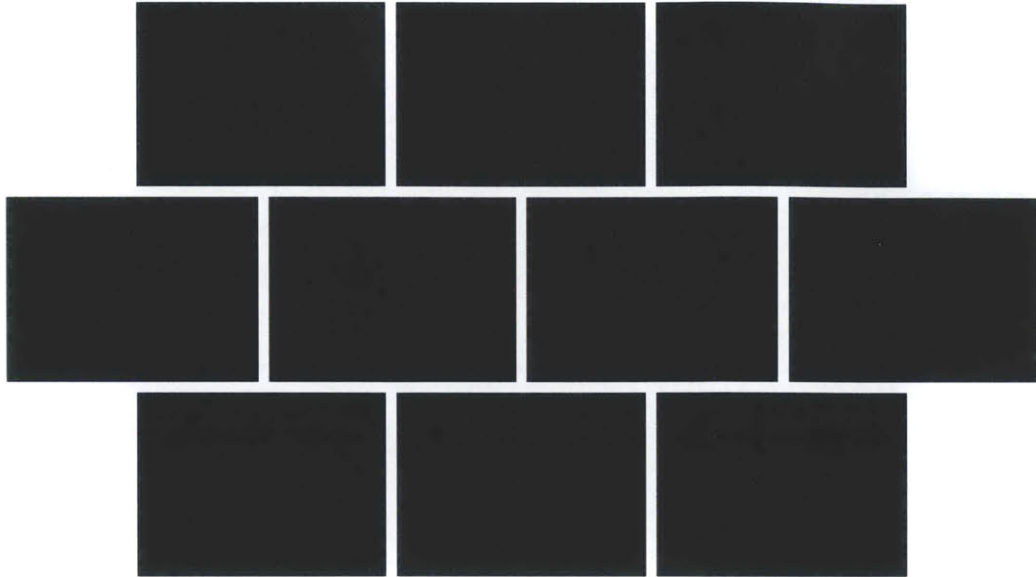


Figure A-23: Raw array images at position 12, with the cameras focused on the sheet's center and rotated 30.8° clockwise from the horizontal to be aligned with the sheet. The liquid flow rate was 268 gallons per minute.

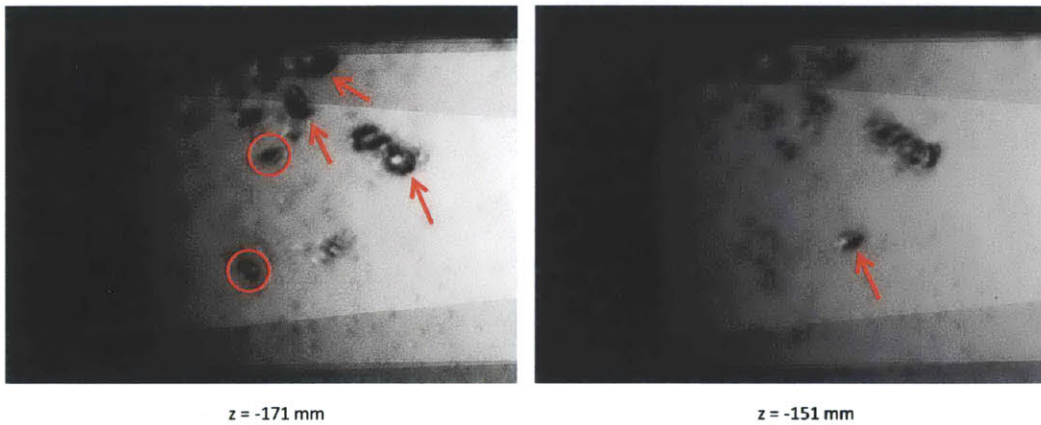


Figure A-24: Sample refocused planes with indicated in-focus features corresponding to the raw images in Figure A-23. Multiplicative refocusing was used with an exponent of 1/4.

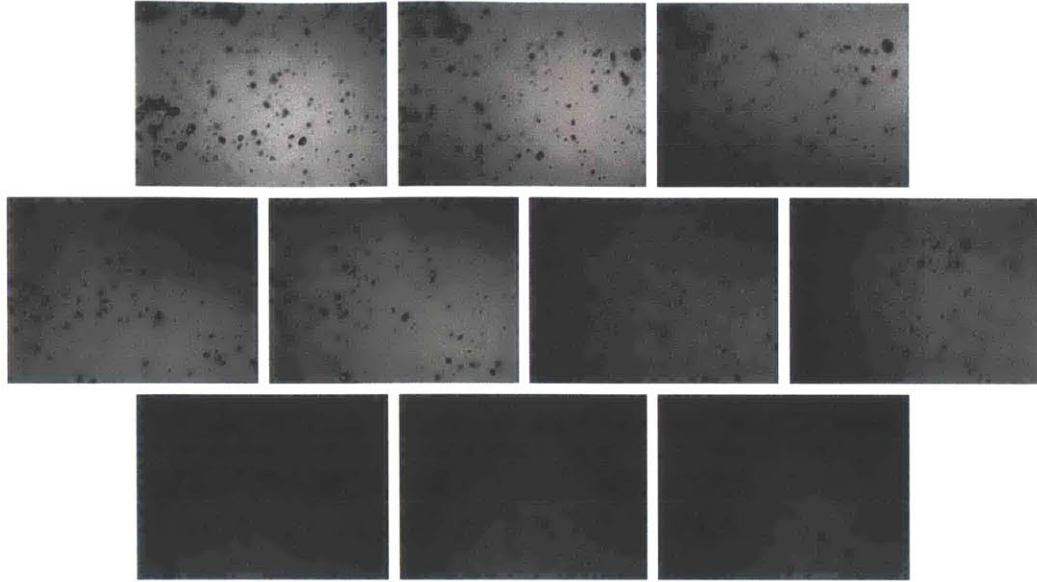


Figure A-25: Raw array images at position 13, with the cameras focused on the sheet's center and rotated  $30.8^\circ$  clockwise from the horizontal to be aligned with the sheet. The liquid flow rate was 269 gallons per minute.

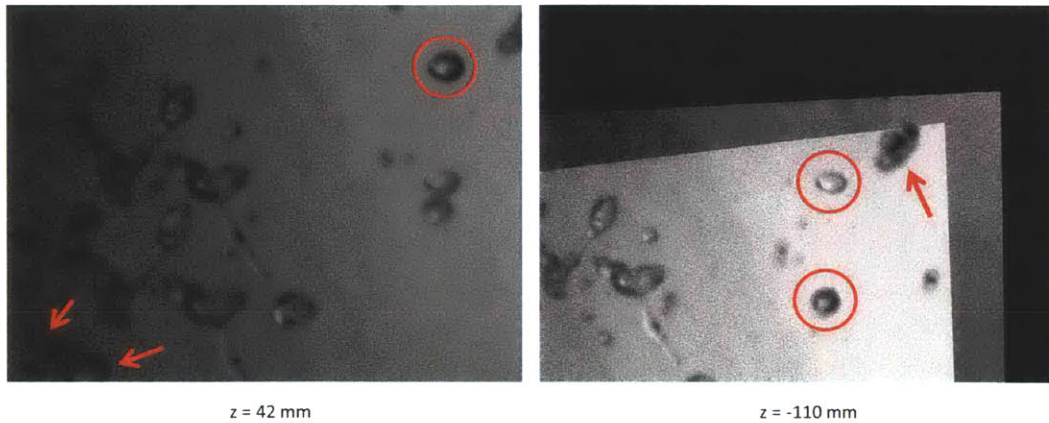


Figure A-26: Sample refocused planes with indicated in-focus features corresponding to the raw images in Figure A-25. Multiplicative refocusing was used with an exponent of  $1/4$ .



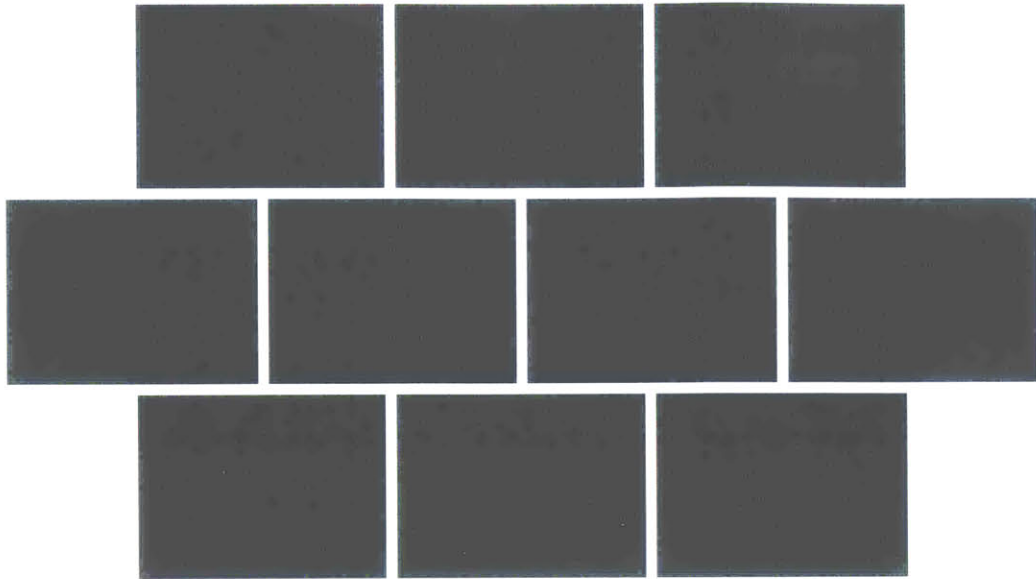


Figure A-27: Raw array images at position 14, with the cameras focused on the sheet's center and rotated  $30.8^\circ$  clockwise from the horizontal to be aligned with the sheet. The liquid flow rate was 269 gallons per minute.

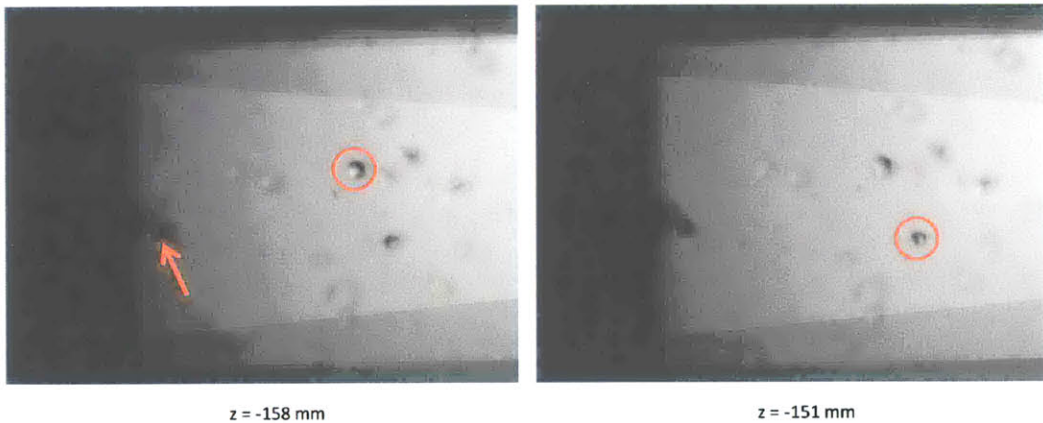


Figure A-28: Sample refocused planes with indicated in-focus features corresponding to the raw images in Figure A-27. Multiplicative refocusing was used with an exponent of  $1/4$ .

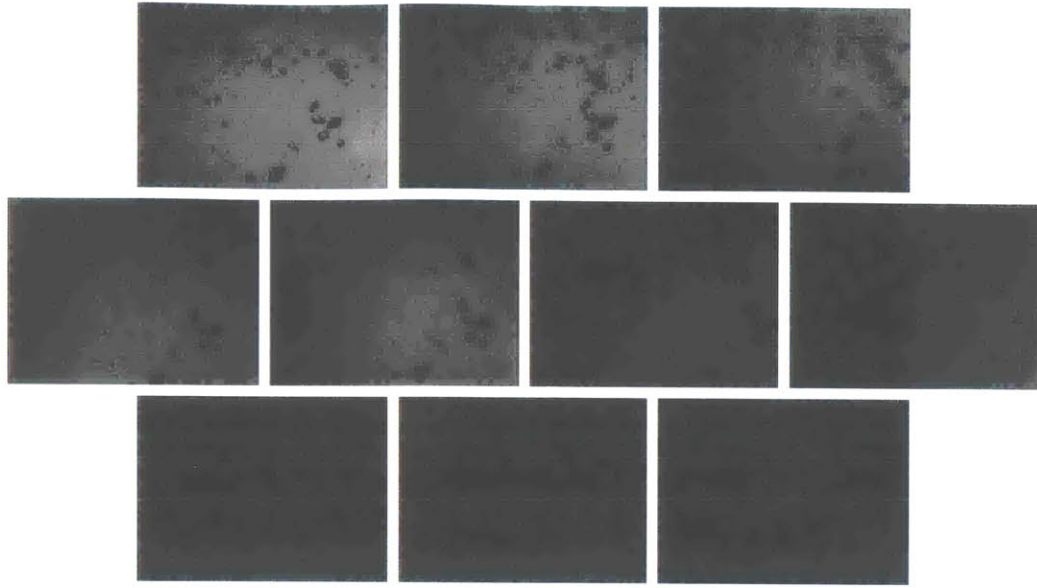


Figure A-29: Raw array images at position 15, with the cameras focused on the sheet's center and rotated  $30.8^\circ$  clockwise from the horizontal to be aligned with the sheet. The liquid flow rate was 269 gallons per minute.

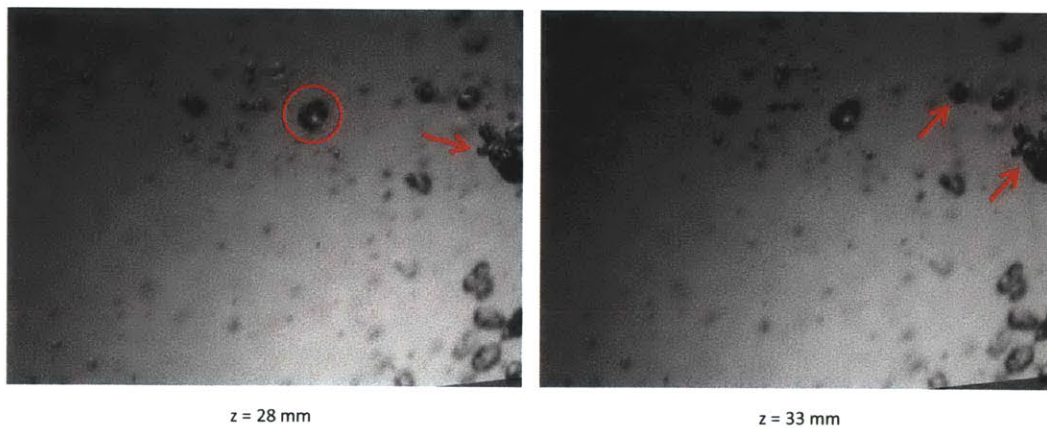


Figure A-30: Sample refocused planes with indicated in-focus features corresponding to the raw images in Figure A-29. Multiplicative refocusing was used with an exponent of  $1/4$ .

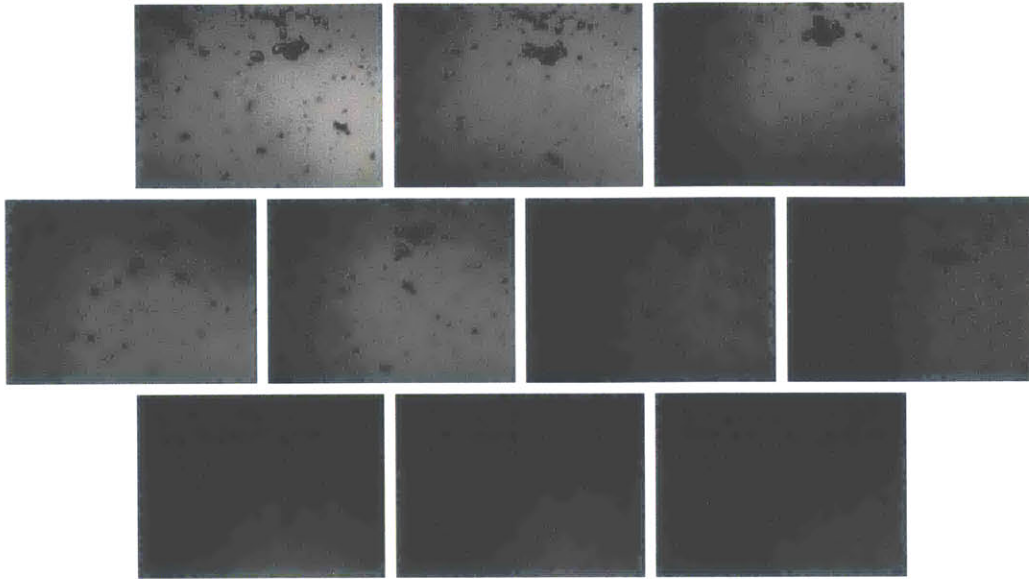


Figure A-31: Raw array images at position 16, with the cameras focused on the sheet's center and rotated 30.8° clockwise from the horizontal to be aligned with the sheet. The liquid flow rate was 267 gallons per minute.

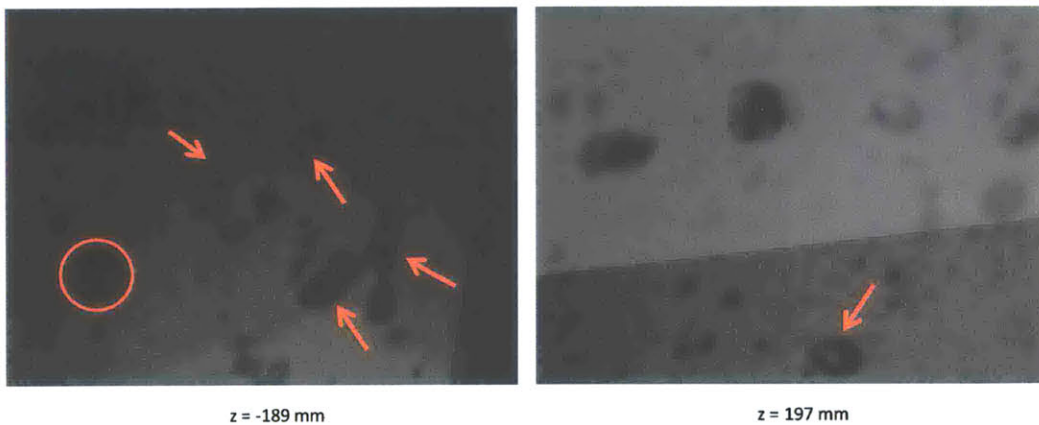


Figure A-32: Sample refocused planes with indicated in-focus features corresponding to the raw images in Figure A-31. Multiplicative refocusing was used with an exponent of 1/4.

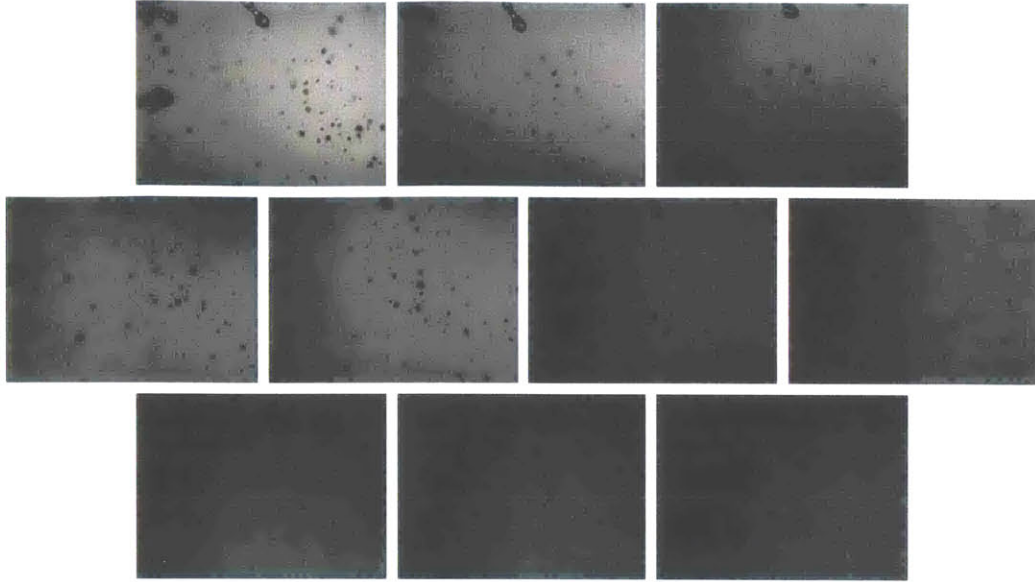


Figure A-33: Raw array images at position 17, with the cameras focused on the sheet's center and rotated 30.8° clockwise from the horizontal to be aligned with the sheet. The liquid flow rate was 266 gallons per minute.

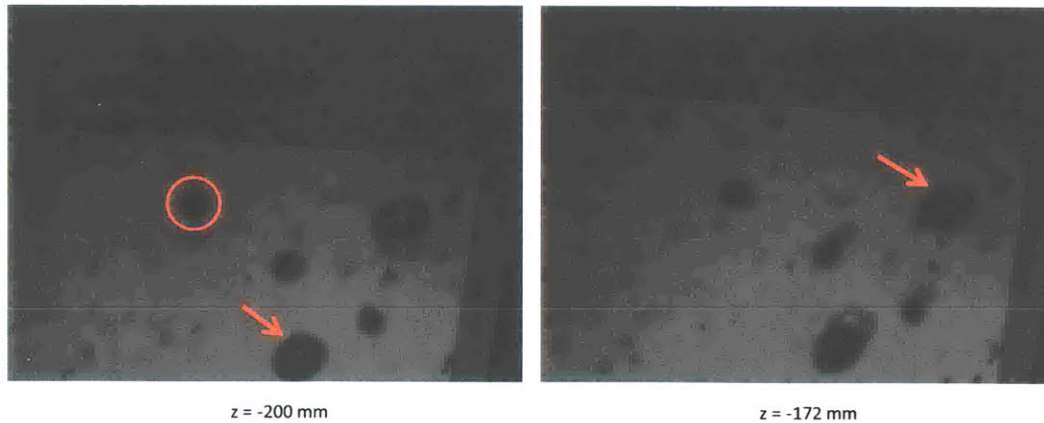


Figure A-34: Sample refocused planes with indicated in-focus features corresponding to the raw images in Figure A-33. Multiplicative refocusing was used with an exponent of 1/4.



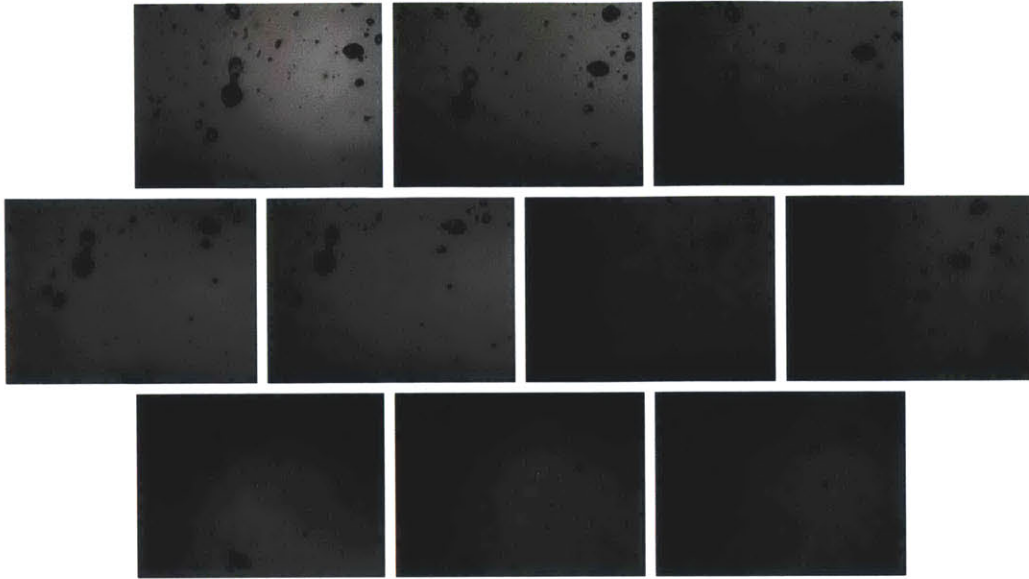


Figure A-35: Raw array images at position 18, with the cameras focused on the sheet's center and rotated 30.8° clockwise from the horizontal to be aligned with the sheet. The liquid flow rate was 266 gallons per minute.

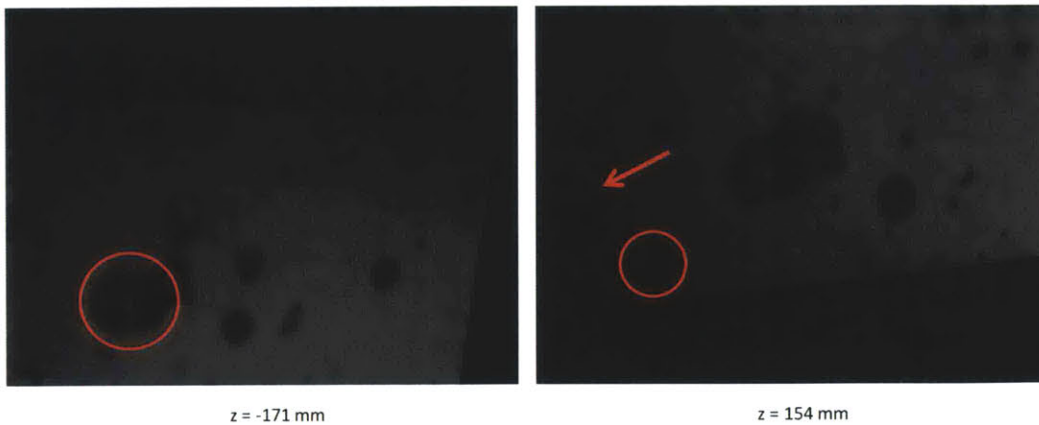


Figure A-36: Sample refocused planes with indicated in-focus features corresponding to the raw images in Figure A-35. Multiplicative refocusing was used with an exponent of 1/4.

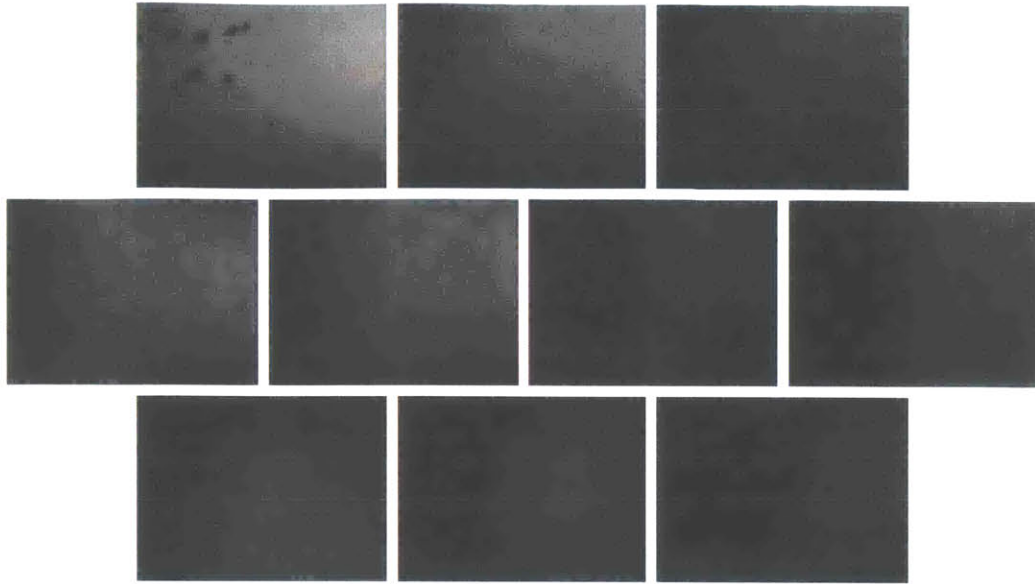


Figure A-37: Raw array images at position 19, with the cameras focused on the sheet's center and rotated 30.8° clockwise from the horizontal to be aligned with the sheet. The liquid flow rate was 268 gallons per minute.

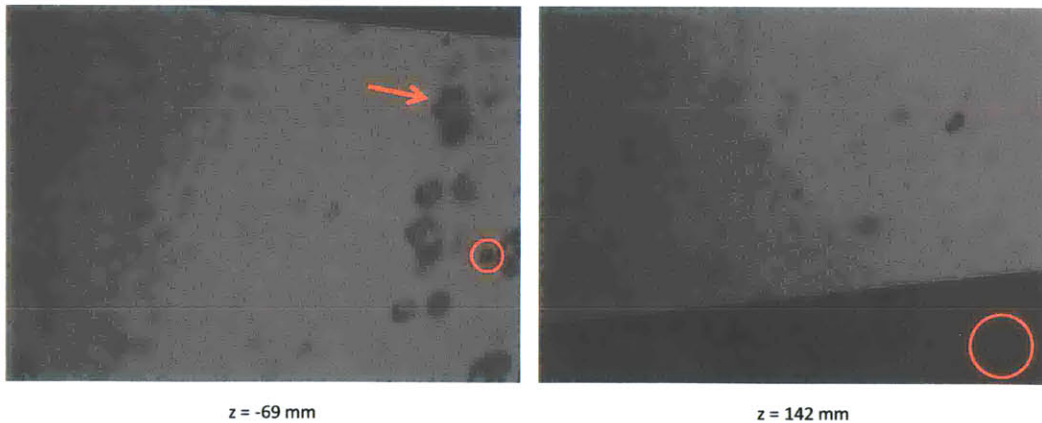


Figure A-38: Sample refocused planes with indicated in-focus features corresponding to the raw images in Figure A-37. Multiplicative refocusing was used with an exponent of  $1/4$ .

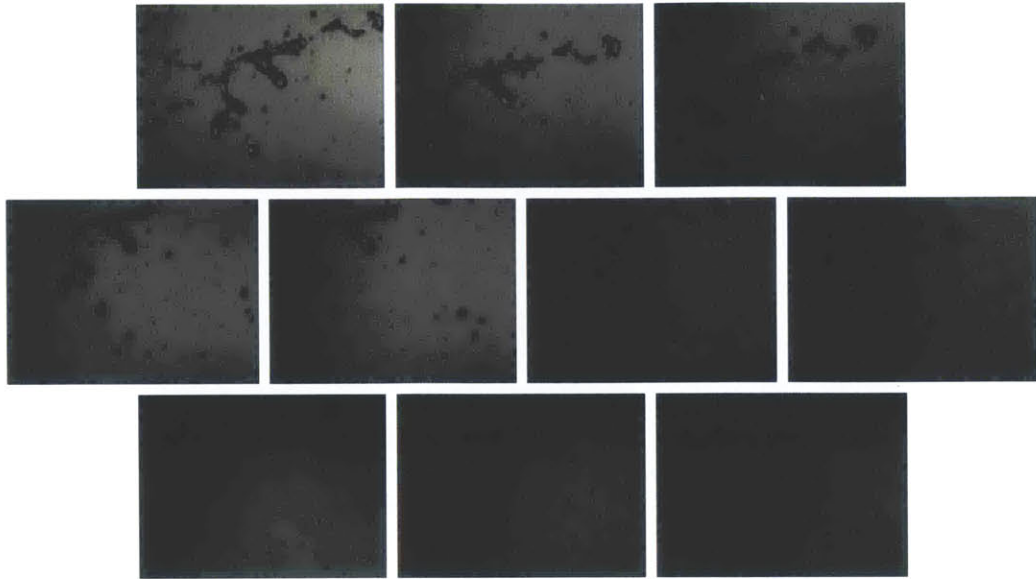


Figure A-39: Raw array images at position 20, with the cameras focused on the sheet's center and rotated 30.8° clockwise from the horizontal to be aligned with the sheet. The liquid flow rate was 268 gallons per minute.

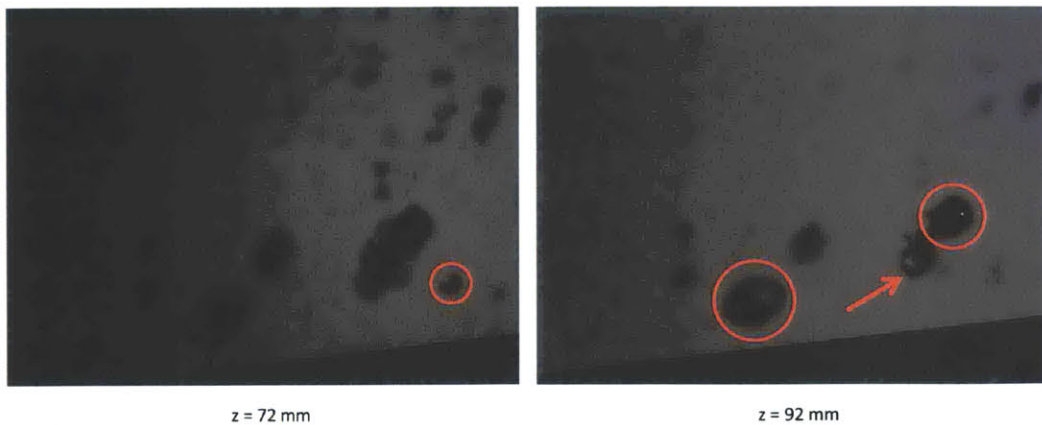


Figure A-40: Sample refocused planes with indicated in-focus features corresponding to the raw images in Figure A-39. Multiplicative refocusing was used with an exponent of 1/4.

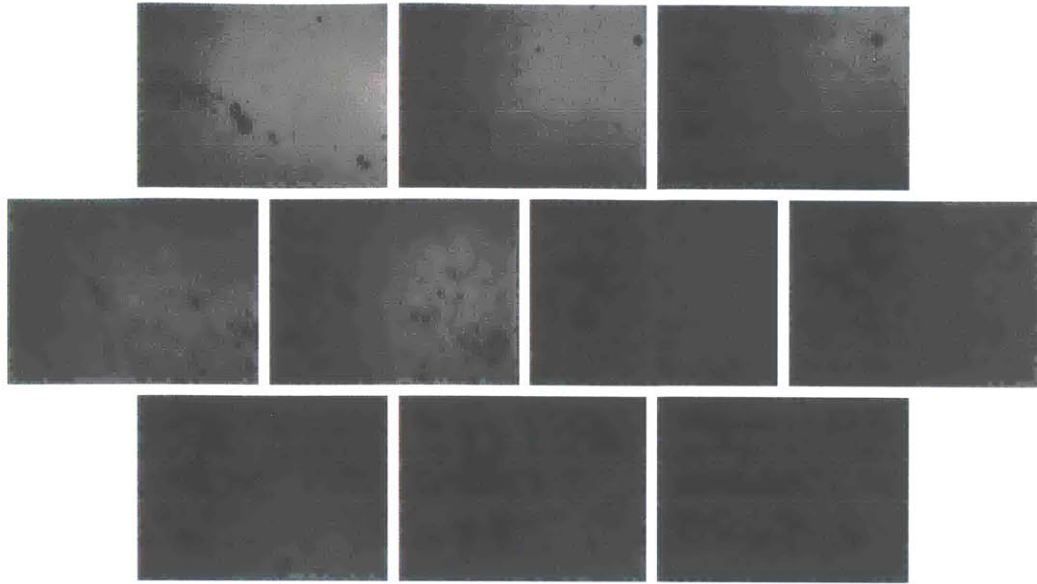


Figure A-41: Raw array images at position 21, with the cameras focused on the sheet's center and rotated  $30.8^\circ$  clockwise from the horizontal to be aligned with the sheet. The liquid flow rate was 268 gallons per minute.

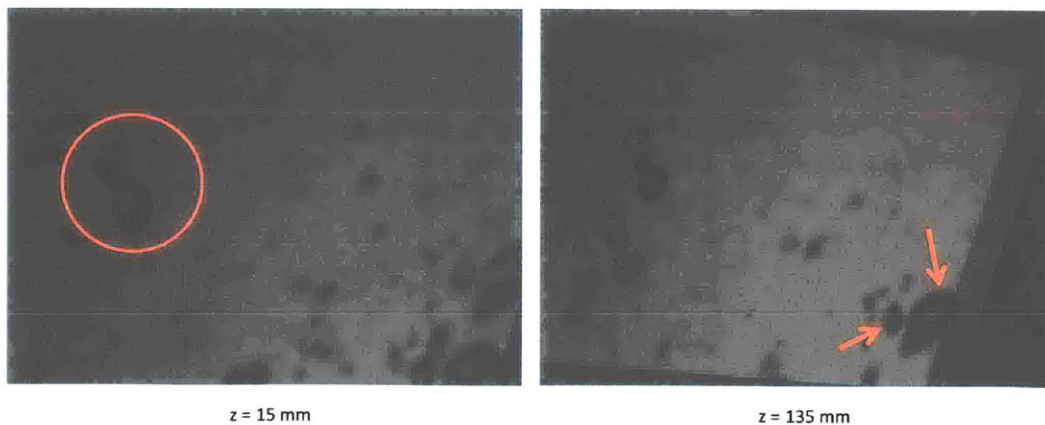


Figure A-42: Sample refocused planes with indicated in-focus features corresponding to the raw images in Figure A-41. Multiplicative refocusing was used with an exponent of  $1/4$ .

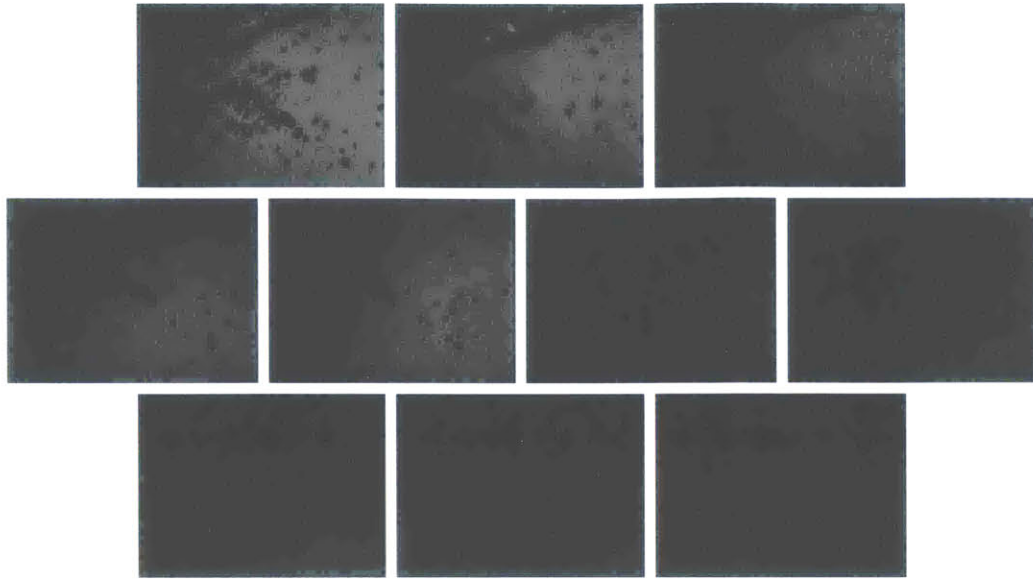


Figure A-43: Raw array images at position 22, with the cameras focused on the sheet's center and rotated 30.8° clockwise from the horizontal to be aligned with the sheet. The liquid flow rate was 268 gallons per minute.

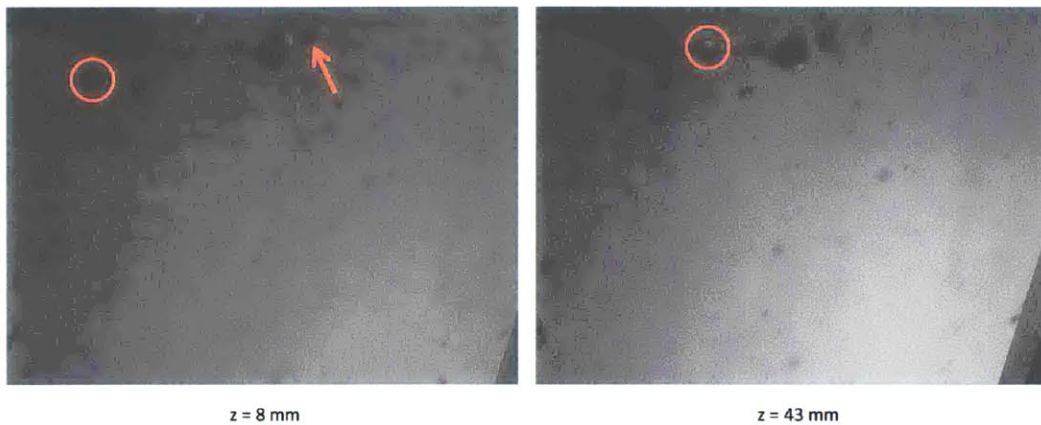


Figure A-44: Sample refocused planes with indicated in-focus features corresponding to the raw images in Figure A-43. Multiplicative refocusing was used with an exponent of 1/4.



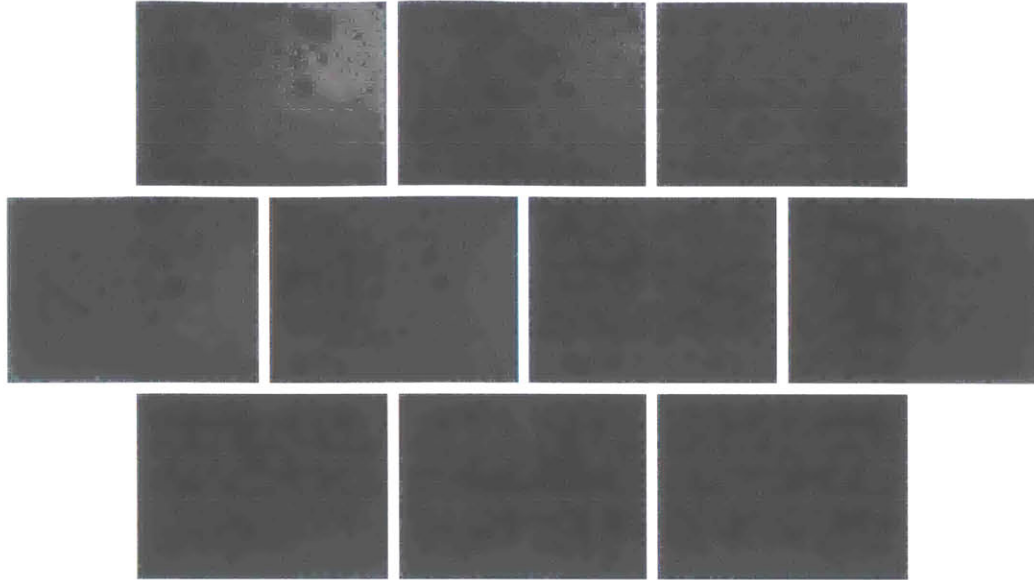


Figure A-45: Raw array images at position 23, with the cameras focused on the sheet's center and rotated  $30.8^\circ$  clockwise from the horizontal to be aligned with the sheet. The liquid flow rate was 269 gallons per minute.

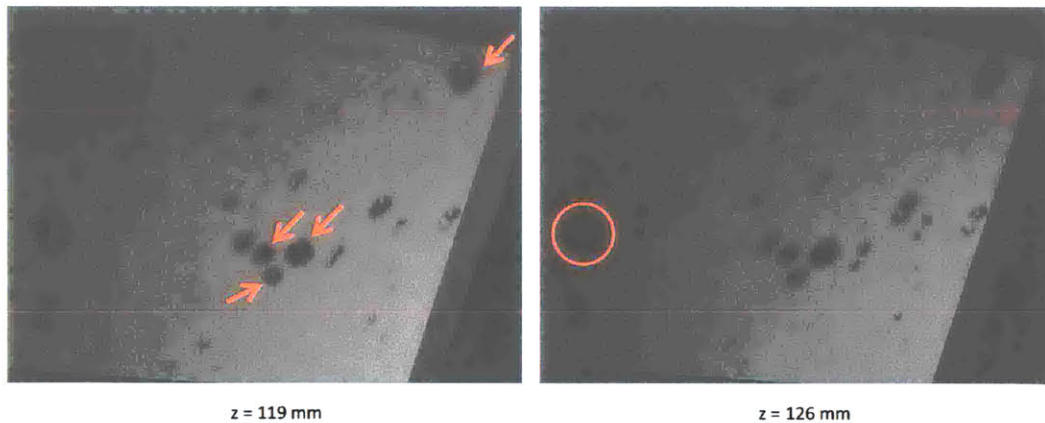


Figure A-46: Sample refocused planes with indicated in-focus features corresponding to the raw images in Figure A-45. Multiplicative refocusing was used with an exponent of  $1/4$ .

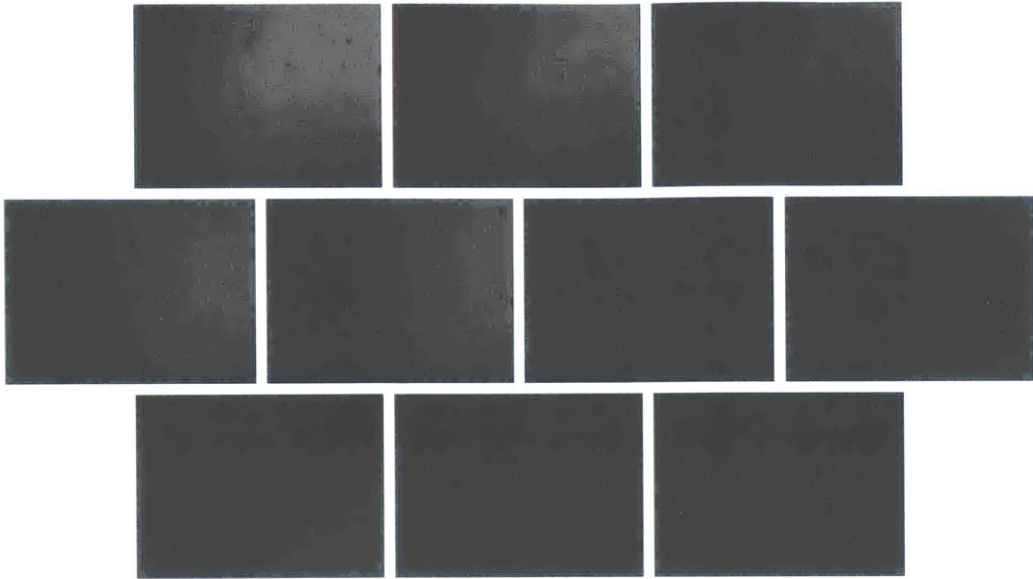


Figure A-47: Raw array images at position 24, with the cameras focused on the sheet's center and rotated  $30.8^\circ$  clockwise from the horizontal to be aligned with the sheet. The liquid flow rate was 268 gallons per minute.

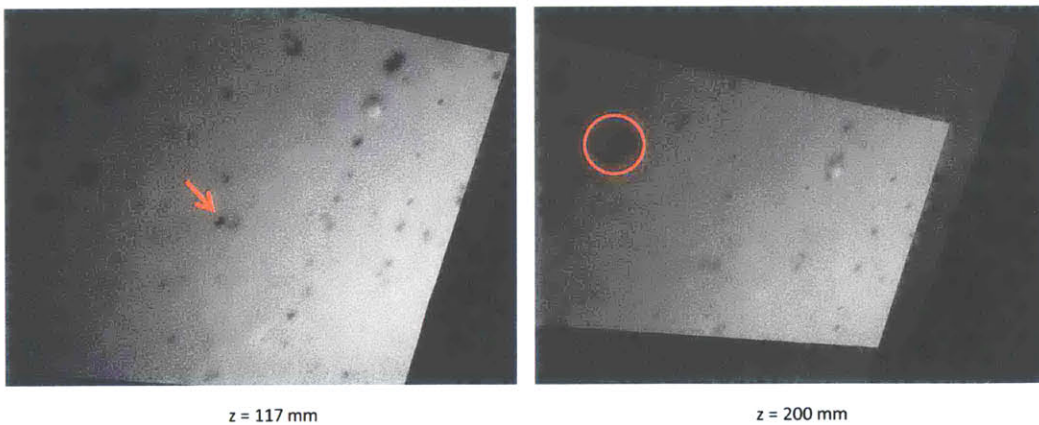


Figure A-48: Sample refocused planes with indicated in-focus features corresponding to the raw images in Figure A-47. Multiplicative refocusing was used with an exponent of  $1/4$ .

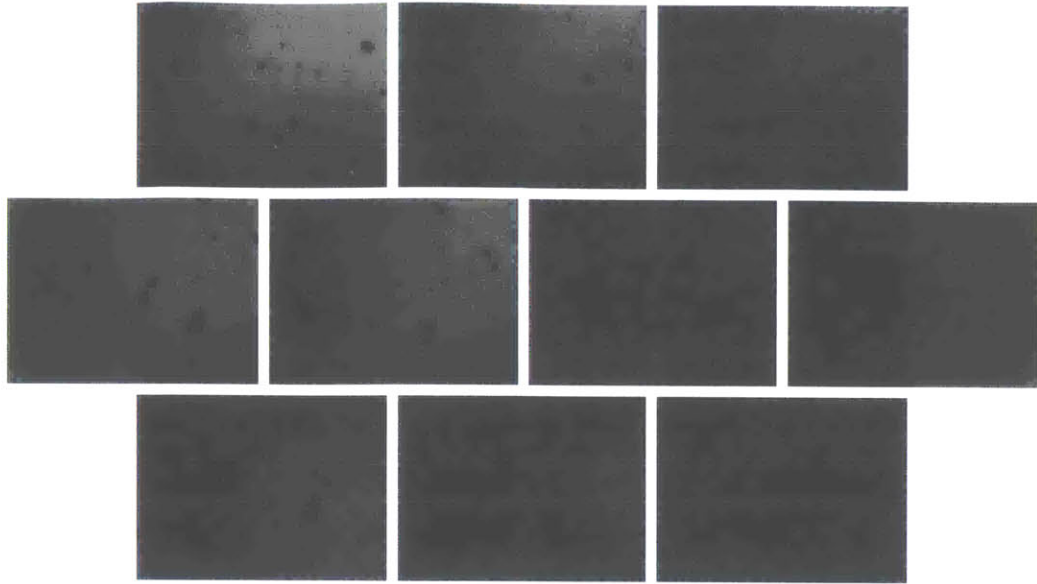


Figure A-49: Raw array images at position 25, with the cameras focused on the sheet's center and rotated  $30.8^\circ$  clockwise from the horizontal to be aligned with the sheet. The liquid flow rate was 268 gallons per minute.

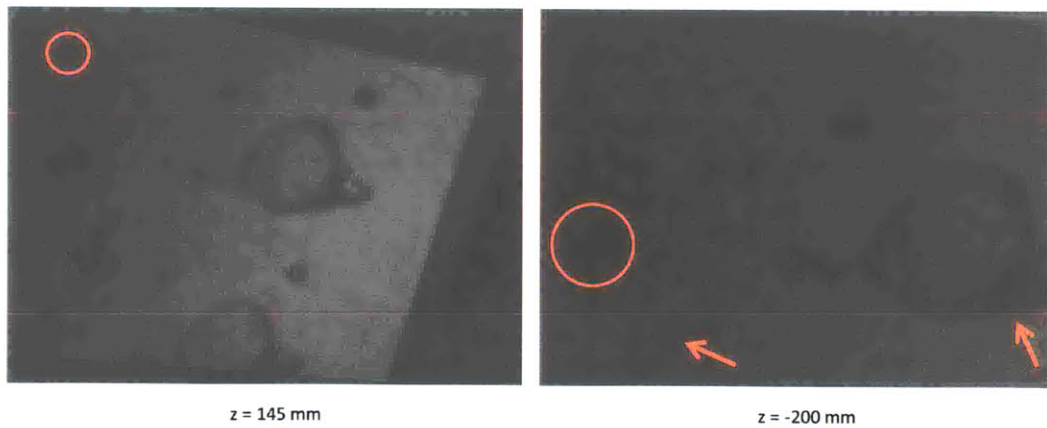


Figure A-50: Sample refocused planes with indicated in-focus features corresponding to the raw images in Figure A-49. Multiplicative refocusing was used with an exponent of  $1/4$ .



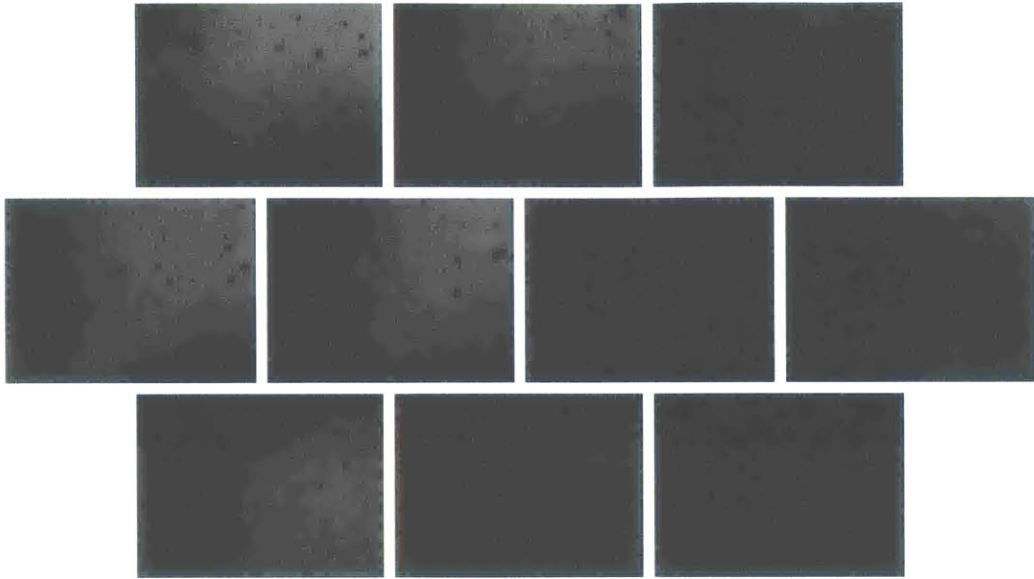


Figure A-51: Raw array images at position 26, with the cameras focused on the sheet's center and rotated 30.8° clockwise from the horizontal to be aligned with the sheet. The liquid flow rate was 268 gallons per minute.

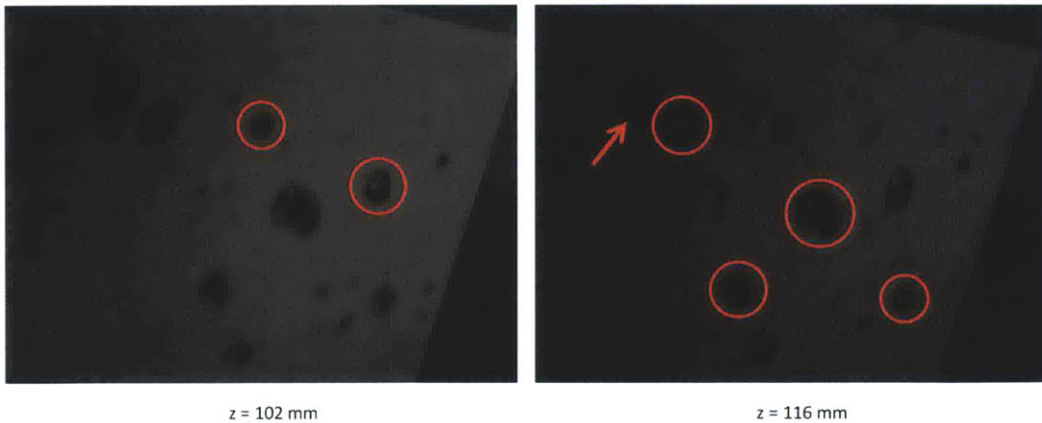


Figure A-52: Sample refocused planes with indicated in-focus features corresponding to the raw images in Figure A-51. Multiplicative refocusing was used with an exponent of  $1/4$ .

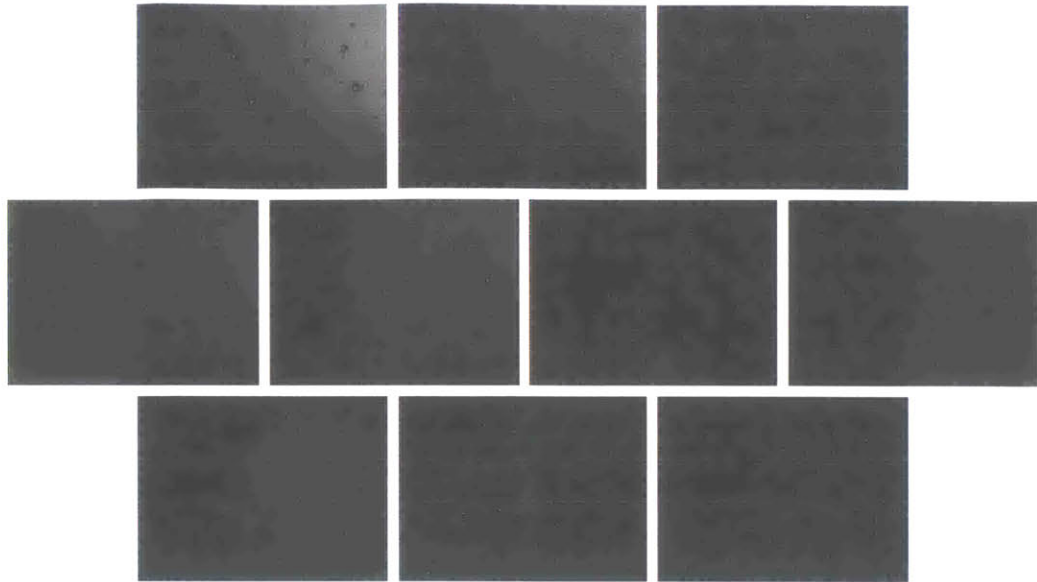


Figure A-53: Raw array images at position 27, with the cameras focused on the sheet's center and rotated 30.8° clockwise from the horizontal to be aligned with the sheet. The liquid flow rate was 269 gallons per minute.

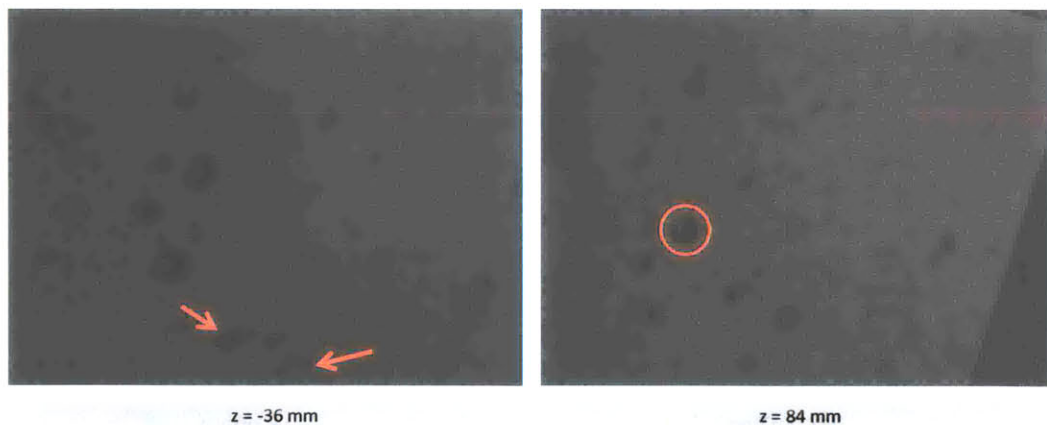


Figure A-54: Sample refocused planes with indicated in-focus features corresponding to the raw images in Figure A-53. Multiplicative refocusing was used with an exponent of 1/4.

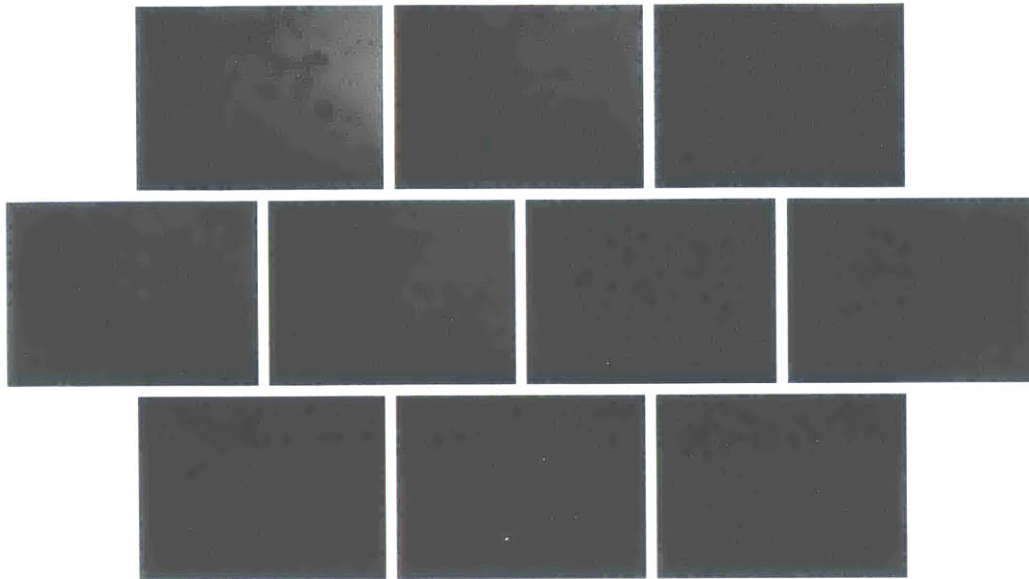


Figure A-55: Raw array images at position 28, with the cameras focused on the sheet's center and rotated 30.8° clockwise from the horizontal to be aligned with the sheet. The liquid flow rate was 269 gallons per minute.

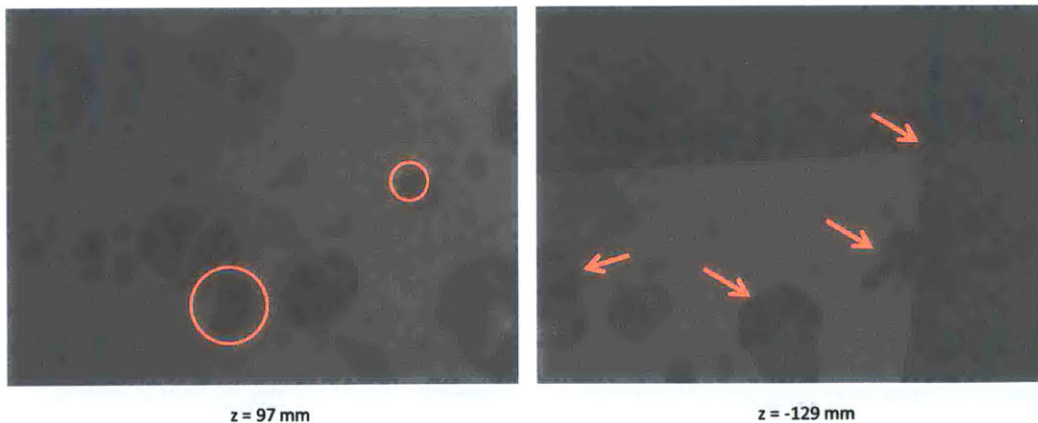


Figure A-56: Sample refocused planes with indicated in-focus features corresponding to the raw images in Figure A-55. Multiplicative refocusing was used with an exponent of  $1/4$ .

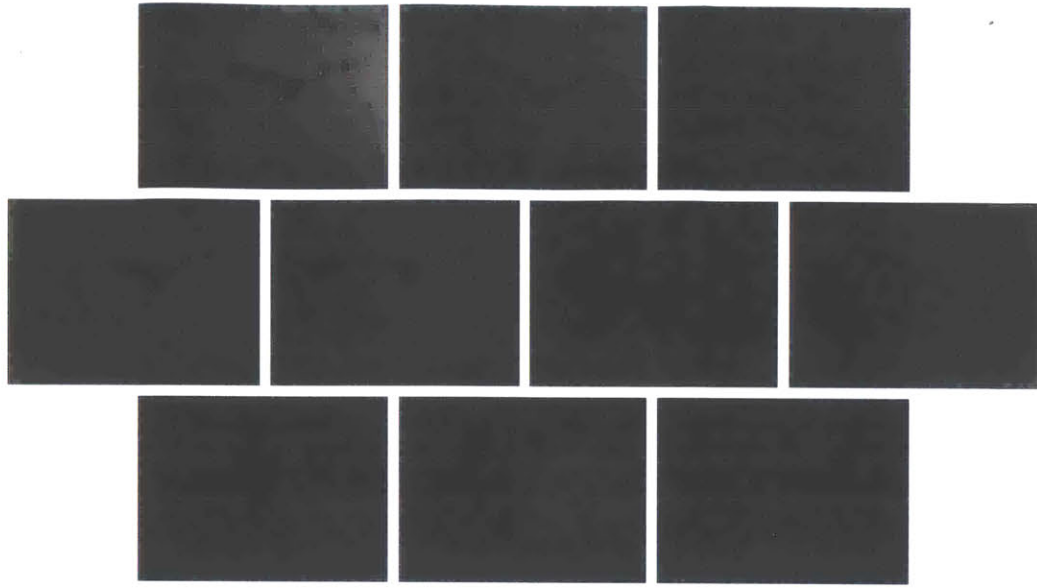


Figure A-57: Raw array images at position 29, with the cameras focused on the sheet's center and rotated 30.8° clockwise from the horizontal to be aligned with the sheet. The liquid flow rate was 266 gallons per minute.

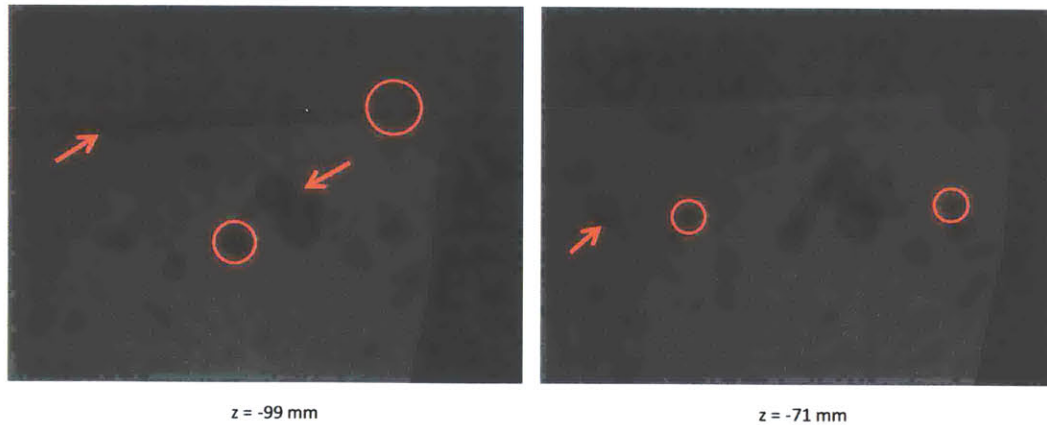


Figure A-58: Sample refocused planes with indicated in-focus features corresponding to the raw images in Figure A-57. Multiplicative refocusing was used with an exponent of 1/4.

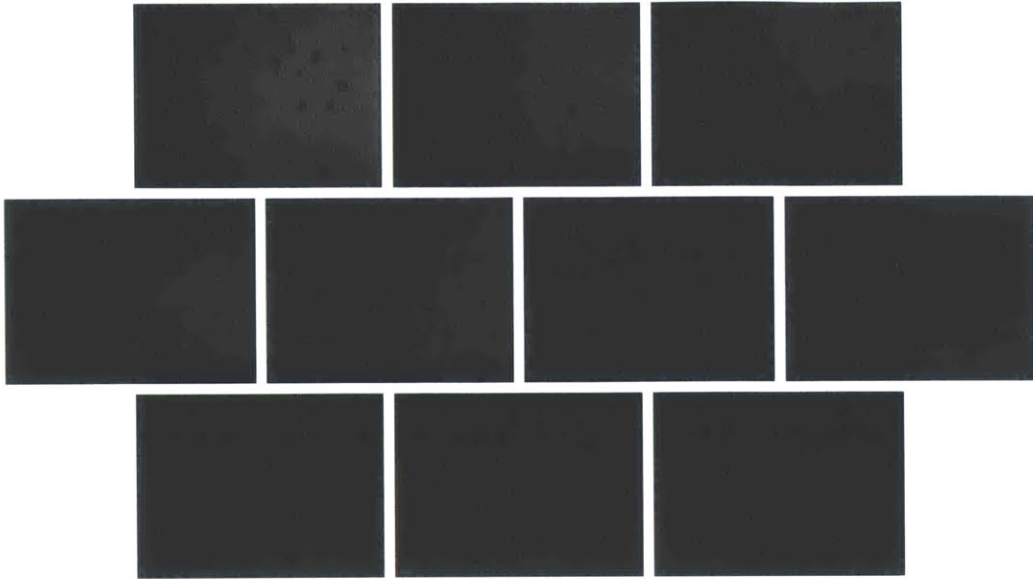


Figure A-59: Raw array images at position 30, with the cameras focused on the sheet's center and rotated 30.8° clockwise from the horizontal to be aligned with the sheet. The liquid flow rate was 266 gallons per minute.

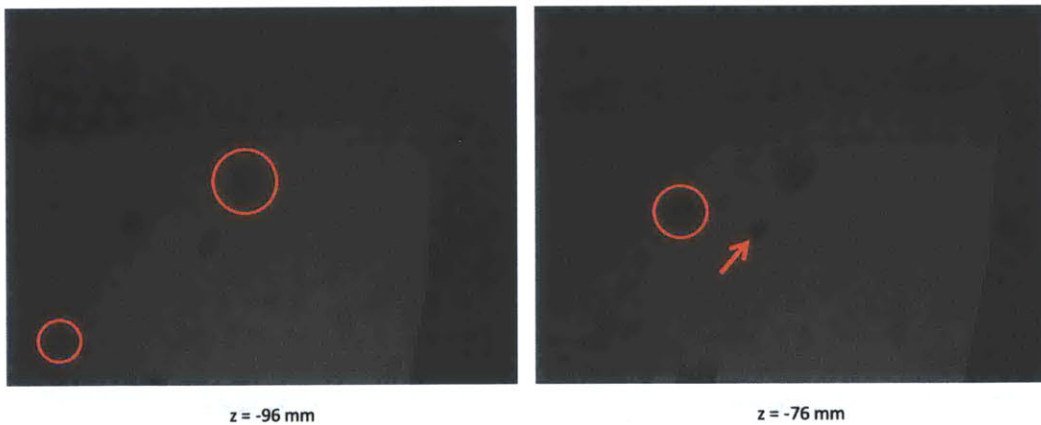


Figure A-60: Sample refocused planes with indicated in-focus features corresponding to the raw images in Figure A-59. Multiplicative refocusing was used with an exponent of 1/4.

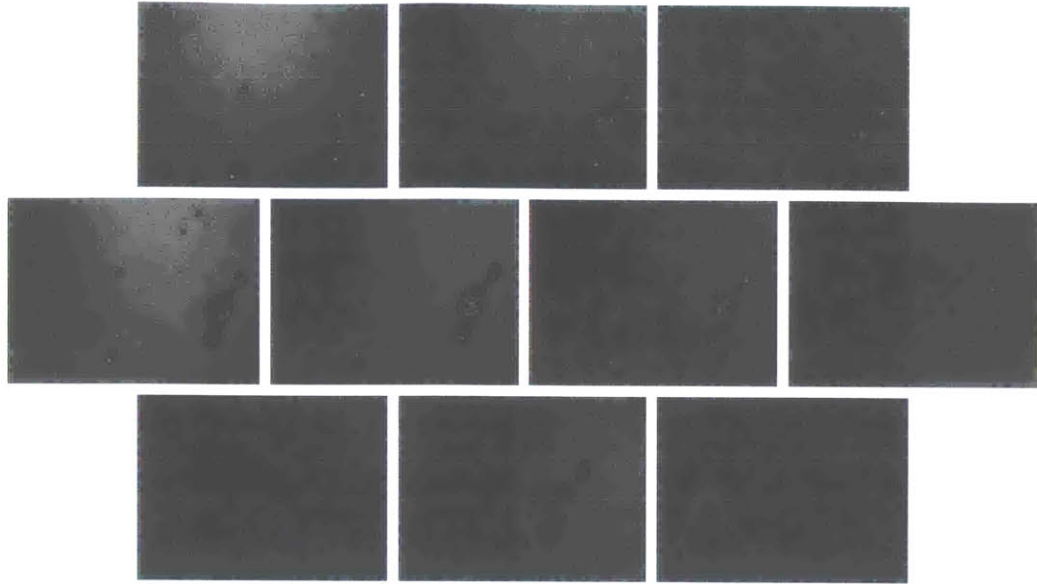


Figure A-61: Raw array images at position 31, with the cameras focused on the sheet's center and rotated  $30.8^\circ$  clockwise from the horizontal to be aligned with the sheet. The liquid flow rate was 269 gallons per minute.

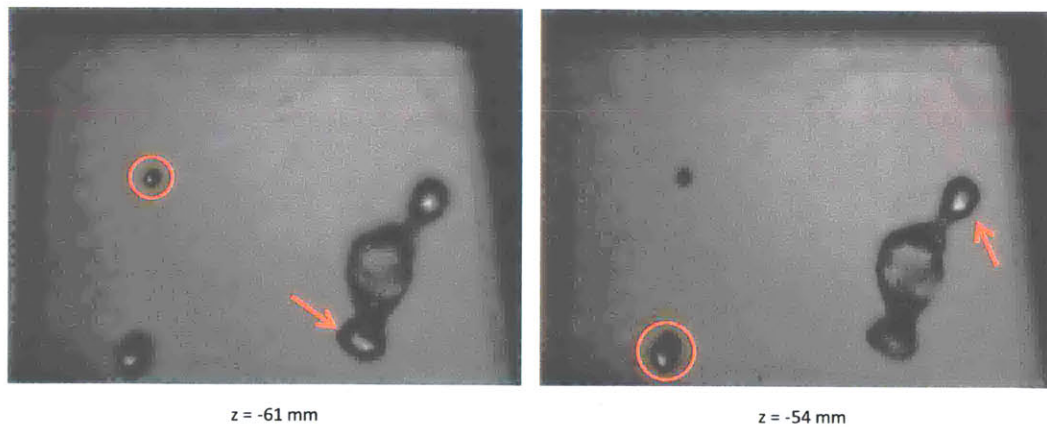


Figure A-62: Sample refocused planes with indicated in-focus features corresponding to the raw images in Figure A-61. Multiplicative refocusing was used with an exponent of  $1/4$ .



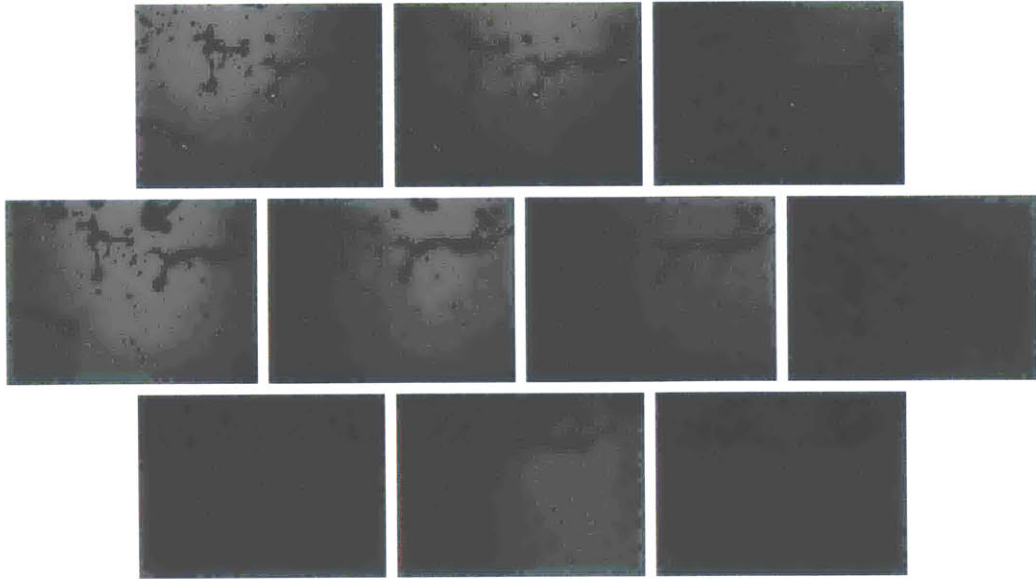


Figure A-63: Raw array images at position 32, with the cameras focused on the sheet's center and rotated 30.8° clockwise from the horizontal to be aligned with the sheet. The liquid flow rate was 270 gallons per minute.

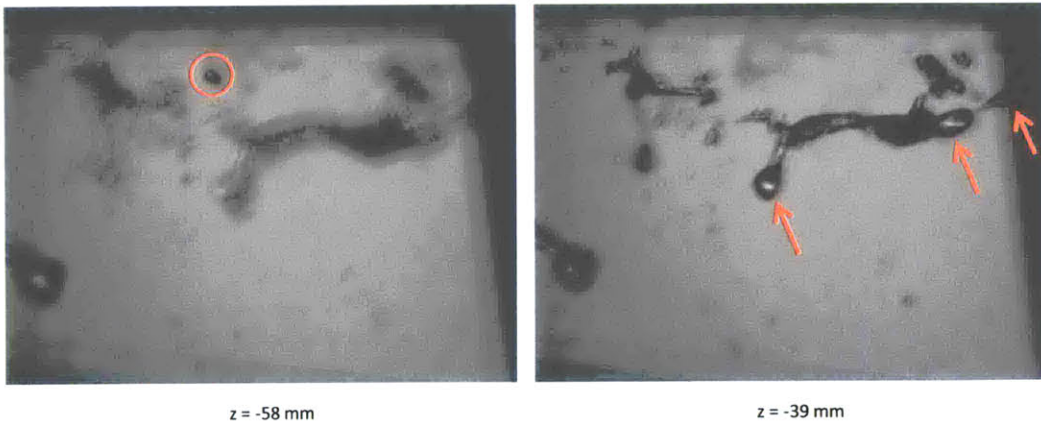


Figure A-64: Sample refocused planes with indicated in-focus features corresponding to the raw images in Figure A-63. Multiplicative refocusing was used with an exponent of 1/4.

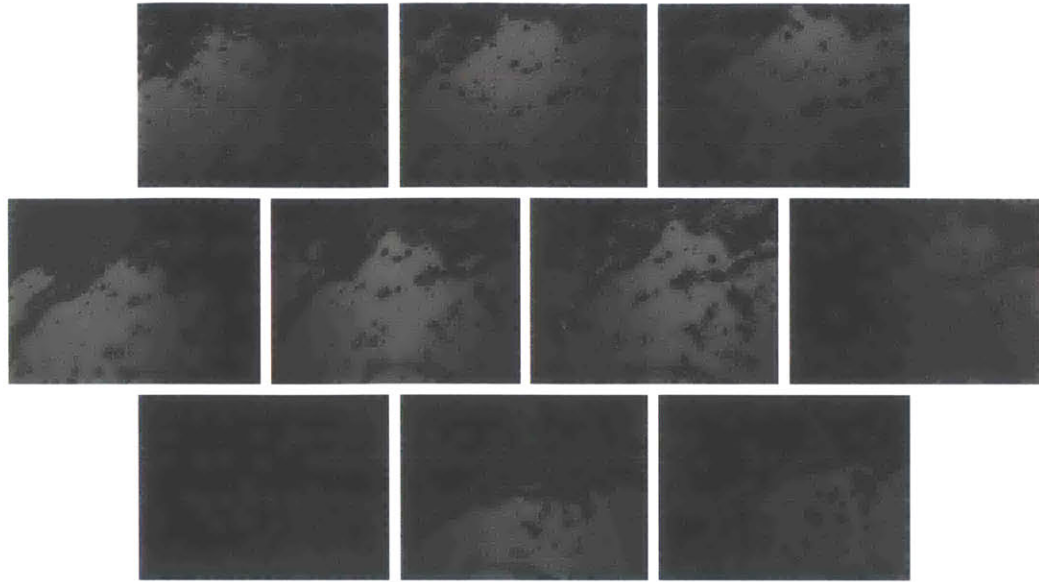


Figure A-65: Raw array images at position 33, with the cameras focused on the sheet's center and rotated 30.8° clockwise from the horizontal to be aligned with the sheet. The liquid flow rate was 269 gallons per minute.

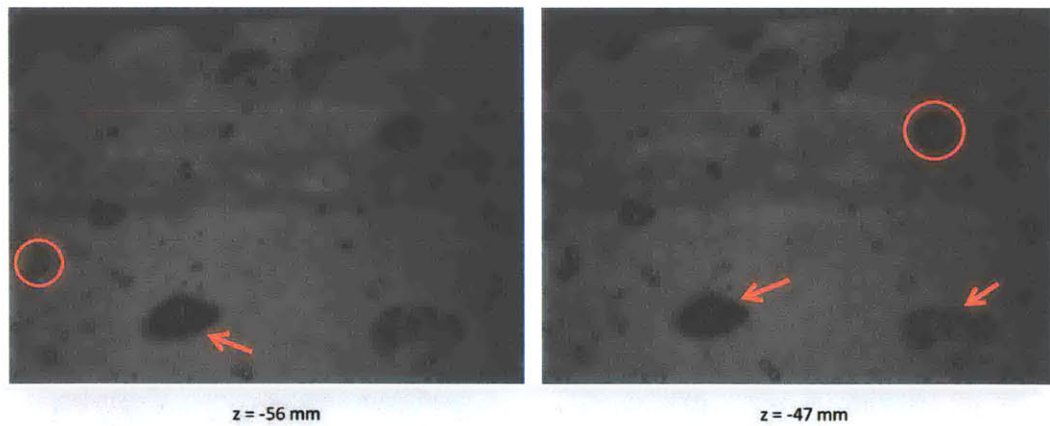


Figure A-66: Sample refocused planes with indicated in-focus features corresponding to the raw images in Figure A-65. Multiplicative refocusing was used with an exponent of 1/4.



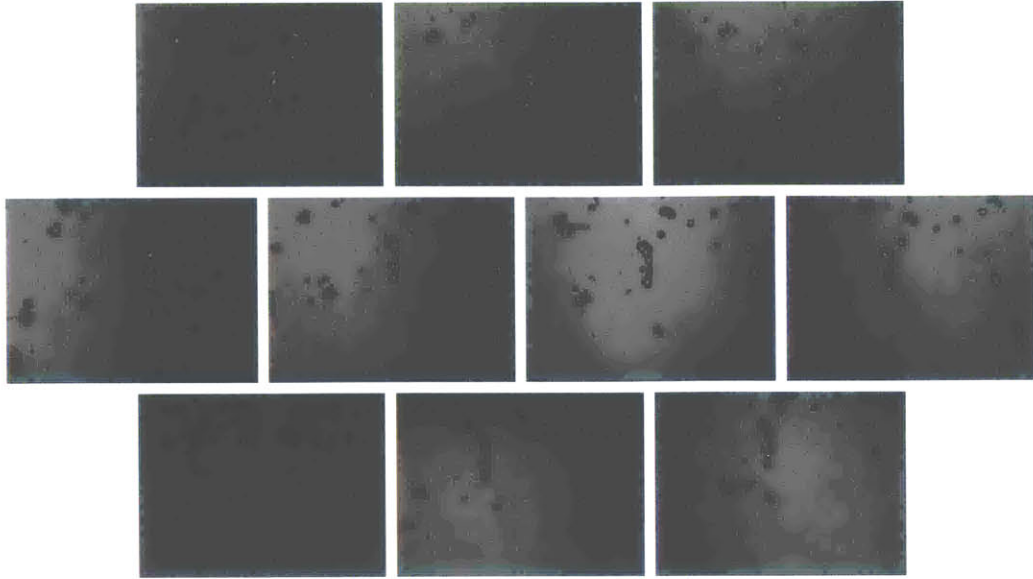


Figure A-67: Raw array images at position 34, with the cameras focused on the sheet's center and rotated 30.8° clockwise from the horizontal to be aligned with the sheet. The liquid flow rate was 270 gallons per minute.

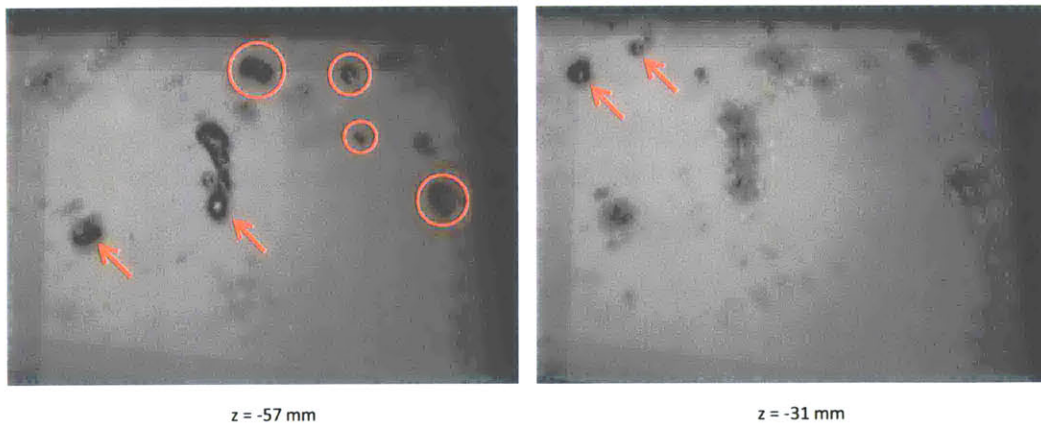


Figure A-68: Sample refocused planes with indicated in-focus features corresponding to the raw images in Figure A-67. Multiplicative refocusing was used with an exponent of 1/4.

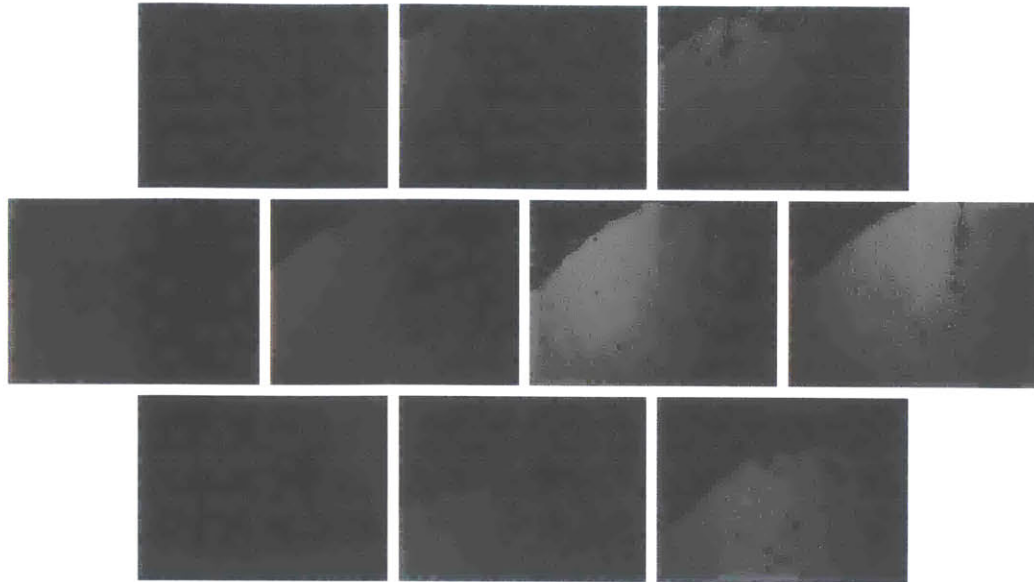


Figure A-69: Raw array images at position 35, with the cameras focused on the sheet's center and rotated 30.8° clockwise from the horizontal to be aligned with the sheet. The liquid flow rate was 270 gallons per minute.

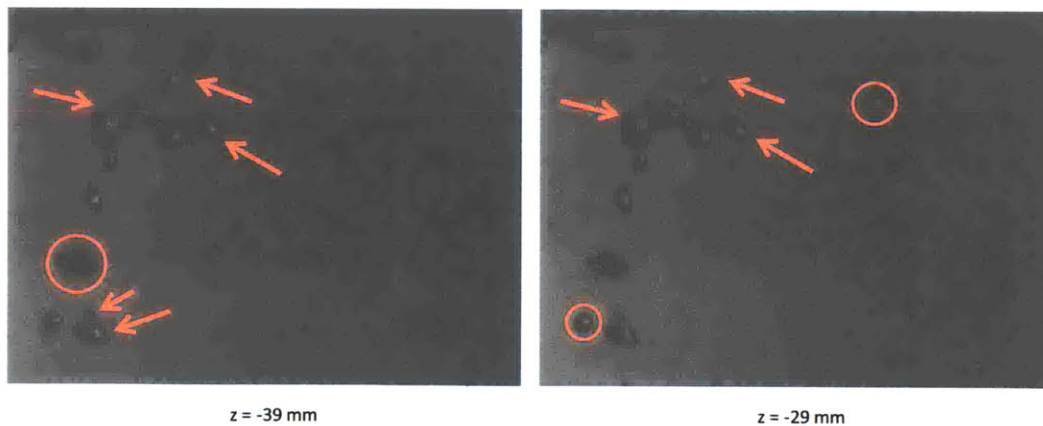


Figure A-70: Sample refocused planes with indicated in-focus features corresponding to the raw images in Figure A-69. Multiplicative refocusing was used with an exponent of 1/4.



Figure A-71: Raw array images at position 36, with the cameras focused on the sheet's center and rotated 30.8° clockwise from the horizontal to be aligned with the sheet. The liquid flow rate was 266 gallons per minute.

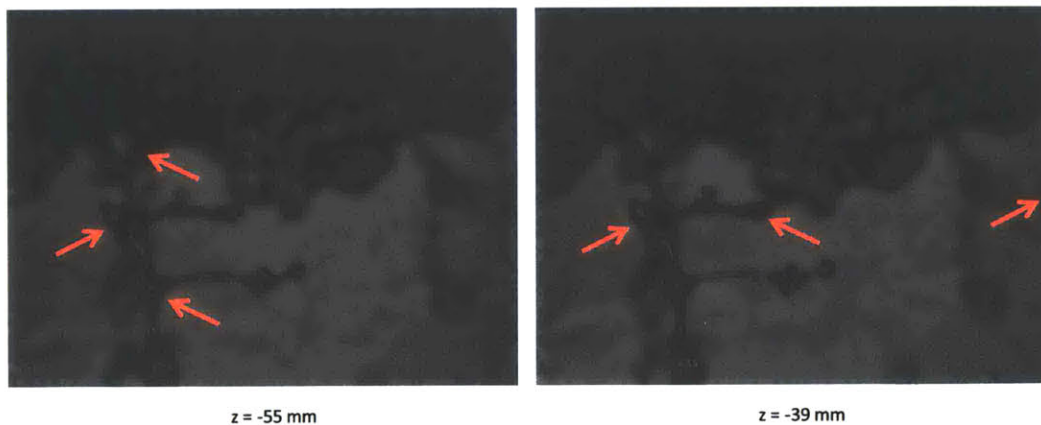


Figure A-72: Sample refocused planes with indicated in-focus features corresponding to the raw images in Figure A-71. Multiplicative refocusing was used with an exponent of 1/4.

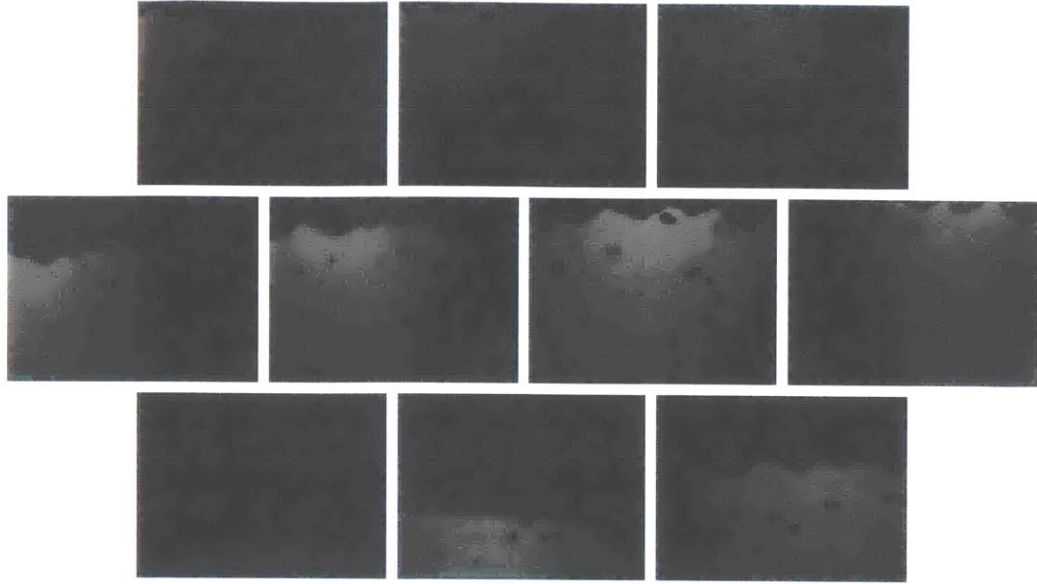


Figure A-73: Raw array images at position 37, with the cameras focused on the sheet's center and rotated 30.8° clockwise from the horizontal to be aligned with the sheet. The liquid flow rate was 267 gallons per minute.

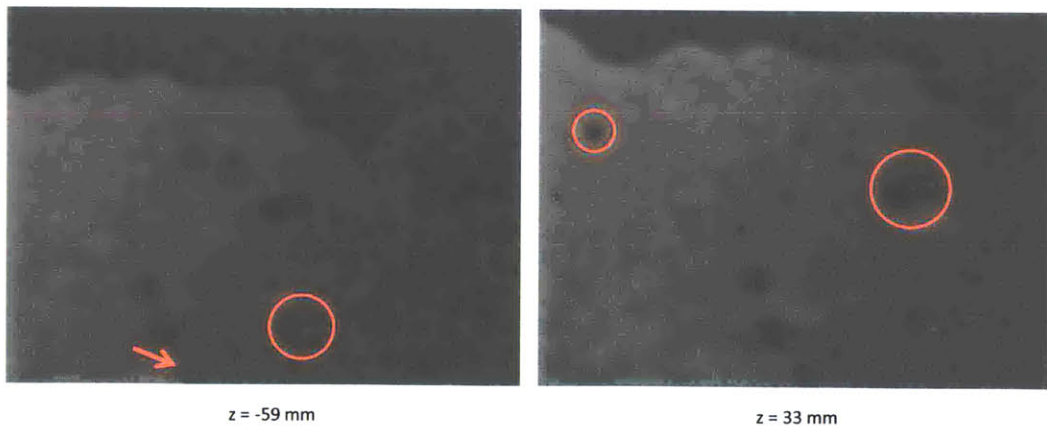


Figure A-74: Sample refocused planes with indicated in-focus features corresponding to the raw images in Figure A-73. Multiplicative refocusing was used with an exponent of 1/4.

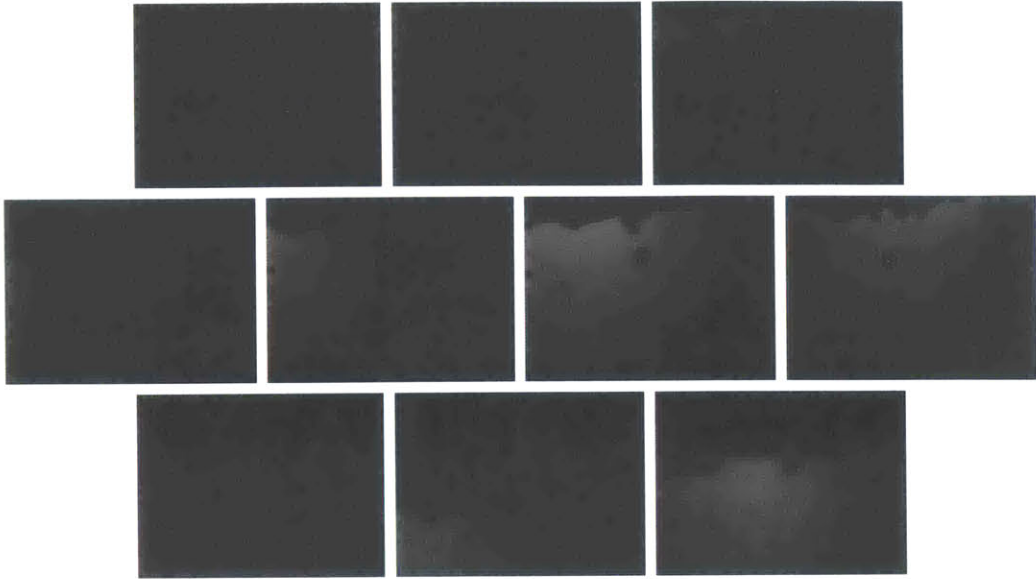


Figure A-75: Raw array images at position 38, with the cameras focused on the sheet's center and rotated 30.8° clockwise from the horizontal to be aligned with the sheet. The liquid flow rate was 266 gallons per minute.

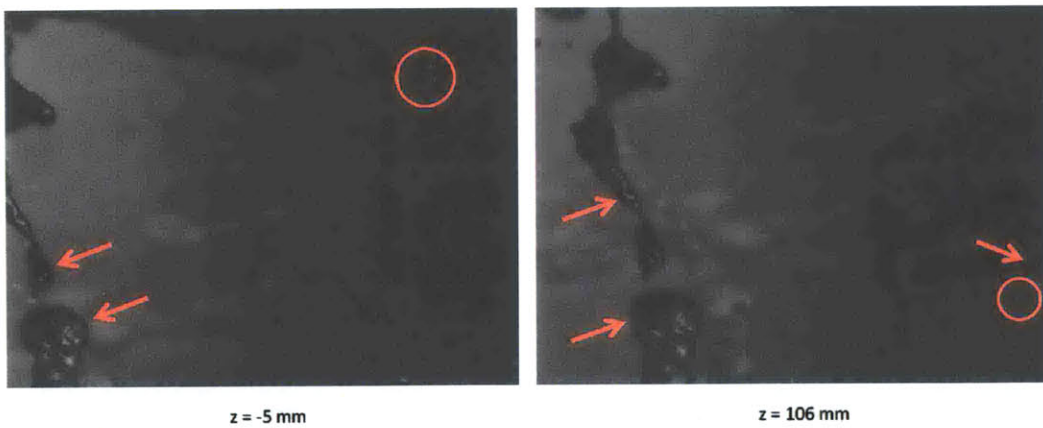


Figure A-76: Sample refocused planes with indicated in-focus features corresponding to the raw images in Figure A-75. Multiplicative refocusing was used with an exponent of 1/4.